The Dissertation Committee for Maryam Ali Certifies that this is the approved version of the following dissertation:

Dynamic Micro-3D-Printed Substrates for Characterizing Cellular Responses to Topography

Committee:

Jason B. Shear, Supervisor

Andrew K. Dunn

Daniel Johnston

Christine E. Schmidt

Wesley J. Thompson

Dynamic Micro-3D-Printed Substrates for Characterizing Cellular Responses to Topography

by

Maryam Ali, B.S.Ch.E.; M.S.

Dissertation

Presented to the Faculty of the Graduate School of
The University of Texas at Austin
in Partial Fulfillment
of the Requirements
for the Degree of

Doctor of Philosophy

The University of Texas at Austin
August 2014

Dedication

To the reader. I hope this dissertation helps you find what you are looking for.

Acknowledgements

I would like to thank my adviser, Jason Shear, for his support and guidance throughout my time in his lab. Without his encouragement of scientific creativity and his patience, I could not have taken on such an ambitious project. I would also like to thank the members of my committee for their consideration of my dissertation and for their stimulating questions during my dissertation defense. They made the experience much more enjoyable than I could have anticipated.

Many readers provided me critical feedback on early drafts of my dissertation. I'm especially grateful to Dr. Muhammad Zaman, Associate Professor in Biomedical Engineering at Boston University for his expert feedback on Chapter 1. I'd like to thank Drs. Samira Moorjani, Eric Spivey, and Jodi Connell for their technical reviews of Chapters 2, 3, and 4 respectively. Thanks also to Dr. Candace Seu, Janine Elliot, and Allison Myers for proofreading the text and offering general feedback.

My time in the Shear lab has been one of immense intellectual and personal growth, thanks to my colleagues. Many of them are now alumni of the group. Drs. Bryan Kaehr and Rex Nielson were graduating around the time I joined, but I benefited from their work and personal advice long after they left the lab. Dr. Samira Moorjani brought me up to speed in my early days in the lab and continues to be a resource I can call upon. Dr. Eric Spivey offered advice and encouragement in equal measure. Dr. Eric Ritschdorff provided crucial expertise in optomechanics and challenged my ideas rigorously. Drs. Stephanie Seidlits, Jodi Connell, and Todd Hoppe played a critical role in my intellectual growth, and I am thankful to them for their guidance and example. Derek Hernandez and Michael Robinson, who are also defending their dissertations this semester, have been a source of intellectual support over many years, and moral support over the months leading up to our defenses. Mignon Fitzgerald, Janine Elliot, and Allison Myers, who are current members of the Shear lab, have been a joy to work with. Their enthusiasm has kept me inspired through some of the most challenging days I faced. I look forward to hearing about their future accomplishments.

Two members of the University's research and technical staff have been immeasurable sources of help. Mr. Tim Hooper, the head of the Instrument Design & Repair facility for the Department of Chemistry, converted a humble office projector into a core component of the laser rig I use in my work. He also went above and beyond the scope of his duties by teaching me the basics of electrical wiring, advising me on components, and letting me borrow his tools when I tried my own hand at repairs and construction. Dr. Dwight Romanovicz, the Electron Microscopy Specialist at the Institute for Cellular and Molecular Biology, was always ready to brainstorm with me about ways to improve imaging of my samples on the SEM. His encyclopedic knowledge of sample preparation techniques is matched only by his enthusiasm in sharing interesting micrographs from his work. I have developed a deeper appreciation for electron microscopy by learning from him.

In the course of building my micro-3D printing rig, I gained a first-hand appreciation for the technical service representatives of instrument manufacturers, who are a font of knowledge and expertise. Steve Fullwood, Bioscience Specialist at Nikon

Instruments, was always available at a few days' notice to help me improve the functionality of my microscope. Joseph Sun de la Cruz, Applications Engineer at National Instruments, wrote a custom LabVIEW VI to help me add an image-skew feature to the digital mask display. The support specialists at Physik Instrumente and Molecular Devices were generously forthcoming with example programs and device drivers.

A few labs generously gifted biological samples. Dr. Stanislav Emilianov's lab provided my first sample of NIH-3T3 cells, and Dr. Paul Janmey at the University of Pennsylvania provided a gift of actin-GFP plasmids.

Many friends have crossed paths with my life during my graduate career and offered support when I needed it. Martha V., Erin B., Sandy O., Merc C., Candace S., and Jeff G. are among the many people who offered encouragement and raised my morale. The members of UT Sciences Toastmasters have provided both professional support and personal friendships. Without all of these people, this journey would have been much more difficult.

I am very grateful to my brother Mustafa, who has always been willing to listen to my jeremiads, offer his counsels, and provide technical advice on electrical and computer systems. He and my sister-in-law, Sana, have provided me space to take a breather from work when I needed one.

There are not enough words to express how much my parents' love, support and sacrifices have helped me accomplish what I have today. If I thank them every day of my life, it will still run short.

The research presented in this dissertation could not have been accomplished without the generous financial support of the Welch Foundation.

If I have neglected to mention anyone who played an important role in my graduate career, I apologize for the oversight. Please know that I would not be where I am without you.

Dynamic Micro-3D-Printed Substrates for Characterizing Cellular Responses to Topography

Maryam Ali, Ph.D.
The University of Texas at Austin, 2014

Supervisor: Jason B. Shear

Cell cultures provide researchers the opportunity to observe cell behavior in response to specific, well-defined environmental cues, leading to insights that enable better engineering design for tissue culture and other biomedical applications. Chemical and electrical stimuli have been successfully applied to cultured cells to approximate aspects of the dynamic conditions experienced *in vivo*. However, *in vitro* topographical cues have mostly been limited to static substrates that do not subject cells to the dynamic conditions they experience *in vivo* when tissue remodels during development and wound healing. Delivering dynamic topographical cues to cultured cells can answer long-standing questions about mechanisms of cell morphology changes. Such capabilities could also facilitate engineering of wound-healing matrices and nerve guidance conduits by promoting migration of cells and providing directional guidance to cellular processes.

This dissertation describes the development of approaches for introducing *in situ* topographical cues to cell cultures and inducing responses such as neurite guidance and cell alignment. Both strategies undertaken in this work make use of multiphoton-promoted photochemistry to print and manipulate three-dimensional microscopic protein hydrogel structures. In one approach, a technique referred to as *micro-3D printing,* topographical guidance cues are printed in the proximity of cultured cells to guide the growth of cellular processes. By translating a tightly-focused pulsed laser beam through a printing reagent solution flooding cultured cells, features are printed that provide physical guidance to extending neurites from NG108-15 cells, a neuronal model cell type. In another approach, an innovative technique known as *micro-3D imprinting* is developed for producing micrometer-scale depressions on the surfaces of photoresponsive protein hydrogels. The impact of various experimental parameters on topographical feature dimensions is characterized. Micro-3D imprinting is used to introduce dynamic topographical changes on a cell culture substrate, demonstrating that NIH-3T3 cells, a fibroblast cell model, alter their morphology and alignment in response to the introduction of a grooved surface topography. This set of approaches introduces new tools to the repertoire of cell biologists for exploring the behavior of cells growing in a spatio-temporally dynamic environment, opening possibilities for studies of cellular behavior in conditions that may better reflect environments cells experience *in vivo*.

Table of Contents

List of Tables

List of Figures

Chapter 1: Introduction and Literature Review

1.1 RECREATING THE CELLULAR ENVIRONMENT

In vitro cell and tissue culture arose in an attempt to understand the functions of biological cells in a systematic manner. Cells are capable of undertaking a variety of behaviors such as changing morphology, migration, differentiation, and apoptosis. Cells *in vivo* are difficult to observe because the opacity of tissues makes it challenging to observe deeper tissues without surgical intervention. In addition, environmental conditions in the body – such as temperature, chemical concentrations, and topography – are in constant flux and difficult to measure. Moreover, samples are heterogeneous, making it difficult to draw generalized conclusions about the behavior of any given cell type.

A common strategy in cell biology is to extract cells from the *in vivo* environment and keep them viable *in vitro* to enable experimental observations in a controlled environment. In the late 19th century, Leo Loeb first suggested the possibility of keeping cells alive outside the body [1]. An early successful strategy for growing cells *in vitro* was to plate an organ fragment as a tissue explant. Cells migrated onto the substrate from the tissue and could be observed individually rather than as part of a heterogeneous aggregate. In 1907, Harrison maintained a culture of explanted frog embryonic cells in a lymph clot for a few weeks [2]. By the mid-20th century, the development of physical and enzymatic disaggregation techniques allowed cells to be dispersed from a tissue sample and plated as individual cells [3,4]. This helped in the establishment of cell lines with a consistent genetic makeup. Important milestones were the L-strain mouse fibroblast line in 1948 [5] and the human HeLa cell line in 1952 [6]. These genetically homogeneous cells responded consistently to environmental conditions, allowing more conclusive experimental observations.

Other important developments involved the standardization of culturing media. The earliest tissue cultures were maintained in isotonic solutions, lymph clots, blood plasma, and mixtures thereof. Animal blood serum (plasma without clotting factors) provided cells a wide range of nutrients and chemical factors they need to thrive. However, these sera had batch-to-batch variations in their levels of biological components (e.g. hormones and growth factors), causing cells to grow at different rates. The sera could also contain infectious contaminants because of their animal origins. The need for consistency drove the development of chemically-defined media, such as Eagle's minimal essential medium, which are widely used today [7–9]. Such media often need to be supplemented with small amounts of sera to provide the full complement of nutrients and carrier proteins needed by particular cell lines, but improved characterization of sera components is allowing the development of entirely synthetic complete media for many cell types [10].

Adherent cells, which comprise the majority of cell types, require a suitable substrate for healthy growth. The earliest cell cultures were grown on glass petri dishes, which required rigorous cleaning to minimize contamination of cell cultures, and biological coatings such as collagen to enhance attachment [11]. The development of plastics in the mid-20th century proved a boon for cell biologists who quickly adopted commercially manufactured disposable polystyrene as the preferred cell culture surface (Cooper 1961; Ryan 2008). While polystyrene itself is a poor substrate for cell adhesion, processes such as gas plasma treatment produce a surface that supports a wide variety of cell types [12]. Coating the surface with polypeptides or glycoproteins can also improve cell adhesion [13].

Cell biologists made these efforts to standardize cell culture conditions for a reason: if genetically similar cells are cultured in consistent conditions, one can minimize misleading variations in cellular behaviors. This renders any experimental effects easier to recognize. In some instances, small variations in environmental conditions can induce profound changes in cell behavior.

Cells interact with the environment in a number of distinct ways. These interactions may be in several forms: (i) chemical factors, which are dissolved in the extracellular media, bind to receptors on the cell membrane, and invoke intracellular signals; (ii) cell-cell interactions, in which receptors on one cell recognize molecules on another cell; and (iii) cell-matrix interactions, in which cell receptors recognize molecular motifs on the ECM. Cells can also detect the shape and stiffness of their substrate based on tensions experienced within their cytoskeletons. Furthermore, cells are capable of responding to extracellular and intracellular bioelectric stimuli. All these stimuli provide environmental information to the interior of the cell. The cell may respond with changes ranging from simple modulations in cell shape to alterations in gene expression. Inside the body, cells constantly receive these signals from secreted factors in the interstitial fluid, contact with adjacent cells, contact with the interstitial matrix, and mechanical tensions produced by growth, development and organism movement. Researchers have made major efforts to model these influences in the *in vitro* environment.

It is easy to dose a population of cells with a chemical factor, but targeting a single cultured cell, or part of a cell, with is a greater technical challenge. The traditional method has been to deliver the agent via a pipette tip or drawn capillary positioned close to the cell of interest, but it is difficult because diffusion typically results in shallow concentration gradients, and it is difficult to selectively target a site on a single cell. Patch clamping allows more precise (generally internal) dosing but risks damaging the cell.

Even the gentlest handling exerts stress on the cell membrane, and this may act as a stimulus itself. Photolytic cleavage, the release of "caged" chemical agents by light, can deliver reagents with high spatiotemporal resolution, although preparation of photolytic agents can be difficult [14]. An advance in cell dosing technology developed by the Shear lab uses a microfluidic device consisting of two vertically stacked flow chambers, with cells adherent to one face of a membrane that also functions as a barrier between flow cells. Ablation of a pore in the membrane using a focused laser light allows a narrow stream of dosing reagent from the lower chamber to flow into the upper cell chamber. Changing the direction of fluid flow in the upper chamber allows the stream to be precisely steered toward cells of interest and multiple cells can be dosed with different reagents in arbitrary patterns [14]. This technique has been successfully used to examine the chemotaxis of HL-60 leukemia cells with subcellular resolutions [15].

Electrical signals, both dynamic and steady-state, are known to influence cell division, migration and differentiation [16]. Transmembrane potentials and ion channel currents have been extensively studied using intracellular microelectrodes and patch clamp electrodes [17]. Spatial voltage gradients in the extracellular and intracellular spaces have attracted recent research attention. The application of electric fields to cell cultures has been used to direct axon extension [18,19] and fibroblast migration [20].

Cell adhesion and morphology is influenced by the chemistry of the surface to which cells adhere. Within organisms, these surfaces may be other cells or ECM. In *in vitro* environments, adhering surfaces are generally glass or polystyrene which may be chemically functionalized or coated with substances that promote cell adhesion. In the 1960s, systematic studies explored how surface characteristics affect cell cultures. Researchers soon realized that surface adhesivity, topography, and stiffness all have distinct effects, and careful attempts must be made to isolate and distinguish these influences.

The varying affinities of cells for different surfaces have been exploited by researchers to produce micropatterned surfaces on which cells favor the chemistry of some regions over others Early efforts in micropatterning used metal or polymer deposition to modulate the native hydrophilicity and/or hydrophobicity of surfaces, and hence their cell adhesive properties [21–26]. Cell surface receptors bind to biological molecules such as polypeptides, glycoproteins and their derived peptide, so cell culture surfaces bearing these molecules were developed via self-assembled monolayers or chemical immobilization [26,27].

In the mid-1980s, biological micropatterning research was driven by basic research into cell function and applied research into devices such as biosensors, prosthetics, and biological computers, on which electrically active cells needed to be spatially distributed into circuits [28]. In product of this intersection of biology and engineering, microfabrication techniques developed in the semiconductor fields were used to functionalize cell-adherent surfaces in diverse and high-resolution micropatterns [24,26]. These techniques include photolithography, microstamping, microfluidic patterning, and stenciling [29,30].

The Shear lab, in collaboration with the lab of Dr. Christine Schmidt, has patterned soft protein hydrogels with biological molecules using multiphoton photochemistry. Protein matrix structures are fabricated via multiphoton lithography (micro-3D printing), and then photochemically functionalized with biotin. Via a neutravidin linker, a wide variety of biotinylated bioactive molecules can be tethered to the printed structures, thereby providing a combination of physical, mechanical, and chemical cues to cells cultured on the printed structures [31].

In general, two-dimensional cell culture surfaces are poor models for the three-dimensional environments that cells experience in native milieus [32]. Where an *in vivo* cell may contact a number of cells and/or extracellular matrix (ECM) in several directions simultaneously, a cell in a conventional monolayer culture environment typically experiences a substrate on the ventral side, a fluid environment on the dorsal side, and possibly some cells in lateral directions. Cells may also grow over each other, producing multilayer cultures. Many cells display different behaviors depending on the dimensionality of their environment.

Researchers have made several attempts to culture cells in conditions that better model their three-dimensional *in vivo* environment. A technique known as histoculture, in which intact tissue fragments are supported on collagen gels in growth media, maintains cells in their *in vivo* structural arrangements and has enjoyed clinical success as a drug response assay [33]. In 1979, researchers successfully cultured disaggregated cells that were embedded in collagen and other biologically-based gels [34]. Since then, cell functions observed in three-dimensional environments have been shown in a number of cases to better reproduce those that occur *in vivo*, and depending on chemical and other properties, to support development of defined differentiation states. [35]. For example, the Shear lab and the Schmidt lab have developed a three-dimensional cell culture substrate for angiogenesis. A photocrosslinkable fibronectin conjugate is incorporated into a three-dimensional hyaluronic acid hydrogel network. Endothelial cells cultured within these hydrogels display proliferation and migration, and attain an angiogenic phenotype [36].

More recently, researchers have increasingly focused on the dynamic nature of *in vivo* conditions. Cell morphology, migration and other properties can be time variant and observations often must be made in real time to capture transient features [30,37,38]. For instance, cell-level changes can be monitored through various time-lapse microscopy modalities. In some cases, fluorescent markers are used in combination with dynamic imaging methods to track the presence, localization and configuration of molecular species over a variety of relevant time scales.

There have been fewer studies that subject cells to dynamic cues to invoke behavioral responses. The technological challenges of creating dynamic environments have only recently been overcome through the development of stimuli-responsive materials. Many “smart” polymers undergo physical transitions at different temperatures, and these properties have been exploited to prepare surfaces that transition between cell adhesive and non-adhesive conditions [39]. Shape-memory polymers are being used to develop substrates that change their topography in response to temperature changes [40–42]. Other substrates transition in response to photochemistry [43], electrochemistry [44], ‘click’ chemistry [45], and applied forces [46].

1.2 THE BEHAVIOR OF CELLS ON SURFACES

Paul Weiss’ experiments in the 1920s drew attention to the fact that adherent cells, particularly fibroblasts, tend to grow aligned to fibrin filaments in a plasma clot culture [47]. Cells were also shown to align with collagen bundles inside a fish scale, to glass streaked with lipids, and to glass scored with fine lines [48,49].

Certain behaviors occur in a wide range of cell types, often produced by very similar mechanisms. Adherent cells thrive when attached to a substrate, and are generally rounded in suspension but flatten and spread out on flat surfaces. They may be stationary or motile, and their paths on isotropic surfaces can appear random or be directionally persistent [50]. On surfaces that are anisotropic with respect to adhesion, chemistry, biological activity, topography or mechanical properties, the cells display preferences for some surfaces over others. These preferences manifest as changes in cell shape (stellate versus bipolar or spindle, shown in Figure 1.1) or speed of movement.

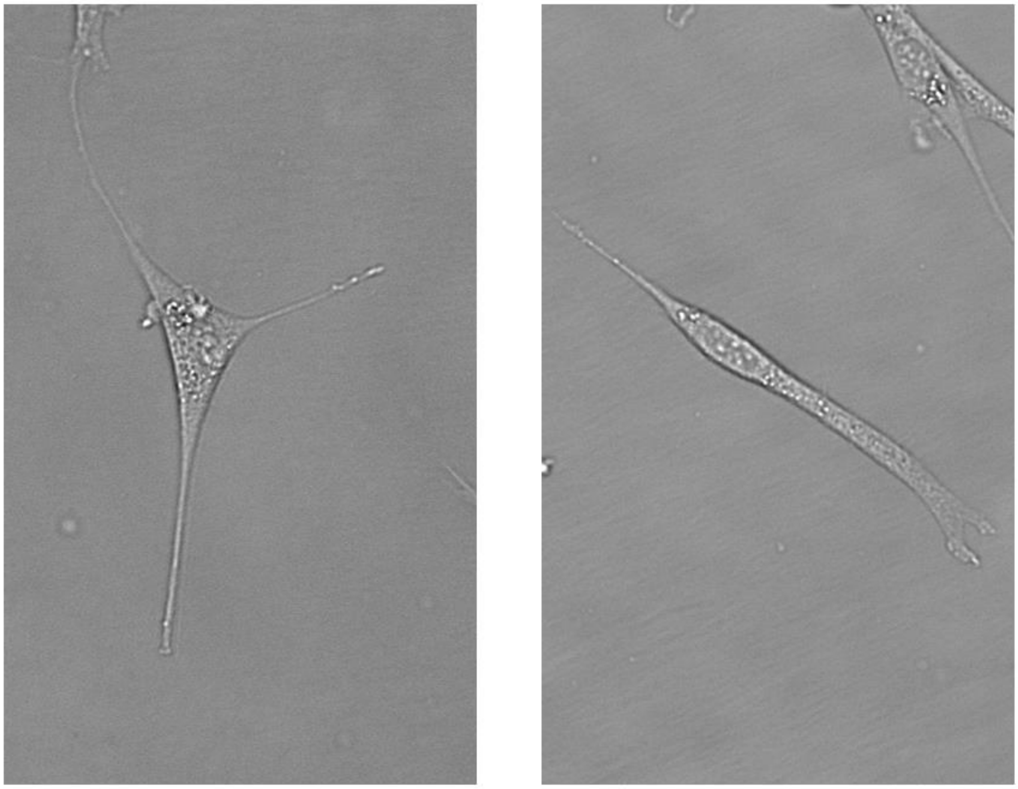

Figure 1.1: Common morphologies of NIH-3T3 fibroblast cells. Stellate on left and bipolar or spindle on right.

Some cells, particularly fibroblastic cells, display a behavior known as contact inhibition [51]. If the leading edges of cells encounter each other during the course of movement, both undergo a temporary cessation of motility. The cells either remain stationary or change direction and move apart. Proliferation also slows down or ceases. Contact inhibition prevents cells *in vivo* from overgrowing. This behavior is a hallmark of well-functioning cells and its absence often indicates abnormality and pathology [52].

Fibroblasts have long served as a model to elucidate the mechanisms of cellular behavior [48]. They are prolific inside the body, forming an important component of connective tissue and secreting the ECM proteins that comprise the stroma of animal tissues. Chick embryonic fibroblasts have historically been a popular experimental cell type, as chick embryos were a readily available source of animal tissue before the advent of commercial cell culture. Fibroblasts display easily observed changes in shape and migration patterns under different circumstances.

Other cells also display characteristic responses to surface effects. Neuronal cells extend processes called neurites to establish connections with other cells, and the direction of neurite growth can be guided using surface cues. Progenitor cells such as mesenchymal stem cells differentiate into various cell types when plated on different surfaces [53].

The work in this dissertation focuses on the response of neuronal and fibroblastic cells to topographical cues. Since morphology and motility are influenced by the same cellular machinery, the mechanisms of both behaviors are detailed in the next section.

1.3 MECHANISMS OF CELL MOTILITY AND RESPONSE TO TOPOGRAPHY

In the first half of the twentieth century, cell biology underwent a transition in approach from a descriptive science to a mechanistic one. Paul Weiss was a vocal proponent of considering the cell as a complex entity that interacted with its environment and modified its behavior in response to specific conditions [48]. He paid particular attention to fibroblasts, which display a distinct range of morphologies in response to substrate conditions. Notably, fibroblasts become elongated and narrow when plated upon surfaces with certain anisotropies. Weiss called this morphological response "contact guidance" and made some of the earliest attempts to explain the mechanism of this behavior. He attributed the shapes of cells to the outcome of competition between two opposing sets of forces experienced by the cells. Cohesion, viscoelasticity, surface tension, and contractile fibrous networks would minimize the surface area of the cell and draw it into a sphere, while adhesive forces at cell margins, inertia, and radial contractile forces would pull the cell outward [49]. In light of later studies, this was a remarkably good prediction although the cytoskeletal and adhesive forces turned out to have an overwhelmingly stronger effect than the viscoelasticity of the cytoplasm or the surface tension in the cell membrane.

1961 was an important year in which many experts presented reviews of current knowledge on cell motility behavior and attempted to fit observations into theories. Abercrombie summarized the contemporary understanding of fibroblast locomotory behavior and proposed a framework of hypotheses about its mechanisms [51]:

1. The fibroblast bears a ruffled membrane which is its main locomotory organ.
2. An isolated fibroblast on a plane surface moves randomly.
3. Multiple ruffled membranes on one cell compete with one another to determine the direction of cell movement.
4. Ruffled membranes can be inhibited by the environment’s heterogeneities, leading to phenomena such as contact guidance and contact inhibition.
5. Cells form adhesions with one another.

In the same year, Ambrose observed fibroblasts with interference and surface-contact microscopy and implicated “contractile fibrils lying just within the cytoplasm and parallel to the cell surface” in the locomotory undulations of the ruffled membrane [54]. Ingram made a similar suggestion in 1969 after examining a side view of moving fibroblasts, using an ingenious culture chamber that allowed microscope imaging parallel to the cell culture surface [55]. Over the next decade, evidence accumulated to support the theory that intracellular machinery, coupled to adhesion sites on the cell surface, drives cell morphology and movement. Several other theories fell by the wayside for lack of evidence, such as Weiss' belief that cells migrate by following tracks of macromolecular exudates [49] and Carter's theory that cells are passive entities whose movement is driven by thermodynamics [56].

A major milestone in the understanding of cell movement was reached in 1970 with a series of five papers presented by Abercrombie, et al. [51,57–60]. The researchers described the motion of the ruffled membrane, now termed the "lamellipodium", as a cycle of protrusions and withdrawals. The overall movement of a cell occurs when an amount of cellular material is thrust forward in the form of lamellipodia, and pulls the remaining cell body forward. Electron microscopy of the cell revealed small clusters of material connecting the cell to the substrate, and longitudinal filaments within the cytoplasm. This was the first indication that adhesion sites attach the cell to the substrate, providing traction, and that cytoskeletal stress fibers contract to pull a cell forward [61]. Cell movement was thus shown to be an active cell-driven process and not the product of passive physical interactions between the cell and substrate. An illustration of the leading edge is shown in Figure 1.2 [62].

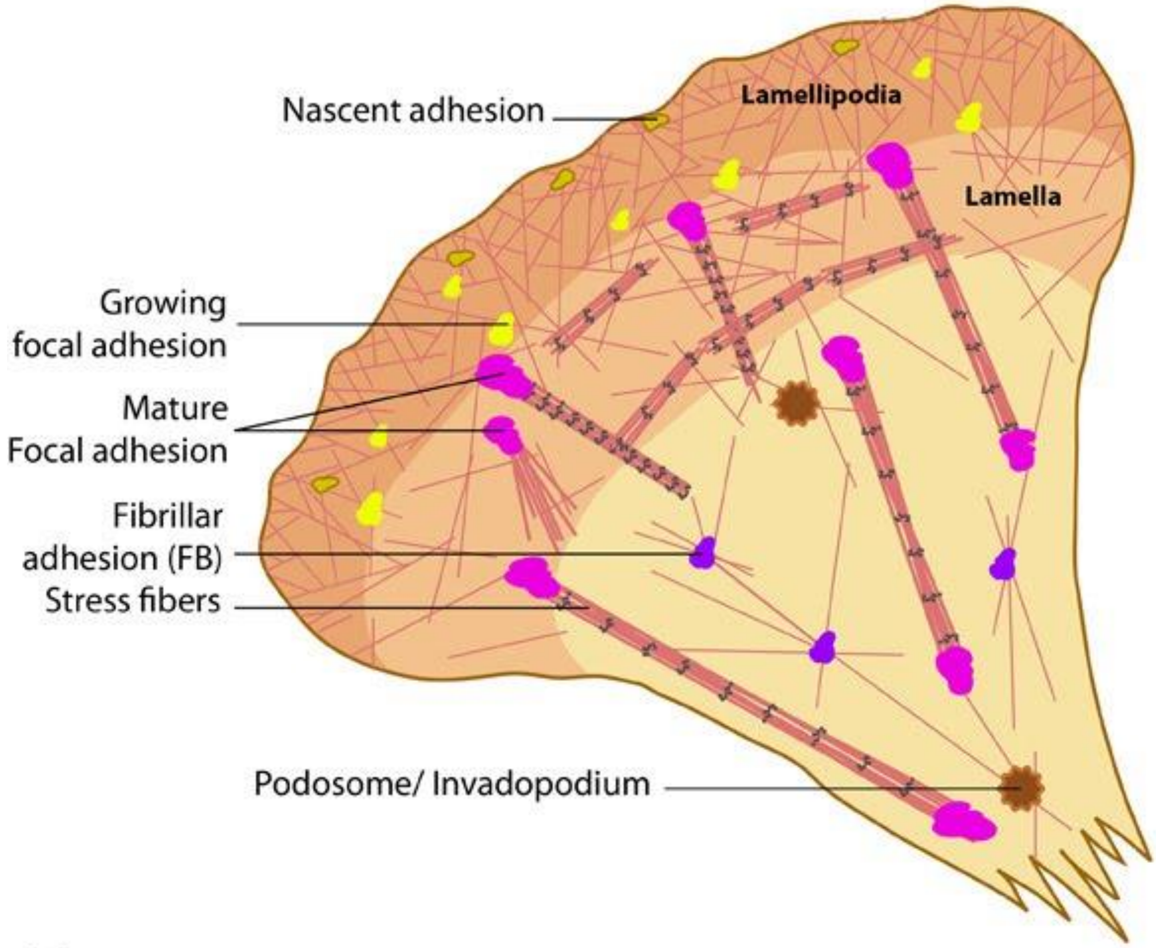

Figure 1.2: Leading edge of a cell. Important features such as the lamellipodia, lamella, actin stress fibers, and adhesions are labelled. Used with permission from MBInfo: www.mechanobio.info; Mechanobiology Institute, National University of Singapore.

The nature of the contractile cytoskeletal stress fibers was identified as actin, a protein known to be involved in intracellular contraction, when Lazarides and Weber in 1974 showed that the fibers could be visualized via fluorescent actin-antibodies [63].

The filopodia, spike-like projections on the surfaces of cells, were observed by Albrecht-Buehler in 1976 on fibroblasts probing the substrate around the cell [22]. When they identify favorable surfaces, the lamellopodia extend into that region. The observations suggested that filopodia have a substrate exploring function, and this finding brought the field closer to a mechanism for cell movement.

By the mid-1980s, the mechanism of cell motility was broadly established as follows:

1. Filopodia probe the substrate around the cell and identify regions on the substrate favorable to the cell.
2. Lamellopodia thrust forward and form focal adhesions to the favorable substrate.
3. The cytoskeleton contracts, dragging the cell body in the direction of the lamellopodia.
4. Older focal adhesions pass underneath the cell until they become part of the rear edge of the membrane.
5. Finally the adhesions in the rear detach and the membrane is pulled toward the cell body.

On planar surfaces, the individual motile steps comprise a random walk. On surfaces that promote cellular alignment, the cells take on a bipolar morphology.

One particular feature of cell behavior that has attracted considerable interest is contact guidance, or “topographical response” as the contemporary convention describes it [64]. Many cells, particularly fibroblasts, tend to change their shape in response to topographical anisotropies; the mechanisms that underlie this behavior have motivated significant research interest. It is important to emphasize that the term “contact guidance” specifically excludes the effects of substrate chemistry and the alignment effects seen in high density cultures as a result of contact inhibition [65]. Relevant surface topography can vary from the nanoscale to the microscale. It can influence cell adhesion strength, cell orientation, cell movement, activation of cellular machinery, and gene expression.

Mechanisms that control orientation are of particular interest in the context of this dissertation. Several mechanisms have previously been proposed to explain why cells plated on a grooved substrate develop bipolar morphology in a direction parallel to grooves. At the most fundamental level, cells react to topography by preferentially extending and adhering to the substrate in certain directions over others. A key question is: what drives this selective preference?

Dunn and Heath observed that cells growing on smooth glass cylinders tend to preferentially extend along the axial direction of the cylinder, and this effect is more pronounced on cylinders with smaller diameters [65,66]. They hypothesized that cells limit their extension in directions of high curvature in order to minimize the bending of the cytoskeleton, but this theory is contradicted by the alignment of cells on grooves with pitches shorter than the length-scale of cells [67]. O'Hara and Buck suggested that cell alignment is an outcome of the asymmetric formation of adhesions in configurations geometrically favored by the underlying topography [68]. Curtis and Wilkinson proposed that topographical features between adhesion sites may produce tensions in the cell membrane, which are detected by stretch receptors and transduced into the intracellular signaling systems [64]. These stretch receptors would also be activated if the cell attempted to extend along the circumference of a narrow cylinder.

Evidence to support or disprove these theories was provided by the tremendous advances in molecular biology techniques developed in the 1980s and 1990s. Techniques such as immunohistochemistry, fluorescence-tagging, genome manipulation, and various advancements in live cell imaging (such as total internal reflectance microscopy and differential interference contrast microscopy) helped researchers identify subcellular structures such as actin bundles, microtubules, and focal adhesions. Knowledge of these structures, and their locations and functions, helped develop the widely-accepted cell motility models of the present day.

Cells are now understood to adhere to surfaces in the following manner. Newly plated adherent cells are round and inactive, apart from some filopodia that probe the environment (Figure 1.3(a)). When these projections detect a surface coated with ECM ligands, they form initial attachments with the substrate and the cell starts to spread. The cell body flattens as actin filaments in the central region of the cell are disassembled. Cell spreading proceeds through a fast continuous phase as actin filaments reassemble in the periphery where the lamellipodia are located around the cell margin (Figure 1.3 (b)). At the boundary between the lamellipodia and cell body is a region called the lamella, which contains a relatively stable branched actin network. The lamellipodia contain a more dynamic network of branched actin filaments which extends and spreads the lamellipodia over a larger surface area. The assembly of the actin network determines the rate of cell spreading and it is continuous, so cells spread uniformly on flat, isotropic surfaces. On anisotropic surfaces, actin assembly is discontinuous and inactive in large sections of the cell margin, leading to asymmetric spreading. The continuous spreading phase is followed by a slow contractile phase in which the edge of the cell extends and withdraws in a cyclic manner while testing the rigidity of the substrate [69,70] (Figure 1.3 (c) and (d)).

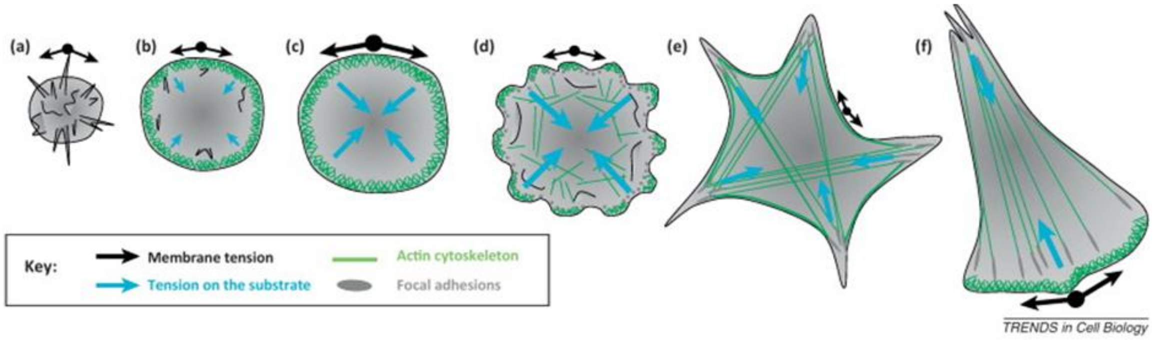

Figure 1.3: Spreading of a cell on a substrate. From initial rounded shape (a) to fast, continuous phase (b), that transitions (c) to a slow contractile phase (d), and finally a fully spread state (e). The establishment of leading and training edges gives the cell polarity (f). Image used with permission from Elsevier [71].

As cells reach their fully spread state (Figure 1.3 (e)), the lamellipodia develop stable adhesions called focal complexes on their ventral sides. The focal complexes grow up to a few hundred nanometers in diameter through the assembly of several hundred types of small proteins including integrins, which are transmembrane receptors coupled to the actin cytoskeleton [71]. Eventually the cell spreads fully and establishes a polarity (Figure 1.3 (f)), i.e. it develops at least one leading edge as well as trailing edges.

Lamellipodia extend because their dynamic branched actin network is continually polymerizing at the ends, and thrusting the cell membrane forward. As the lamellipodium thrusts forward, the network itself undergoes a relative backward motion known as retrograde actin flow. The retrograde actin flow applies stress to the stationary nascent adhesions and encourages them to develop into mature focal adhesions (FA). Meanwhile, the ventral cell membrane, anchored to the underlying substrate via focal complexes, is stationary relative to the lamellipodium so by the time the FA completely mature they are under the lamella. Further forward movement of the cell brings the aging FA toward the rear of the cell, while new FA develop at the leading edge.

The interplay of FA, actin microfilament bundles, and microtubules control the contractility and motility of the cell. In addition to the branched actin network in the lamellipodia and lamella, there are other actin filaments that organize into bundles in response to the maturation of focal adhesions. These actin bundles are coupled to the intracellular domains of FA and apply stress forces to the latter when myosin II motor proteins drive contraction of the actin cytoskeleton.

FA have the interesting property of growing in size when they experience applied tension, and disassembling when the tension is removed. As they grow in size, they couple to yet more actin filaments, thereby increasing the stress they experience. Because of this feed-forward mechanism, the FA could grow large enough to impair cell motility and induce excessive contractility of the cell. Microtubules play a regulatory role by disrupting the unchecked growth of FA, and interrupting the feed-forward loop [64].

One advantage of the cell's contractile machinery is that it allows the cell to "test" the rigidity of the underlying substrate. As the actin cytoskeleton contracts, FA, anchored to the extracellular substrates, resist movement and transmit tension to the actin bundles. These tensions are integrated and lead to the release of signaling molecules that act on downstream effectors and ultimately reorganize the cytoskeleton. If the surface is appropriately rigid, the signals direct the actin stress bundles to undergo polymerization and extend the cell further. The cell binds to the new region, probes yet further with its leading lamellipodia, and the process continues cyclically.

The forward thrust of the leading edge and the contractility of the actin cytoskeleton are important parts of the cell motility machinery. Adhesion to a new surface followed by contraction leads the bulk of the cell body to translocate in the direction of the leading edge. However, the trailing edge of the cell needs to detach from its adhered surface and retract toward the cell body in order for the cell to complete its movement.

The cytoskeletal contraction stresses FA on both the leading and trailing edges, in essence creating a “tug-of-war” between the two ends of the cell, with the cell body being pulled toward the “victor” while the “loser” detaches from the surface. The leading edge generally wins this competition because its FA are stronger. The trailing edge is attached to the substrate by aging FA, which are weaker because of a breakdown of adhesive components [72].

The shape of a cell, during motility and otherwise, arises from an interplay between the cytoskeleton, the adhesion sites, and the cell membrane as it stretches between them. The filamentous actin cytoskeleton undergoes rearrangement driven by actin polymerization dynamics in response to signaling molecules generated by environmental cues. This cellular machinery is implicated in the response of cells to underlying topography, such as grooved substrates.

Many cells, particularly fibroblasts, respond to grooved topographies by elongating and developing a bipolar morphology. The complete set of mechanisms has not been elucidated but it appears that filopodia, the finger-like projections that sense cells’ surroundings, are more likely to form parallel to grooves because the perpendicular configuration is subject to unfavorable stress. The bias in filopodia formation propagates to biases in leading edge advancement, cytoskeletal rearrangement, and movement. These influences collectively shape the cell into a bipolar spindle [53,73], with a very narrow lamellipodium [74] .

Efforts in cell motility research has shifted in the direction of a complete identification of cellular components and their interactions, thermodynamics, kinetics, and mechanical characteristics [72]. The hope is that by modeling the molecular machinery completely, researchers will be able to model the mechanisms of cell motility on a molecular level and thereby learn to predict and control the migration of cells. However, the computational demands of these models have increased as the number of identified molecules has burgeoned. Focal adhesions alone are comprised of over 150 distinct molecules [69]. Identifying their functions is yet more time-consuming because it often involves observing cell responses after the molecule of interest is disrupted by drugs or gene modification. The process is complicated by the fact that many molecules act in concert to function effectively, and cells have evolved many redundancies to compensate for natural mutations. Where cell biologists began with observations on cell behavior and sought mechanisms to explain them, we are now at a point where we have a plethora of "mechanisms in search of functions" [64].

Many computational models of cell migration focus on the scale of individual cells or cell populations. A large number of models for 2D migration have been developed over the past twenty years [75]. More recently, models are being developed to capture cell behavior in 3D environments to reproduce *in vivo* conditions more closely [76]. Several important distinctions have been found between cell behavior in 2D and 3D cultures, for instance there is controversy over whether FA develop in 3D environments of if they are artifacts of culturing cells on a 2D surface [77].

Many aspects of cell morphology and motility have been elucidated by varying characteristics of the culture surface and observing how cells react. The next section describes these surface modifications and their effects.

1.4 MANIPULATING SURFACE TOPOGRAPHY

The oriented growth of cells on grooved substrata was observed early on the history of cell culture [78], and investigations into this phenomenon have driven many discoveries in the area of cell behavior and motility. Many researchers theorized that grooved areas provided cells a different degree of adhesivity versus ungrooved areas, perhaps because the groove-carving process exposed adhesive sites within the bulk of the substrate. But adhesivity did not explain why, in a similar phenomenon, cells growing on a glass cylinder preferred to orient parallel to the axis instead of the circumference [79]. Rovensky et. al. [80] responded by molding grooved substrates out of polymers, thereby eliminating differences in chemistry between the carved and uncarved surfaces. They noted that cells plated on the substrate migrated out of the grooves and onto the plateaus between grooves, and this trend increased with groove depth. The researchers concluded that cells migrated away from grooves not because of chemistry-related adhesive effects or microstructural heterogeneity, but because of the latters' geometric configuration.

Dunn and Heath also attempted to distinguish between chemical and physical effects, and plated fibroblasts on cylindrical glass fibers of different radii [66]. The cells aligned parallel to the longitudinal axis, particularly on the fibers of small radii. The researchers concluded that substrate shape can influence cell alignment in the absence of chemical heterogeneity, and hence topographically-induced contact guidance is a distinct phenomenon from adhesion-induced alignment [65].

Grooved substrates were initially produced by mechanically scoring lines through a rigid metal or plastic sheet [80]. These grooves had poor reproducibility and researchers could not vary parameters such as depth, width and shape independently [81,82]. During the 1980s, many techniques originally developed in the semiconductor industry were adapted to create cell surface topographies [83]. These include micromachining, ion milling and photolithography [81,83,84]. Improved control allowed researchers to explore a wider range of topographies, such as pillars, pits and tunnels, but variations on the groove pattern remain the most popular [74].

With better control over groove dimensions, researchers found that the minimum dimensions that cells respond to can be as shallow as 75 nm and narrow as 100 nm [73], but different cell types display different sensitivities. Cells orient to grooves increasingly with groove depth. With narrower grooves, cells span several grooves at a time, adhering mostly to the plateaus between the grooves. If grooves are much wider than cells, oriented behavior decreases, although cells may align to one edge [74]. Topographies of pits and posts have been shown to affect cell spreading, but these responses have not been as extensively studied as groove responses [53]. Cell responses to these influences are probabilistic rather than deterministic.

Examining cellular structures provides clues to how the cells interact with these features. Microtubules are the earliest structures to align with grooves. The actin cytoskeleton remodels so that filaments are parallel to grooves, and focal adhesions align along the edges of grooves and plateaus [85,86].

Neurite guidance is a special case of contact guidance that occurs in neuronal cells. Neurites are projections extending from the bodies of neuronal cell types, such as neurons and neuroblastoma-glioma cells, and they can mature into axons and dendrites which play an important role in cell-cell communication by transmitting electro-chemical signals from one cell to another via synapses. At their ends, neurites possess a pathfinding structure known as a growth cone, illustrated in Figure 1.3 [87]. This complex structure contains many molecular components such as receptors and adhesion molecules to interact with the environment, and a cytoskeleton that drives the growth cone to probe the surroundings and pull the cell body forward. There are also signaling molecules that integrate signals from the environment, modulate the forces on the cytoskeleton, and influence gene expression [88]. Much of the cellular machinery in the neurites is similar to the cell motility machinery for fibroblasts described earlier.

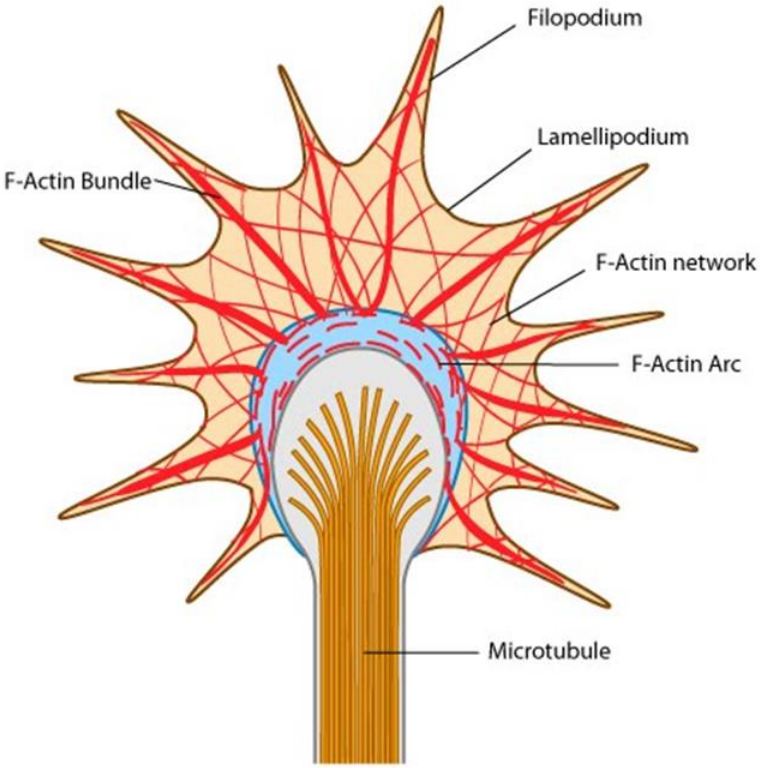

Figure 1.4: Growth cone of a neuronal cell. It contains many structures also found in the leading edges of cells, such as the lamellipodia, actin stress bundles, and microtubules. Used with permission from MBInfo: www.mechanobio.info; Mechanobiology Institute, National University of Singapore.

Neurons are capable of connecting via synapses to form networks. Electrochemical signals between cells produce a functional circuit capable of signal transduction [89]. An electrical signal travels from a cell body down one neurite, and converts to a chemical signal that crosses the synapse (an intercellular junction), and in turn may lead to a change in the membrane potential of the second cell. If the second cell is a neuron, post-synaptic processing determines whether it further propagates the signal. Networks of these cells and synapses are capable of complex computational activities in, for instance, the central nervous system where they perform functions such as balance maintenance and cognition [90].

Understanding the connectivity patterns and the resulting functions of nervous system networks is an important goal in neuroscience, with applications including the repair of damaged nerves, the formation of brain-computer interfaces and the creation of biosensors. Such goals are difficult to accomplish using brain tissue slices because the dense arrangement of neurons and synapses limits the resolution at which the networks can be probed. There have been attempts to recreate two-dimensional cell networks in culture at resolutions that facilitate examination with current technology, but without the developmental cues available in intact tissue, cells extend neurites and form synapses in an unguided and random manner. Neurite guidance usually involves the use of chemical and/or physical cues to direct the growth of neurites. Neurite guidance technologies allow researchers to culture networks of neurite-producing cells with experimentally-imposed connectivity patterns that drastically reduce the network complexity, enabling studies on electrochemical signal processing [91,92].

Neurite guidance in cell cultures has been demonstrated by the application of diffusible neurotropic factors. Early techniques used micropipettes to deliver factors into culture media near the growth cone of interest [93]. Since factors delivered in this manner dissipate quickly in the bulk media, microfluidic chambers were developed for the establishment of stable gradients of soluble guidance cues [94].

Several neurite guidance techniques work by modifying the neurite growth substrates by modifying them so that at least two types of surfaces are presented to cells. The favorable surfaces are often presented as “pathways” for neurite growth, surrounded by unfavorable surfaces. Neurites respond by extending on the favorable surface while avoiding the unfavored one. Surface modification may be chemical, involving immobilized micropatterns of proteins [95], biopolymers [96,97], or genes [98]. Chemical patterning is achieved by a variety of techniques including photolithography (using photoresist to protect or expose selected surfaces for modification) [99], microcontact printing (in which an elastomeric stamp is used to print chemicals onto a surface) [100], and microfluidic deposition (in which chemicals flowing through a microfluidic device are deposited at precise locations) [101]. Surface modification may also be topographical. Neurites follow grooves that are etched into the growth substrate by laser ablation or photolithography [74,102,103], or molded onto the substrate by soft-lithography methods [104]. Another technique uses tunable hydrogels to present neurites with surfaces of varying stiffness, some more favored by neurites than others [105]. Although such immobilized chemical and physical patterns are effective for manipulating cells, neuronal or otherwise, that are cultured upon them, they are limited because they typically cannot be introduced to a growing culture or modified after initial fabrication.

Crosslinked protein structures can create a three-dimensional pattern that provides contact guidance to neurites at a resolution down to ~250 nm in three dimensions [106]. These structures can also be functionalized with a range of molecules to provide chemical guidance cues. Previous work in the Shear lab has demonstrated neurite guidance by dynamically building topographical features on the growth substrate *in situ* using micro-3D printing [107].

The mechanical properties of the substrate also affect cell behavior. Cells sense the rigidity of the underlying substrate through the force exerted on focal adhesions during cytoskeleton contraction. If the focal adhesions are bound to a soft and flexible surface, the substrate yields under the contractility force and the net force on the focal adhesions is lower than it would be on a rigid, unyielding surface.

Compared to chemical and topographical influences, studies of mechanical influences on cells have a relatively recent history. Because of technological limitations, it wasn't until the 1980s that flexible cell substrates could be reproducibly prepared and characterized [65]. Since then, substrate rigidity has been shown to affect a wide range of cellular properties including morphology, spreading, focal adhesion formation, proliferation, apoptosis, gene expression and differentiation [108]. Substrate materials preferred for these applications have mechanical properties that can be controlled without substantially changing the surface chemistry. In 1997, Pelham and Wang successfully prepared a substrate on which biological and mechanical properties could be independently controlled, using polyacrylamide gels coated with collagen, and they showed that NIH3T3 and other cells are less likely to spread and migrate on compliant surfaces than on hard surfaces [109]. Improved cytocompatibility is seen with poly(ethylene glycol)-based hydrogels [108].

Accumulating evidence suggested that cells are likely to respond if their membranes experience strong mechanical tension. Applied force can expose cryptic peptide sequences, open mechanosensitive ion channels, and stimulate the strengthening of receptor-ligand interactions [110]. In 1999, Mooney et al. demonstrated that smooth muscle cells plated on an elastic substrate, when subjected to cyclic strain, aligned parallel to the axis of stretching and the resulting tissue grew stronger [111]. In the same year, Sznadjer et al. showed that the activity of Na^+-K^+-ATPase increased in alveolar cells under cyclic stretching [112]. Cheng et al. evoked an electrical response from a single sensory nerve by indenting the elastomeric substrate [113].

More recently, attention is being directed toward capturing the dynamic behaviors of the *in vivo* environment and replicating them *in vitro*. The body is not a static system, and at any given time cells experience changes in topography, chemistry, temperature, and mechanical tension. Static *in vitro* environments fail to expose cells to these dynamic cues and this is one reason that cells do not behave as they do *in vivo*. “Smart”, or stimuli-responsive, systems can provide the dynamic conditions needed to reconstruct *in vivo* conditions. These have been applied to 3-D cultures [114], topography [40–42], or microfluidic systems [115].

One method to introduce dynamic topographies to cell culture is to create substrates from shape-memory polymers. These materials are cast in a thermodynamically stable shape, and then molded into another temporary shape. A switch, such as a temperature change, can trigger a reversion to the original permanent shape, which the material “remembers” via its molecular configuration. Substrates made with poly-(ε-caprolactone) have been used to provide fibroblasts and human mesenchymal stem cells with an initially grooved substrate that switches to a flat substrate. Cells change their morphology from aligned and bipolar to stellate [40,41].

Another strategy is to selectively erode parts of the substrate. Tibbitt et al. demonstrated that two-photon excitation could be used to selectively degrade a PEG hydrogel substrate and thereby disrupt cell-substrate adhesion [116].

1.5 MULTIPHOTON PHOTOCHEMISTRY OF PROTEINS

To create topographically dynamic surfaces for culturing cells, the Shear lab uses an additive manufacturing technique called micro-3D printing. This technique exploits non-linear multiphoton excitation to achieve localized photocrosslinking of reagents by focusing a pulsed laser beam to produce a high photon flux. This high photon flux occurs in a small region because the light intensity of the focused laser beam approximately follows a Gaussian distribution; it drops off laterally as $1/\exp[-2r^2/r_0^2]$, where r/r_0 is the normalized distance from the optical axis, and axially as $1/(1 + z^2/z_R^2)$ where z/z_R is the distance from the focal plane normalized by the Rayleigh length [117]. As the rate of two-photon absorption is proportional to the square of the incident light intensity, the excitation of photosensitizers and initiation of photocrosslinking is limited to a prolate spheroid volume element ("voxel") on the order of a femtoliter in size. By translating the voxel through the reagent one can crosslink regions of one, two, or three dimensions, thereby building up structures of arbitrary shape. The feature resolution can be as small as a few hundred nanometers and structures can be tens or hundreds of microns in size [118]. At the end of the process, the unreacted reagent is washed away, leaving behind the intact printed structures as shown in Figure 1.4.

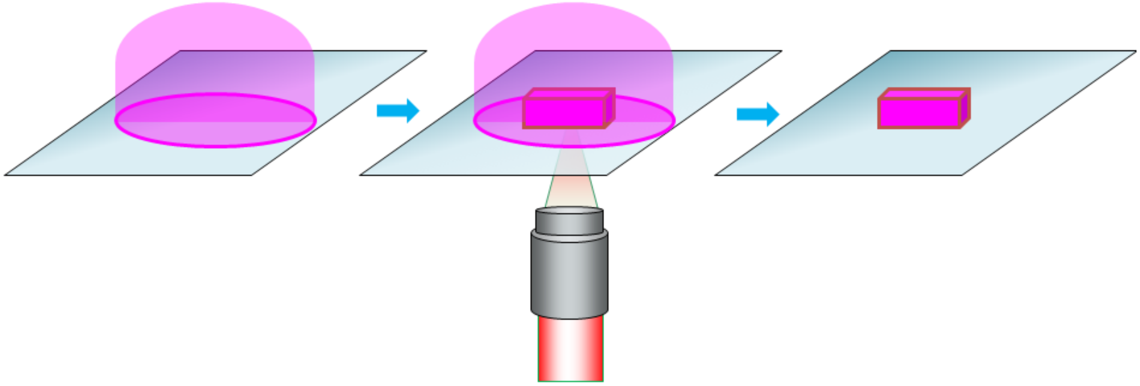

Figure 1.5: Schematic of micro-3D printing. Printing reagent is applied to a glass cover slip (left). A pulsed laser beam is focused into the reagent and translated to photocrosslink the reagent into a solid (center). The reagent is rinsed away, leaving a printed structure anchored to the glass (right).

The reagents used in micro-3D printing are monomers or macromolecules with photoreactive moieties. A photoinitiator or photosensitizer is often included to start the photoreaction or improve photoreaction efficiency. A solvent may be necessary to bring the reacting molecules into liquid or gel phase. Early developments of this technology took place in the late 1990s, using photopolymerizable resins, and monomers and oligomers with acrylate groups [119]. More recently, the Campagnola and Shear groups have achieved micro-3D printing with reagents consisting of proteins and photosensitizers [106,120–122].

The Shear lab introduced mask-based multiphoton photolithography by scanning the laser beam in a raster pattern via a galvo-mirror device and selectively passing it through a transparency mask [118]. This technique was extended to dynamic masks by introducing a computer-controlled digital mirror device (DMD) at the mask plane [123]. A rich variety of microarchitectures have been produced using this technique, particularly cellular microenvironments that are difficult or impossible to produce with other techniques. The technique also has the advantage of rapid prototyping, resulting in a shorter experimental cycle.

Multiphoton excitation is a non-linear optical phenomenon first theorized by Maria Goeppert-Mayer in 1931 [124], and experimentally demonstrated by Kaiser and Garrett in 1961 following the invention of the laser [125]. It is well-established in the field of fluorescence imaging because of its ability to photoexcite molecules with high spatial and temporal resolution [126]. At higher energy levels, it can be used to initiate photochemical reactions such as the crosslinking of proteins [106].

In the simplest case of two-photon absorption, a molecule with transition energy k between two states interacts with a photon of energy k/2 and enters a virtual state that persists for times of $\sim 10^{-15}$ s. If a second photon of k/2 energy interacts with it during this period, then both photons may be absorbed and the molecule transitions to the excited state. Because this phenomenon is non-linear, the rate of absorption is ideally proportional to the square of light intensity. Although this phenomenon is seen very rarely in nature because the necessary intensities are difficult to reach without quantum saturation or photobleaching, it can be induced readily in the lab by creating conditions in which multiple photons have a high probability of interacting with the same molecule within femtosecond timescales. This is commonly achieved by using low-duty-cycle pulsed lasers with high peak powers and pico- or femto-second pulse durations, focused through high numerical aperture objectives into small voxels. This produces a small region with a high photon flux where multiphoton absorption can take place [127]. Low average power lowers the total energy deposited in the system, and decreases cell damage in biological samples. Multiphoton excitation affords the advantages of reactions confined to a small voxel, reduced out-of-plane bleaching of photosensitizers, and greater penetration depth through the use of near-IR wavelengths [106].

After absorbing multiple photons, the excited photosensitizer can undergo intersystem crossing and enter a long-lived excited triplet state. When it relaxes to the ground state, the released energy can be transferred to an acceptor molecule that further undergoes a reaction [128,129]. Figure 1.1 depicts this process in a Jablonski diagram, where the acceptor molecule is molecular oxygen.

The photochemistry of multiphoton-excited reactions has not been explored as thoroughly as that of single-photon reactions. The selection rules for single- and multiphoton reactions are not the same and there is no guarantee that a molecule that absorbs a single photon will absorb two photons of half that energy. Therefore the multiphoton excitation spectra of molecules must be ascertained independently of their single photon absorbance spectra. The efficiency of two-photon absorbance of a molecule is quantified by the two-photon cross-section of that species. This value is given in units of Goeppert-Mayers (GM, equivalent to 10^{-50} cm^4 s photon^{-1}).

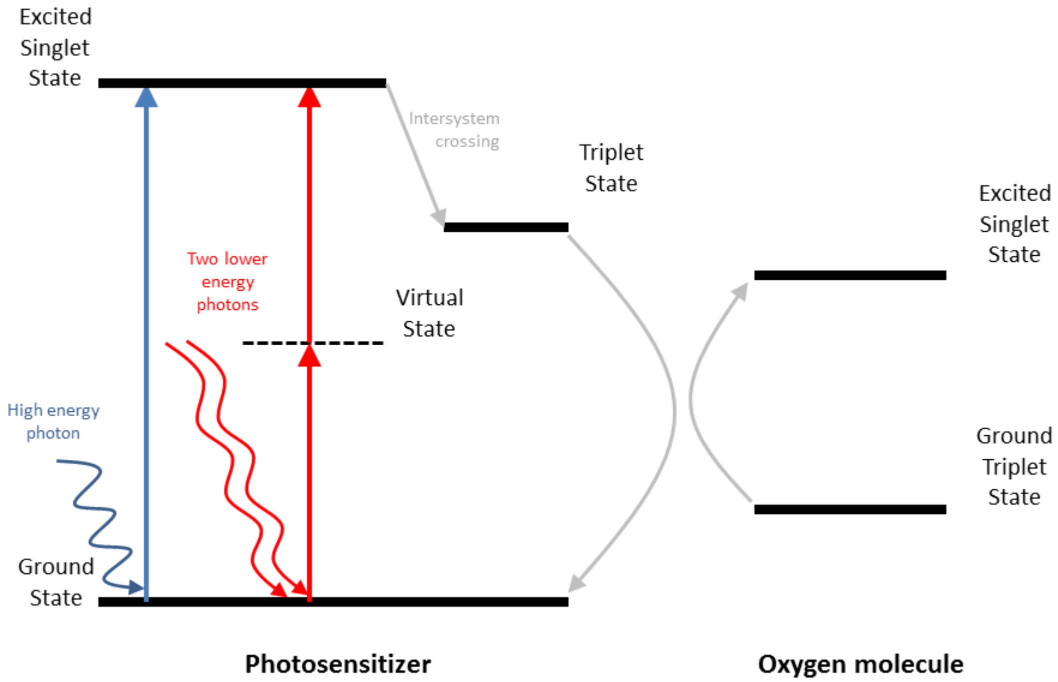

Figure 1.6: Jablonski diagram depicting single and two-photon absorption, and transfer of energy to produce singlet oxygen.

Photosensitizers, after excitation, can proceed through two reaction pathways referred to as either Type I or Type II. In a Type I reaction, the photosensitizers react with another molecule to produce free radicals. These radicals can react further with molecular oxygen to generate singlet oxygen and other reactive oxygen species. In a Type II reaction, shown in Figure 1.5, the photosensitizer transfers its energy directly to molecular oxygen, generating singlet oxygen [130]. In both pathways, the reactive oxygen species initiate photoreactions such as photocrosslinking.

Three photosensitizers are particularly relevant to this dissertation, flavin adenine dinucleotide, rose bengal and eosin yellow. Flavin adenine dinucleotide (FAD) is a biomolecule related to riboflavin (vitamin B_2). It is an enzyme cofactor involved in several metabolic processes and can be used as a photosensitizer in the presence of living tissue because of its low biological toxicity [107]. The two-photon cross-section at 740 nm is 0.08 GM. Rose bengal (RB) is a fluorescein-related synthetic dye first developed in the 19th for dyeing wool [131]. The earliest biological uses were as histological stains and intravenous assays, and it came to be used as a photosensitizer for photodynamic cancer therapies in the late 20th century. Eosin yellow ("eosin") is also a fluorescein analog used in histology as well as the cosmetics industry. It has lower cytotoxicity than rose bengal.

A number of biologically relevant materials have been developed using micro-3D printing, particularly in the class of materials known as hydrogels. Hydrogels are three-dimensional cross-linked hydrophilic polymer networks that are hydrated in aqueous solutions, and can have bulk properties ranging from very soft to very stiff. Edible jelly is a quintessential example of a material in this class. Hydrogels produced in our lab have been composed of poly(ethylene glycol) as well as proteins.

A wide range of proteins have been used as reagents for micro-3D printing, including bovine serum albumin (BSA), gelatin, apo-myoglobin and enzymes including alkaline phosphatase and cytochrome C [121,132,133]. Several amino acid residues are able to participate in photochemical reactions and form both intramolecular and intermolecular crosslinks. If there are enough intermolecular crosslinks between proteins in an aqueous environment, they can form hydrogels. Although the mechanisms have not been completely characterized, there is evidence that photo-oxidizable amino acid residues such as histidine (His), tryptophan (Trp), and tyrosine (Tyr) react with singlet oxygen to form species that react with other residues to form covalent crosslinks. Furthermore, lysine (Lys) is readily attacked by other residues that have been activated. The likelihood of a residue's participation in photochemistry is influenced by its location relative to the surface of the protein tertiary structure and by whether it is feasibly oriented relative to the target [134,135]. The mechanisms implicated in crosslinking reactions of proteins in the presence of photosensitizers include the Type I and Type II mechanisms described above, as well as pathways in which the photosensitizer extracts a hydrogen atom from an amino acid residue, allowing the residue to participate directly in crosslinking [106].

The two proteins used in this dissertation research, bovine serum albumin (BSA) and acid-hydrolyzed type-I porcine gelatin ("gelatin") are both readily photocrosslinked. In fact, BSA can act as its own photosensitizer, although reaction efficiency is improved if an exogenous photosensitizer is added to the system. BSA is a compact globular protein of 66.5 kDa, shaped as a prolate obloid of dimensions 140 × 40 × 40 Å [136]. Of its 583 amino acid residues, 101 (16.6%) are the residues involved in photocrosslinking listed above [137]. Over a third of the residues are hydrophobic, but the protein is water soluble as the hydrophobic residues are tucked within the core of the globule, with hydrophilic residues on the surface. The isoelectric point in water at 25°C is 4.7, so in neutral buffers, BSA bears a net negative charge [138].

Gelatin is derived from the denaturation and partial hydrolysis of collagen, which is the most abundant structural protein in animals. There are several related proteins in the collagen family, but the most relevant to this work is type-I collagen, which structurally consists of three polypeptides twisted into left-handed helices, coiled into a triple-helix. The helices are arranged in parallel to form long fibrils [139]. The polypeptides are nearly identical in structure and consist of repeating motifs of glycine-proline-X or glycine-X-hydroxyproline, where X is another amino acid residue [140]. The small glycine residue facilitates the tight packing of fibrils, while the proline and hydroxyproline stabilize the triple helix.

Although, collagen itself is not water soluble, various gelatin variants are highly soluble. Gelatins are industrially derived by extracting collagen from the skin, bones, and hooves of livestock and hydrolyzing it under acidic (Type A gelatin) or alkaline (Type B gelatin) conditions. The process unravels the individual collagen polypeptide strands and breaks them down into fragments which vary in size. The distribution of fragment sizes depends on the temperature, pH, and time of the process as well as the source of the collagen. Type A gelatin, of most interest to us, has an isoelectric point of 7.5-9.2, so in neutral buffers it is mildly cationic.

Gelatin is used in the food industry for its ability to thermally set into a hydrogel at room temperature. Indeed, the word “gel” derives from this well-known property of gelatin [141]. Above its melting point, gelatin polypeptides dissociate and disperse through the aqueous media. As the temperature decreases, the polypeptide molecules reassemble into triple helices with other polypeptides in a process called renaturation. Each polypeptide coils with multiple others, forming physical crosslinks that transform the solution into a solid network [140]. The more crosslinks in a network, the stiffer the gel will be. Since longer polypeptides form more crosslinks than shorter ones, the extent of hydrolysis of the original collagen determines how stiff the gel can be. For this reason, commercially available gelatin is often rated by its Bloom number, a measure of the strength of gelatin gelled according to a defined protocol [142]. The Bloom number reflects the average molecular weight of the polypeptides.

Since gelatin is irregularly fragmented collagen, it isn’t possible to know how many photocrosslinkable residues each polypeptide bears. However an analysis of the amino acid composition reveals that histidine, lysine, tryptophan and tyrosine comprise 3.7% of bovine type I collagen polypeptides [143]. This is much lower than in BSA.

Photocrosslinked gelatin gels tend to be softer than photocrosslinked BSA gels, and the low availability of photocrosslinkable residues is probably a major reason.

Since photocrosslinking of these proteins takes place in a small voxel, the laser beam that initiates the reaction must be scanned in a manner that ensures the voxels overlap. The overlap ensures that each new line or layer of printed material is connected with previously printed material. To achieve overlap, the step-size between printed lines and layers must be smaller than the width of the voxel. The lateral and axial dimensions of the voxel are determined by a number of factors. The numerical aperture (NA) of the focusing objective influences the size and shape of the voxel by redistributing the light energy. A higher NA corresponds to a lower diffraction limit and narrower point spread function, and produces a more compact voxel [144]. The voxel size also depends on the light intensity threshold required to initiate photocrosslinking, which further depends on the two-photon cross-section of the photosensitizer, the efficiency of reaction initiation, and the dwell-time of the laser beam. The number of involved parameters makes it difficult to determine the voxel length and width using theoretical calculations [117]. Thus experimental means were used to determine step sizes for the laser scans to produce solid structures produced with voxels that overlapped substantially.

This dissertation describes the micro-3D printing of structures that serve as cellular microenvironments. The reagents used for micro-3D printing are aqueous solutions of the proteins BSA and gelatin, with rose bengal or eosin yellow added as photosensitizers. Specific reagent compositions will be discussed in later chapters.

1.6 PROTECTING CELLS FROM PHOTOCHEMICAL EFFECTS

The reactive products such as singlet oxygen and free radicals that are generated by photoreactions are necessary to induce crosslinking, but they can also be damaging to cells. If photoreactions are performed in close proximity to living cells, there may be injurious effects on the cells. Reactive molecules can modify the cell membrane, proteins, and nucleic acids with short- and long-term repercussions on the viability and behavior of cells [145]. Furthermore, micro-3D printing reagents such as some photosensitizers can have direct toxic effects on cells [146]. These effects can lead to necrosis in the short term, apoptosis over the course of hours, or other changes to cell behavior.

With the correct dosage, targeted delivery, and appropriate photoexcitation, phototoxic effects can be harnessed for therapeutic applications such as photodynamic therapy. But when maintaining cell health is the goal, there are strategies for minimizing phototoxicity when performing micro-3D printing. One is a careful selection of reagents to ensure biocompatibility. Proteins such as BSA and gelatin are of biological origin and non-toxic at the selected concentrations. Some photosensitizers, such as flavin adenine dinucleotide, are biological molecules and cells display a tolerance for them at concentrations (on the order of 10 mM) that would be toxic if a synthetic photosensitizer such as rose bengal were used [107].

There are many biological antioxidants, such as ascorbate, α-tocopherol and lycopene, which quench or neutralize free radicals. Adding appropriate amounts of these antioxidants to the system can terminate reactive molecules before they have a chance to damage cells [147].

Photosensitizers can damage cells through in a number of ways. Firstly, the photosensitizer molecules may be endocytosed by cells, bringing them into closer proximity with intracellular organelles where photoexcitation can break down compounds or crosslink proteins [148]. Secondly, extracellular photosensitizers and reactive molecules in an excited state can diffuse toward cells and cause damage extracellularly.

Thirdly, photosensitizers in some cases may be toxic without light excitation. These problems can be avoided by conjugating the photosensitizer to larger molecules [149].

As reactive molecules diffuse toward cells, they undergo Brownian motion while colliding with solvent, reagent, and other molecules along the way. Each collision increases the likelihood that the reactive molecule will be neutralized before it reaches the cell, so by increasing the distance between the photoreaction site and cells, the likelihood of cell damage is reduced. A further option is to use bulk fluid flow to direct diffusing molecules away from a cell of interest. This possibility is explored in Chapter 2.

1.7 CONCLUSION AND CHAPTER SUMMARY

This chapter has been an introduction to the broad field of cell behavior in response to *in vitro* environments. In particular, it has explored the literature on cellular response to topographical influences, and discussed the applicability of multiphoton micro-3D printing to this field. The importance of studying cell behavior in dynamic environmental conditions has also been considered.

Chapter 2 describes a method to introduce topographical guidance cues to a culture of neuronal cells, with the aim of guiding neurites toward target sites. Micro-3D printing is performed proximally to living cells, while measures are taken to minimize cytotoxic effects. Results from these experiments are presented and further challenges are discussed. Chapter 3 introduces multiphoton imprinting, a technique that allows modulation of the surface topography of a micro-3D printed material. Several reaction parameters are explored and their effects on imprinting are characterized. Chapter 4 describes how topographical changes introduced onto a cell substrate by multiphoton imprinting influences the behavior of cells. Chapter 5 explores future directions into which this work may be extended.

1.8 REFERENCES

1. Loeb L. Über die Entstehung von Bindegewebe, Leucocyten und roten Blutkörperchen aus Epithel; und über eine Methode, isolierte Gewebsteile zu züchten [Internet]. Chicago, Stern; 1897 [cited 2013 Dec 23]. 72 p. Available from: http://archive.org/details/berdieentstehu00loeb

2. Harrison RG, Greenman MJ, Mall FP, Jackson CM. Observations of the living developing nerve fiber. Anat Rec. 1907;1(5):116–28.

3. Rous P, Jones FS. A Method for Obtaining Suspensions of Living Cells from the Fixed Tissues, and for the Plating Out of Individual Cells. J Exp Med. 1916 Apr 1;23(4):549–55.

4. Dulbecco R. Production of Plaques in Monolayer Tissue Cultures by Single Particles of an Animal Virus. Proc Natl Acad Sci U S A. 1952 Aug;38(8):747–52.

5. Sanford KK, Earle WR, Likely GD. The growth in vitro of single isolated tissue cells. J Natl Cancer Inst. 1948 Dec;9(3):229–46.

6. Puck TT, Marcus PI. A Rapid Method for Viable Cell Titration and Clone Production with HeLa Cells in Tissue Culture: The Use of X-Radiated Cells to Supply Conditioning Factors. Proc Natl Acad Sci U S A. 1955 Jul 15;41(7):432–7.

7. Eagle H. The Specific Amino Acid Requirements of a Mammalian Cell (strain L) in Tissue Culture. J Biol Chem. 1955 Jun 1;214(2):839–52.

8. Sanford KK, Westfall BB, Fioramonti MC, McQuilken WT, Bryant JC, Peppers EV, et al. The effect of serum fractions on the proliferation of strain L mouse cells in vitro. J Natl Cancer Inst. 1955 Dec;16(3):789–802.

9. Freshney RI. Culture of Animal Cells: A Manual of Basic Technique and Specialized Applications. 6th edition. Hoboken, N.J: Wiley-Blackwell; 2010.

10. Van der Valk J, Brunner D, De Smet K, Fex Svenningsen A, Honegger P, Knudsen LE, et al. Optimization of chemically defined cell culture media--replacing fetal bovine serum in mammalian in vitro methods. Toxicol In Vitro. 2010 Jun;24(4):1053–63.

11. Ehrmann RL, Gey GO. The Growth of Cells on a Transparent Gel of Reconstituted Rat-Tail Collagen. J Natl Cancer Inst. 1956 Jun 1;16(6):1375–403.

12. Lydon MJ, Minett TW, Tighe BJ. Cellular interactions with synthetic polymer surfaces in culture. Biomaterials. 1985 Nov;6(6):396–402.

13. Hoch HC, Jelinski LW, Craighead HG. Nanofabrication and Biosystems: Integrating Materials Science, Engineering, and Biology. Cambridge ; New York, NY, USA: Cambridge University Press; 1996.

14. Hoppe TJ, Moorjani SG, Shear JB. Generating Arbitrary Chemical Patterns for Multipoint Dosing of Single Cells. Anal Chem. 2013 Apr 2;85(7):3746–51.

15. Moorjani S, Nielson R, Chang XA, Shear JB. Dynamic remodeling of subcellular chemical gradients using a multi-directional flow device. Lab Chip. 2010 Aug 21;10(16):2139–46.

16. McCaig CD, Song B, Rajnicek AM. Electrical dimensions in cell science. J Cell Sci. 2009 Dec 1;122(23):4267–76.

17. Kornreich BG. The patch clamp technique: principles and technical considerations. J Vet Cardiol. 2007 May;9(1):25–37.

18. Nguyen HT, Sapp S, Wei C, Chow JK, Nguyen A, Coursen J, et al. Electric field stimulation through a biodegradable polypyrrole-co-polycaprolactone substrate enhances neural cell growth. J Biomed Mater Res A. 2014 Aug;102(8):2554–64.

19. Borgens RB. Electrically mediated regeneration and guidance of adult mammalian spinal axons into polymeric channels. Neuroscience. 1999;91(1):251–64.

20. Guo A, Song B, Reid B, Gu Y, Forrester JV, Jahoda CAB, et al. Effects of Physiological Electric Fields on Migration of Human Dermal Fibroblasts. J Invest Dermatol. 2010 Sep;130(9):2320–7.

21. Carter SB. Principles of Cell Motility: The Direction of Cell Movement and Cancer Invasion. Nature. 1965 Dec 18;208(5016):1183–7.

22. Albrecht-Buehler G. The angular distribution of directional changes of guided 3T3 cells. J Cell Biol. 1979 Jan;80(1):53–60.

23. Cooper A, Munden HR, Brown GL. The growth of mouse neuroblastoma cells in controlled orientations on thin films of silicon monoxide. Exp Cell Res. 1976 Dec;103(2):435–9.

24. Furshpan EJ, MacLeish PR, O'Lague PH, Potter DD. Chemical transmission between rat sympathetic neurons and cardiac myocytes developing in microcultures: evidence for cholinergic, adrenergic, and dual-function neurons. Proc Natl Acad Sci U S A. 1976 Nov;73(11):4225–9.

25. Ivanova OY, Margolis LB. The Use of Phospholipid Film for Shaping Cell Cultures. Nature. 1973 Mar 16;242(5394):200–1.

26. Kleinfeld D, Kahler KH, Hockberger PE. Controlled outgrowth of dissociated neurons on patterned substrates. J Neurosci. 1988 Nov;8(11):4098–120.

27. Hammarback J a., Palm S l., Furcht L t., Letourneau P c. Guidance of neurite outgrowth by pathways of substratum-adsorbed laminin. J Neurosci Res. 1985;13(1-2):213–20.

28. Blawas AS, Reichert WM. Protein patterning. Biomaterials. 1998 May;19(7-9):595–609.

29. Théry M. Micropatterning as a tool to decipher cell morphogenesis and functions. J Cell Sci. 2010 Dec 15;123(Pt 24):4201–13.

30. Folch A, Toner M. Microengineering of cellular interactions. Annu Rev Biomed Eng. 2000;2:227–56.

31. Seidlits SK, Schmidt CE, Shear JB. High-Resolution Patterning of Hydrogels in Three Dimensions using Direct-Write Photofabrication for Cell Guidance. Adv Funct Mater. 2009 Nov 23;19(22):3543–51.

32. Petersen OW, R?nnov-Jessen L, Howlett AR, Bissell MJ. Interaction with basement membrane serves to rapidly distinguish growth and differentiation pattern of normal and malignant human breast epithelial cells. Proc Natl Acad Sci U S A. 1992 Oct 1;89(19):9064–8.

33. Hoffman RM. To do tissue culture in two or three dimensions? That is the question. Stem Cells. 1993 Mar;11(2):105–11.

34. Yang J, Richards J, Bowman P, Guzman R, Enami J, McCormick K, et al. Sustained growth and three-dimensional organization of primary mammary tumor epithelial cells embedded in collagen gels. Proc Natl Acad Sci USA. 1979 Jul;76(7):3401–5.

35. Ma W, Fitzgerald W, Liu Q-Y, O'Shaughnessy TJ, Maric D, Lin HJ, et al. CNS stem and progenitor cell differentiation into functional neuronal circuits in three-dimensional collagen gels. Exp Neurol. 2004 Dec;190(2):276–88.

36. Seidlits SK, Drinnan CT, Petersen RR, Shear JB, Suggs LJ, Schmidt CE. Fibronectin-hyaluronic acid composite hydrogels for three-dimensional endothelial cell culture. Acta Biomater. 2011 Jun;7(6):2401–9.

37. Kloxin AM, Kloxin CJ, Bowman CN, Anseth KS. Mechanical Properties of Cellularly Responsive Hydrogels and Their Experimental Determination. Adv Mater. 2010;22(31):3484–94.

38. Tibbitt MW, Anseth KS. Dynamic Microenvironments: The Fourth Dimension. Sci Transl Med. 2012 Nov 14;4(160):160ps24–160ps24.

39. Okano T, Yamada N, Okuhara M, Sakai H, Sakurai Y. Mechanism of cell detachment from temperature-modulated, hydrophilic-hydrophobic polymer surfaces. Biomaterials. 1995 Mar;16(4):297–303.

40. Ebara M, Uto K, Idota N, Hoffman JM, Aoyagi T. Shape-Memory Surface with Dynamically Tunable Nano-Geometry Activated by Body Heat. Adv Mater. 2012 Jan 10;24(2):273–8.

41. Le DM, Kulangara K, Adler AF, Leong KW, Ashby VS. Dynamic topographical control of mesenchymal stem cells by culture on responsive poly(ε-caprolactone) surfaces. Adv Mater. 2011 Aug 2;23(29):3278–83.

42. Davis KA, Burke KA, Mather PT, Henderson JH. Dynamic cell behavior on shape memory polymer substrates. Biomaterials. 2011 Mar;32(9):2285–93.

43. Edahiro J-I, Sumaru K, Tada Y, Ohi K, Takagi T, Kameda M, et al. In situ control of cell adhesion using photoresponsive culture surface. Biomacromolecules. 2005 Apr;6(2):970–4.

44. Yeo W-S, Yousaf MN, Mrksich M. Dynamic interfaces between cells and surfaces: electroactive substrates that sequentially release and attach cells. J Am Chem Soc. 2003 Dec 10;125(49):14994–5.

45. Van Dongen SFM, Maiuri P, Marie E, Tribet C, Piel M. Triggering Cell Adhesion, Migration or Shape Change with a Dynamic Surface Coating. Adv Mater. 2013;25(12):1687–91.

46. Davila J, Chassepot A, Longo J, Boulmedais F, Reisch A, Frisch B, et al. Cyto-mechanoresponsive Polyelectrolyte Multilayer Films. J Am Chem Soc. 2012 Jan 11;134(1):83–6.

47. Weiss P. Erzwingung elementarer Strukturverschiedenheiten am in vitro wachsenden Gewebe. Wilhelm Roux' Archiv für Entwicklungsmechanik der Organismen. 1929 Jun 27;116(1):438–554.

48. Weiss P. Cellular Dynamics. Rev Mod Phys. 1959 Jan;31(1):11–20.

49. Weiss P. Guiding principles in cell locomotion and cell aggregation. Exp Cell Res. 1961;8:260–81.

50. Petrie RJ, Doyle AD, Yamada KM. Random versus directionally persistent cell migration. Nat Rev Mol Cell Biol. 2009 Aug;10(8):538–49.

51. Abercrombie M. The bases of the locomotory behaviour of fibroblasts. Exp Cell Res. 1961;8, Supplement:188–98.

52. Galle J, Preziosi L, Tosin A. Contact inhibition of growth described using a multiphase model and an individual cell based model. Appl Math Lett. 2009 Oct;22(10):1483–90.

53. Bettinger CJ, Langer R, Borenstein JT. Engineering substrate topography at the micro- and nanoscale to control cell function. Angew Chem Int Ed Engl. 2009;48(30):5406–15.

54. Ambrose EJ. The movements of fibrocytes. Exp Cell Res. 1961;8, Supplement:54–73.

55. Ingram VM. A Side View of Moving Fibroblasts. Nature. 1969 May 17;222(5194):641–4.

56. Carter SB. Haptotaxis and the Mechanism of Cell Motility. Nature. 1967 Jan 21;213(5073):256–60.

57. Abercrombie M, Heaysman JEM, Pegrum SM. The locomotion of fibroblasts in culture: I. Movements of the leading edge. Exp Cell Res. 1970 Mar;59(3):393–8.

58. Abercrombie M, Heaysman JEM, Pegrum SM. The locomotion of fibroblasts in culture: III. Movements of particles on the dorsal surface of the leading lamella. Exp Cell Res. 1970 Oct;62(2–3):389–98.

59. Abercrombie M, Heaysman JE, Pegrum SM. The locomotion of fibroblasts in culture. IV. Electron microscopy of the leading lamella. Exp Cell Res. 1971 Aug;67(2):359–67.

60. Abercrombie M, Heaysman JEM, Pegrum SM. Locomotion of fibroblasts in culture: V. Surface marking with concanavalin A. Exp Cell Res. 1972 Aug;73(2):536–9.

61. Milestone 2 : Nature Milestones in Cytoskeleton [Internet]. [cited 2013 Dec 28]. Available from: http://www.nature.com/milestones/milecyto/full/milecyto02.html

62. MBInfo contributors. Types of cell-matrix adhesion complexes [Internet]. MBInfo Wiki; 2011 [cited 2014 Jun 18]. Available from: http://www.mechanobio.info/figure/1384243207520.jpg.html

63. Lazarides E, Weber K. Actin Antibody: The Specific Visualization of Actin Filaments in Non-Muscle Cells. Proc Natl Acad Sci USA. 1974 Jun 1;71(6):2268–72.

64. Ridley A, Peckham M, Clark P. Cell Motility: From Molecules to Organisms. 1 edition. Wiley; 2007. 364 p.

65. Bellairs R, Curtis A, Dunn G. Cell Behaviour: A Tribute to Michael Abercrombie. Cambridge ; New York: Cambridge University Press; 1982. 624 p.

66. Dunn GA, Heath JP. A new hypothesis of contact guidance in tissue cells. Exp Cell Res. 1976 Aug;101(1):1–14.

67. Lackie JM, Dunn GA, Jones GE. Cell Behaviour: Control and Mechanism of Motility. London: Portland Press; 346 p.

68. Ohara PT, Buck RC. Contact guidance in vitro: A light, transmission, and scanning electron microscopic study. Exp Cell Res. 1979 Jul;121(2):235–49.

69. Geiger B, Spatz JP, Bershadsky AD. Environmental sensing through focal adhesions. Nat Rev Mol Cell Biol. 2009 Jan;10(1):21–33.

70. Wedlich D. Cell Migration in Development and Disease. 1st edition. Weinheim: Wiley-Blackwell; 2005. 398 p.

71. Gauthier NC, Masters TA, Sheetz MP. Mechanical feedback between membrane tension and dynamics. Trends in Cell Biology. 2012 Oct;22(10):527–35.

72. Lauffenburger DA, Horwitz AF. Cell Migration: A Physically Integrated Molecular Process. Cell. 1996 Feb 9;84(3):359–69.

73. Bettinger CJ, Orrick B, Misra A, Langer R, Borenstein JT. Microfabrication of poly (glycerol-sebacate) for contact guidance applications. Biomaterials. 2006 Apr;27(12):2558–65.

74. Curtis A, Wilkinson C. Topographical control of cells. Biomaterials. 1997 Dec;18(24):1573–83.

75. Danuser G, Allard J, Mogilner A. Mathematical modeling of eukaryotic cell migration: insights beyond experiments. Annu Rev Cell Dev Biol. 2013;29:501–28.

76. Rangarajan R, Zaman MH. Modeling cell migration in 3D. Cell Adh Migr. 2008;2(2):106–9.

77. Fraley SI, Feng Y, Krishnamurthy R, Kim D-H, Celedon A, Longmore GD, et al. A distinctive role for focal adhesion proteins in three-dimensional cell motility. Nat Cell Biol. 2010 Jun;12(6):598–604.

78. Weiss P. Cell contact. Int Rev Cytol. 1958;(7):391–423.

79. Curtis ASG, Varde M. Control of Cell Behavior: Topological Factors. JNCI J Natl Cancer Inst. 1964 Jul 1;33(1):15–26.

80. Rovensky YA, Slavnaja IL, Vasiliev JM. Behaviour of fibroblast-like cells on grooved surfaces. Exp Cell Res. 1971 Mar;65(1):193–201.

81. Brunette DM. Fibroblasts on micromachined substrata orient hierarchically to grooves of different dimensions. Exp Cell Res. 1986 May;164(1):11–26.

82. Brunette DM. Spreading and orientation of epithelial cells on grooved substrata. Exp Cell Res. 1986 Nov;167(1):203–17.

83. Clark P, Connolly P, Curtis AS, Dow JA, Wilkinson CD. Topographical control of cell behaviour: II. Multiple grooved substrata. Development. 1990 Apr;108(4):635–44.

84. Dunn GA, Brown AF. Alignment of fibroblasts on grooved surfaces described by a simple geometric transformation. J Cell Sci. 1986 Jul 1;83(1):313–40.

85. Oakley C, Brunette DM. The sequence of alignment of microtubules, focal contacts and actin filaments in fibroblasts spreading on smooth and grooved titanium substrata. J Cell Sci. 1993 Sep;106 (Pt 1):343–54.

86. Wójciak-Stothard B, Curtis A, Monaghan W, Macdonald K, Wilkinson C. Guidance and Activation of Murine Macrophages by Nanometric Scale Topography. Exp Cell Res. 1996 Mar 15;223(2):426–35.

87. MBInfo contributors. Growth cone structure [Internet]. MBInfo Wiki; 2012 [cited 2014 Jun 18]. Available from: http://www.mechanobio.info/figure/1384241700956.jpg.html

88. Maloney MT, Bamburg JR. Mechanisms of neuronal growth cone guidance: an historical perspective. Dev Neurobiol. 2011 Sep;71(9):795–800.

89. Blankenship AG, Feller MB. Mechanisms underlying spontaneous patterned activity in developing neural circuits. Nat Rev Neurosci. 2010 Jan;11(1):18–29.

90. Kandel E, Schwartz J, Jessell T. Principles of Neural Science. 4 edition. New York: McGraw-Hill Medical; 2000. 1414 p.

91. Offenhäusser A, Böcker-Meffert S, Decker T, Helpenstein R, Gasteier P, Groll J, et al. Microcontact printing of proteins for neuronal cell guidance. Soft Matter. 2007 Feb 14;3(3):290–8.

92. Wheeler BC, Brewer GJ. Designing Neural Networks in Culture. Proc IEEE Inst Electr Electron Eng. 2010 Mar 1;98(3):398–406.

93. Lohof AM, Quillan M, Dan Y, Poo MM. Asymmetric modulation of cytosolic cAMP activity induces growth cone turning. J Neurosci. 1992 Apr;12(4):1253–61.

94. Wang CJ, Li X, Lin B, Shim S, Ming G, Levchenko A. A microfluidics-based turning assay reveals complex growth cone responses to integrated gradients of substrate-bound ECM molecules and diffusible guidance cues. Lab Chip. 2008 Jan 29;8(2):227–37.

95. Hynd MR, Frampton JP, Dowell-Mesfin N, Turner JN, Shain W. Directed cell growth on protein-functionalized hydrogel surfaces. J Neurosci Methods. 2007 May 15;162(1-2):255–63.

96. Li J, McNally H, Shi R. Enhanced neurite alignment on micro-patterned poly-L-lactic acid films. J Biomed Mater Res A. 2008 Nov;87(2):392–404.

97. Krsko P, McCann TE, Thach T-T, Laabs TL, Geller HM, Libera MR. Length-scale mediated adhesion and directed growth of neural cells by surface-patterned poly(ethylene glycol) hydrogels. Biomaterials. 2009 Feb;30(5):721–9.

98. Houchin-Ray T, Huang A, West ER, Zelivyanskaya M, Shea LD. Spatially patterned gene expression for guided neurite extension. J Neurosci Res. 2009 Mar;87(4):844–56.

99. Craighead HG, James CD, Turner AMP. Chemical and topographical patterning for directed cell attachment. Curr Opin Solid State Mater Sci. 2001 Apr;5(2–3):177–84.

100. Wheeler BC, Corey JM, Brewer GJ, Branch DW. Microcontact printing for precise control of nerve cell growth in culture. J Biomech Eng. 1999 Feb;121(1):73–8.

101. Li GN, Liu J, Hoffman-Kim D. Multi-molecular gradients of permissive and inhibitory cues direct neurite outgrowth. Ann Biomed Eng. 2008 Jun;36(6):889–904.

102. Rajnicek A, Britland S, McCaig C. Contact guidance of CNS neurites on grooved quartz: influence of groove dimensions, neuronal age and cell type. J Cell Sci. 1997 Dec;110 (Pt 23):2905–13.

103. Mahoney MJ, Chen RR, Tan J, Saltzman WM. The influence of microchannels on neurite growth and architecture. Biomaterials. 2005 Mar;26(7):771–8.

104. Gomez N, Lu Y, Chen S, Schmidt CE. Immobilized nerve growth factor and microtopography have distinct effects on polarization versus axon elongation in hippocampal cells in culture. Biomaterials. 2007 Jan;28(2):271–84.

105. Jiang FX, Yurke B, Firestein BL, Langrana NA. Neurite outgrowth on a DNA crosslinked hydrogel with tunable stiffnesses. Ann Biomed Eng. 2008 Sep;36(9):1565–79.

106. Pitts JD, Campagnola PJ, Epling GA, Goodman SL. Submicron Multiphoton Free-Form Fabrication of Proteins and Polymers: Studies of Reaction Efficiencies and Applications in Sustained Release. Macromolecules. 2000 Feb 5;33(5):1514–23.

107. Kaehr B, Allen R, Javier DJ, Currie J, Shear JB. Guiding neuronal development with in situ microfabrication. Proc Natl Acad Sci USA. 2004 Nov 16;101(46):16104–8.

108. Stephanie Nemir HNH. PEGDA hydrogels with patterned elasticity: Novel tools for the study of cell response to substrate rigidity. Biotechnol Bioeng. 2009;105(3):636–44.

109. Pelham RJ, Wang Y -l. Cell locomotion and focal adhesions are regulated by substrate flexibility. Proc Natl Acad Sci USA. 1997 Dec 9;94(25):13661–5.

110. Vogel V, Sheetz M. Local force and geometry sensing regulate cell functions. Nat Rev Mol Cell Biol. 2006 Apr;7(4):265–75.

111. Kim B-S, Nikolovski J, Bonadio J, Mooney DJ. Cyclic mechanical strain regulates the development of engineered smooth muscle tissue. Nat Biotech. 1999 Oct;17(10):979–83.

112. Waters CM, Ridge KM, Sunio G, Venetsanou K, Sznajder JI. Mechanical stretching of alveolar epithelial cells increases Na(+)-K(+)-ATPase activity. J Appl Physiol. 1999 Aug;87(2):715–21.

113. Cheng C-M, Lin Y-W, Bellin RM, Steward RL Jr, Cheng Y-R, LeDuc PR, et al. Probing localized neural mechanotransduction through surface-modified elastomeric matrices and electrophysiology. Nat Protoc. 2010 Apr;5(4):714–24.

114. Han L-H, Lai JH, Yu S, Yang F. Dynamic tissue engineering scaffolds with stimuli-responsive macroporosity formation. Biomaterials. 2013 Jun;34(17):4251–8.

115. Gurkan UA, Tasoglu S, Akkaynak D, Avci O, Unluisler S, Canikyan S, et al. Smart Interface Materials Integrated with Microfluidics for On-Demand Local Capture and Release of Cells. Adv Healthc Mater. 2012 Sep;1(5):661–8.

116. Tibbitt MW, Kloxin AM, Dyamenahalli KU, Anseth KS. Controlled two-photon photodegradation of PEG hydrogels to study and manipulate subcellular interactions on soft materials. Soft Matter. 2010;6(20):5100–8.

117. Serbin J, Egbert A, Ostendorf A, Chichkov BN, Houbertz R, Domann G, et al. Femtosecond laser-induced two-photon polymerization of inorganic organic hybrid materials for applications in photonics. Opt Lett. 2003 Mar 1;28(5):301–3.

118. Kaehr B, Shear JB. Mask-Directed Multiphoton Lithography. J Am Chem Soc. 2007 Jan 30;129(7):1904–5.

119. Maruo S, Nakamura O, Kawata S. Three-dimensional microfabrication with two-photon-absorbed photopolymerization. Opt Lett. 1997 Jan 15;22(2):132–4.

120. Basu S, Campagnola PJ. Properties of crosslinked protein matrices for tissue engineering applications synthesized by multiphoton excitation. J Biomed Mater Res A. 2004 Nov 1;71(2):359–68.

121. Allen R, Nielson R, Wise DD, Shear JB. Catalytic Three-Dimensional Protein Architectures. Anal Chem. 2005 Jul 15;77(16):5089–95.

122. Kaehr B, Shear JB. Multiphoton fabrication of chemically responsive protein hydrogels for microactuation. Proc Natl Acad Sci USA. 2008 Jul 1;105(26):8850–4.

123. Nielson R, Kaehr B, Shear JB. Microreplication and Design of Biological Architectures Using Dynamic-Mask Multiphoton Lithography. Small. 2009 Jan 1;5(1):120–5.

124. Göppert-Mayer M. Über Elementarakte mit zwei Quantensprüngen. Ann Phys. 1931 Jan 1;401(3):273–94.

125. Kaiser W, Garrett C. Two-Photon Excitation in CaF_{2}: Eu^{2+}. Phys Rev Lett. 1961 Sep;7(6):229–31.

126. Denk W, Strickler JH, Webb WW. Two-photon laser scanning fluorescence microscopy. Science. 1990 Apr 6;248(4951):73–6.

127. LaFratta CN, Fourkas JT, Baldacchini T, Farrer RA. Multiphoton Fabrication. Angew Chem Int Ed. 2007 Aug 20;46(33):6238–58.

128. Levy JG. Photosensitizers in photodynamic therapy. Semin Oncol. 1994 Dec;21(6 Suppl 15):4–10.

129. Ravve A. Light-Associated Reactions of Synthetic Polymers. Springer Science & Business Media; 2007. 377 p.

130. Dolmans DEJGJ, Fukumura D, Jain RK. Photodynamic therapy for cancer. Nat Rev Cancer. 2003 May;3(5):380–7.

131. Testori A, Faries MB, Thompson JF, Pennacchioli E, Deroose JP, van Geel AN, et al. Local and intralesional therapy of in-transit melanoma metastases. J Surg Oncol. 2011 Sep;104(4):391–6.

132. Postnikova BJ, Currie J, Doyle T, Hanes RE, Anslyn EV, Shear JB, et al. Towards nanoscale three-dimensional fabrication using two-photon initiated polymerization and near-field excitation. Microelectron Eng. 2003 Sep;69(2–4):459–65.

133. Lyon JL, Hill RT, Shear JB, Stevenson KJ. Direct Electrochemical and Spectroscopic Assessment of Heme Integrity in Multiphoton Photo-Cross-Linked Cytochrome c Structures. Anal Chem. 2007 Feb 9;79(6):2303–11.

134. Shen HR, Spikes JD, Kopeceková P, Kopecek J. Photodynamic crosslinking of proteins. I. Model studies using histidine- and lysine-containing N-(2-hydroxypropyl)methacrylamide copolymers. J Photochem Photobiol B, Biol. 1996 Jul;34(2-3):203–10.

135. Spikes JD, Shen HR, Kopecková P, Kopecek J. Photodynamic crosslinking of proteins. III. Kinetics of the FMN- and rose bengal-sensitized photooxidation and intermolecular crosslinking of model tyrosine-containing N-(2-hydroxypropyl)methacrylamide copolymers. Photochem Photobiol. 1999 Aug;70(2):130–7.

136. Wright AK, Thompson MR. Hydrodynamic structure of bovine serum albumin determined by transient electric birefringence. Biophys J. 1975 Feb;15(2 Pt 1):137–41.

137. Stein WH, Stein WH. Amino Acif Composition of β-Lactoglobulin and Bovine Serum Albumin. J Biol Chem. 1949 Mar 1;178(1):79–91.

138. Ge S, Kojio K, Takahara A, Kajiyama T. Bovine serum albumin adsorption onto immobilized organotrichlorosilane surface: influence of the phase separation on protein adsorption patterns. J Biomater Sci Polym Ed. 1998;9(2):131–50.

139. Alberto M, Gabriela M. Hydrodynamic Properties of Gelatin - Studies from Intrinsic Viscosity Measurements. In: Verbeek C, editor. Products and Applications of Biopolymers [Internet]. InTech; 2012 [cited 2014 May 25]. Available from: http://www.intechopen.com/books/products-and-applications-of-

biopolymers/hydrodynamic-properties-of-gelatin-studies-from-intrinsic-viscosity-measurements

140. Izmailova VN, Derkach SR, Sakvarelidze MA, Levachev SM, Voron'kov NG, Yampol'skaya GP. Gelation in gelatin and gelatin-containing multicomponent blends. Polym Sci Ser C. 2004;46(12):73–92.

141. Kasapis S, Norton IT, Ubbink JB. Modern Biopolymer Science: Bridging the Divide between Fundamental Treatise and Industrial Application. Academic Press; 2009. 639 p.

142. Phillips GO, Williams PA. Handbook of Hydrocolloids. Taylor & Francis; 2000. 476 p.

143. Szpak P. Fish bone chemistry and ultrastructure: implications for taphonomy and stable isotope analysis. J Archaeol Sci. 2011 Dec;38(12):3358–72.

144. Sun H-B, Maeda M, Takada K, Chon JWM, Gu M, Kawata S. Experimental investigation of single voxels for laser nanofabrication via two-photon photopolymerization. Applied Physics Letters. 2003 Aug 4;83(5):819–21.

145. Lavie G, Kaplinsky C, Toren A, Aizman I, Meruelo D, Mazur Y, et al. A photodynamic pathway to apoptosis and necrosis induced by dimethyl tetrahydroxyhelianthrone and hypericin in leukaemic cells: possible relevance to photodynamic therapy. Br J Cancer. 1999 Feb;79(3-4):423–32.

146. Mousavi SH, Tavakkol-Afshari J, Brook A, Jafari-Anarkooli I. Direct toxicity of Rose Bengal in MCF-7 cell line: Role of apoptosis. Food Chem Toxicol. 2009 Apr;47(4):855–9.

147. Fritz Böhm RE. Antioxidant inhibition of porphyrin-induced cellular phototoxicity. J Photochem Photobiol B, Biol. 2002;177–83.

148. Rosenkranz AA, Jans DA, Sobolev AS. Targeted intracellular delivery of photosensitizers to enhance photodynamic efficiency. Immunol Cell Biol. 2000 Aug;78(4):452–64.

149. Hoppe TJ. Laser-Based Techniques for Manipulating the Single-Cell Environment [Doctoral]. [Austin, TX]: The University of Texas at Austin; 2013.

Chapter 2: Micro-3D printing under laminar flow and in the presence of cells

2.1 INTRODUCTION

Neuronal cells produce long, narrow, and often branching structures called neurites that, under the right circumstances, can participate in cell-cell communication. Researchers are interested in controlling the extension and directional growth of neurites for better control over cellular communication. Technologies that enable this would facilitate a number of applications, including nerve regeneration, and the development of neuronal networks and neuroelectronic interfaces. They could be used for analyte sensing, neurostimulation, and the development of *in vitro* biological computers [1,2].

A distal tip of an extending neurite contains a specialized structure called a growth cone. The growth cone has lamellipodia and filipodia that probe the environment around the cell through membrane receptors present on their surface that can sense chemical and physical cues in the environment. These environmental signals are processed within the growth cone, and trigger second-messenger signaling pathways that lead to cytoskeletal changes ultimately that influence the direction of neurite extension.

My work on printing *in situ* topographical guidance cues in a cell culture was initially motivated by my interest in neurite guidance. My goal was to direct the growth of neurites to specific target sites on other cell bodies and neurites. I planned to select neurites within a culture of neuronal cells, and then print walls to guide the extending neurites toward arbitrarily chosen target sites. Laminar flow would be used to direct phototoxic molecules generated by printing away from cells. A secondary goal was to measure the strength of any synapses that formed between the neurites and their targets.

The goal of micro-3D printing walls in the presence of living cells was based on preliminary results previously demonstrated in the Shear lab. Neurite guidance had been achieved in a culture of mouse neuroblastoma x rat glioma hybrid (NG108-15) cells and primary neurons by printing lines using multiphoton excitation, after temporarily replacing the cell culture media with a printing reagent [3]. This chapter seeks to extend these preliminary results into a validated method for *in situ* printing, and use it for targeted synaptogenesis.

2.2 METHODS

Formulation of printing reagent

The reagent solution contains bovine serum albumin (BSA) at a concentration shown in previous studies to produce robust micro-3D printed structures [3]. Flavin adenine dinucleotide (FAD) was selected as the photosensitizers because of its biocompatibility. The solution was buffered in HBS to maintain a near-neutral pH. The printing reagent solvent was based on a HEPES-buffered saline solution (HBS) consisting of 135 mM NaCl, 2 mM $MgCl_2$, 10 mM D-glucose, 5 mM KCl, 2 mM $CaCl_2$, and 10 mM HEPES adjusted to pH 7.4 (all obtained from Thermo Fisher Scientific, Waltham, MA. The photosensitizer FAD (F6625, Sigma, St Louis MO) was incorporated at concentrations of 1-5 mM, and dissolved using a rotating mixer overnight. Into this solvent, BSA (BAH64-0100, Equitech-Bio, Kerrville TX) was dissolved to a concentration of 300 mg/mL via centrifugation (which produces a more homogenous solution than vortexing). When the reagent was to be used in the presence of cells, it was first sterilized using a 0.22 μm PES syringe-driven filter unit (Millex-GP, Merck Millipore Ltd., Cork, Ireland).

Micro-3D printing directed by nanopositioner

Micro-3D printing was based on a method described previously [4]. A beam from a Q-switched frequency-doubled (532 nm) diode-pumped Nd:YAG laser (NG10320-110;

JDS Uniphase, San Jose, CA) was expanded to a diameter of 6 mm to overfill the back aperture of an objective (Nikon CFI S Plan Fluor ELWD 40X, 0.6 NA, Nikon Instruments, Melville, NY), mounted on an inverted microscope (TE-2000, Nikon Instruments, Melville, NY). The fabrication voxel was initially focused in the focal plane of the printing surface, which was a glass coverslip in contact with the reagent, to perform printing as depicted in Fig 2.1. In a closed vessel such as a flow chamber, top-down printing (from the "ceiling" of the vessel) allows each layer to be printed by a laser beam that has not been attenuated by passing through other printed layers. Alternatively, bottom-up printing (from the vessel "floor") may be performed when open vessels such as petri dishes are used. A piezo-nanopositioner (E-710, Physik Instrumente, Germany) translated the printing surface relative to the fabrication voxel, producing extended microstructures anchored to the printing surface. Translation along the xy-plane was used to print each layer of a microstructure. Individual lines of arbitrary length were printed separated by 0.5 μm lateral increments to produce a solid layer. Translation along the z-axis and printing more layers built up the microstructure in three dimensions. The layers were printed 0.5 μm apart to produce a solid wall. These step sizes were experimentally found to produce robust structures, indicating that the voxel for this set of parameters was over 0.5 μm wide at the beam waist and over 0.5 μm long in the axial direction

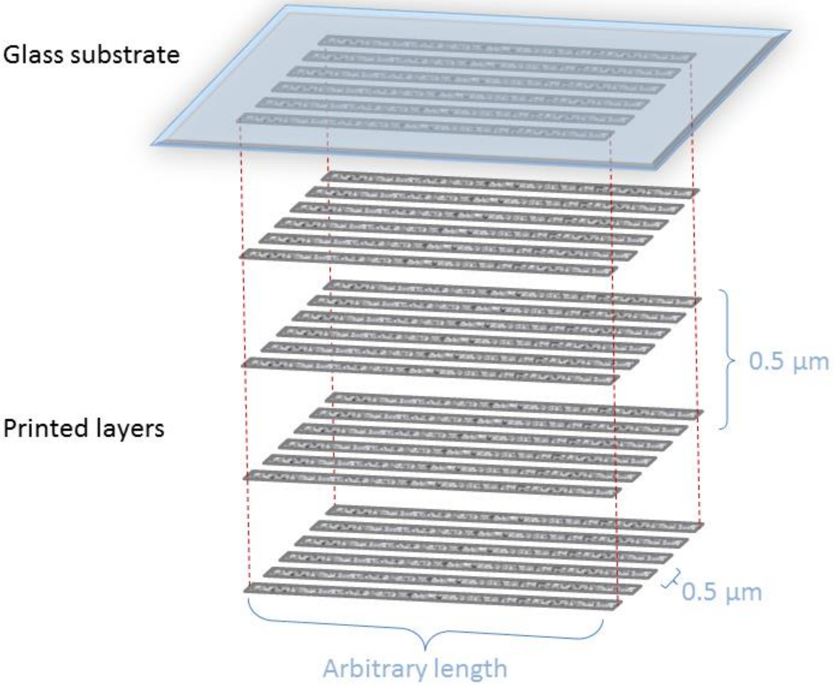

Figure 2.1: An exploded-view diagram showing the individual printed lines that comprise a micro-3D printed wall. The glass substrate anchoring the wall is at the top, and printing is performed starting from the lower surface of the glass in a top-down fashion. Individual lines are printed by stepping the voxel 0.5 µm laterally and vertically.

The highest peak power produced by this laser was ~7 kW and average power output was > 25 mW, with a pulse energy of ~3.5 µJ and pulse width ~600 ps. The repetition rate of the laser was ~7.65 kHz. As a result of attenuation from average laser powers at the (overfilled) back aperture of the objective were typically 7-12 mW.

Design of flow system

A flow cell (30 mm × 2.5 mm × 0.15 mm) consisting of a SecureSeal™ spacer and polycarbonate backing (#440889B, Grace BioLabs, Bend OR) was adhered to a printing surface consisting of a clean glass slide (Fisher Scientific, Hampton, NH) drilled with inlet holes. This created a flow chamber in which the glass formed the ceiling of the chamber. Printing reagent solution was circulated through the flow chamber using a syringe pump (53130, Stoetling Co., Wood Dale, IL) at flow rates ranging from 0.1 to 30 µL/min. C-flex tubing (1/32"ID x 3/32"OD, Cole-Parmer, Vernon Hills, IL) carried reagent from the 3 mL syringe (BD, Franklin Lakes, NJ) to the flow cell via silicone connectors (Grace BioLabs, Bend, OR). A schematic diagram of the flow system is depicted in Figure 2.2.

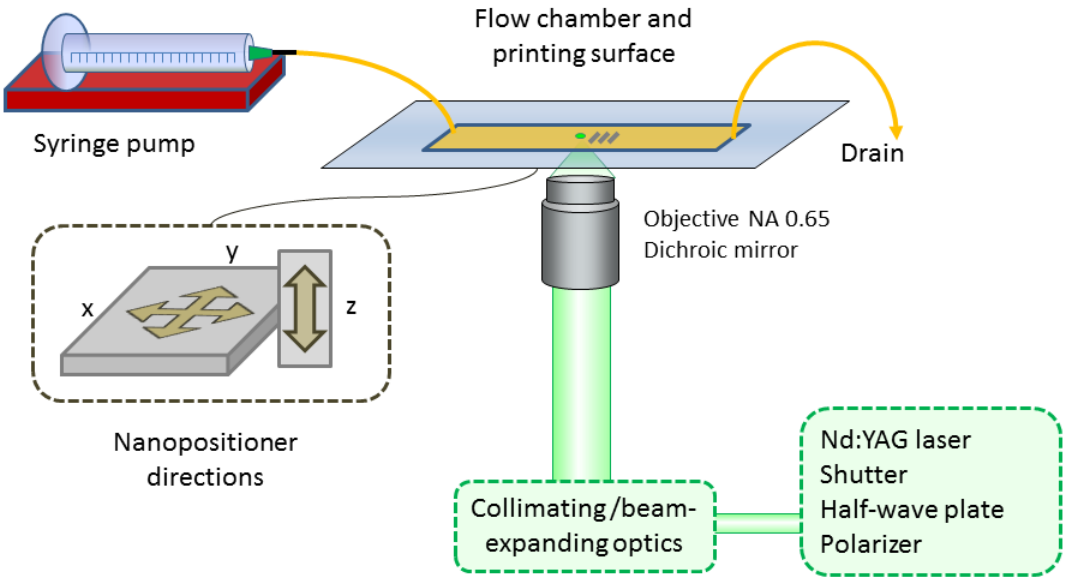

Figure 2.2: A schematic of the printing setup. A syringe pump delivers reagent solution into the flow chamber. An Nd:YAG laser beam is focused on the printing surface of the flow cell. A nanopositioner translates the flow cell relative to the focused laser beam.

Cell toxicity studies

A chambered coverslip with 8 wells (Nunc Lab-Tek II, Thermo Scientific, Waltham MA) was coated with poly-D-lysine hydrobromide (PDL) (MP Biomedicals, Santa Ana, CA). A 1 mg/mL PDL solution in water was added to each well and incubated at room temperature for 90 minutes. The wells were then rinsed thoroughly with sterile deionized water and air-dried in sterile conditions.

NG108-15 cells were seeded into each well at a calculated concentration of ~10,000 cells/cm^2. Each well had an area of 0.7 cm^2 and contained complete media, comprised of Dulbecco's Modification of Eagle's Medium (DMEM; Cellgro, Herndon, VA) with 10% fetal bovine serum (FBS; Hyclone, Logan, UT). The day after seeding (Day 1), the cells were imaged over an area of ~3 mm^2 in each well. On Day 2, 0.3 mL of media was removed from each well and replaced with 0.3 mL of reagent solution. Reagent solutions were prepared with the following concentrations of FAD: 0 mM, 6.66 mM, 10 mM, and 13.33 mM. When these solutions were added to the wells, the media already in the wells diluted the FAD to the following concentrations: 0 mM, 5 mM, 7.5 mM, and 10 mM.

Cells were kept in reagent solution for 1 hour at room temperature in a cell culture hood. This time-period was selected to match the expected length of one experiment. Then one-third of the reagent solution was removed from each well and replaced with the same volume of media gently to minimize detachment of cells. After waiting 10 minutes to allow the solutions to diffuse together, another 0.3 mL was removed and replaced by media. This step was repeated 2 times until the color of fluid in the wells appeared similar to the color of media without any added reagent. The gradual fluid exchange prevented the cells from being exposed to air and drying. The wells were then kept in an incubator overnight.

On Day 3, the cells were again imaged over an area of ~3 mm^2 in each well and the numbers of healthy and unhealthy cells were manually counted. Unhealthy cells were recognized by their granular (uneven boundaries and grainy cytoplasm) and/or vacuolar (containing one or more large vacuoles) morphologies. Morphological assessment was used in lieu of live/dead stains to assess viability because unhealthy cells had a tendency to detach from their substrate before they accepted dead-cell stains.

Printing in presence of cells

Chambered cover slips with 8 wells were coated with PDL by incubating in a 1 mg/mL PDL solution for 90 min. The wells were rinsed with sterile deionized water and dried. Wells were seeded with NG108-15 cells at a density of ~10,000 cells/cm^2 and maintained in differentiation media, consisting of DMEM with 1% FBS, in an incubator at 37°C with a humidified 5% CO_2 atmosphere. On Day 2 after seeding, the media was removed and replaced with reagent solution in thirds, as described in the cell toxicity section above. (FAD 5-7 mM, BSA 300 mg, HBS 1mL).

Using an Nd:YAG laser (532 nm) that was expanded to fill the back aperture of the 40X objective, several micro-walls were printed in the vicinity of the cultured cells.

The reagent solution was replaced with differentiation media and the culture returned to the incubator. The culture was returned to the microscope at intervals for brightfield imaging to monitor interactions of cultured cells with the fabricated micro-walls.

Scanning electron microscopy

Micro-3D printed structures were prepared for scanning electron microscopy by fixation for 20 minutes in a solution of 5% gluteraldehyde (Ted Pella, Redding, CA) in HBS, followed by serial dehydration in deionized water, 50% ethanol, 100% ethanol, a

50:50 ethanol-methanol solution, and 100% methanol. Specimens were finally air dried for one day, attached to a pin stub mount (Ted Pella, Redding, CA) with a PELCO carbon conductive tab (Ted Pella, Redding, CA) and silver paint and stored in a desiccator at room temperature for at least 2 days. Mounted specimens were sputter coated to a nominal thickness of 5 nm with platinum/palladium using a Cressington 208 Bench Top Sputter Coater (Cressington Scientific, Watford, UK).

Scanning electron microscopy (SEM) was performed using a Zeiss Supra 40 VP Field Emission Scanning Electron Microscope (Carl Zeiss Microscopy, Thordwood, NY). Mounted specimens were imaged using a secondary electron detector at an EHT voltage of 5.0-7.0 kV and working distance of 10-25 mm, with the specimen stage tilted at angles in the range 20°-60°. Heights of printed structures were calculated using trigonometry.

2.3 RESULTS AND DISCUSSION

The primary goal of the work presented in this chapter was to print protein-based microstructures through multiphoton photocrosslinking in an environment where one can control the residence time of photoreaction-generated molecules and thereby prevent damage to cells.

Multiphoton induced photocrosslinking reactions take place in close proximity to the laser focal point, and can produce reactive high-energy molecules such as singlet oxygen and photosensitizer fragment radicals [5,6]. As these reactive compounds diffuse from the focal region to surrounding areas, these species may damage cultured cells. The hypothesis I set out to evaluate was that convective flow that opposes the diffusion of cytotoxic molecules toward cells can serve as a means to protect cells from these species.

To this end, a platform was developed for printing protein microstructures within a flow chamber. The reagent solution provided the material for microstructure printing, and was flowed in a manner to convect reactive species away from cellular sites of interest. Such flow reduces the dwell time of reagent within the multiphoton laser voxel, reducing the efficiency of photoreaction for a given set of fabrication conditions. It was critical to carefully identify useful reaction parameters (e.g. average laser powers, concentrations of protein, concentrations of photosensitizer) to form the most robust structures possible (i.e. capable of forming robust barriers with defined geometries throughout experimental duration) while still minimizing the residence time of reactive molecules. A flow cell of 30 mm length × 2.5 mm width × 0.15 mm height was used for this application. A linear velocity flow map, shown in Figure 2.3, was calculated for a volumetric flow rate of 30 μL/min using the linear velocity (*v*) distribution equation, shown in Equation 2.1, for laminar flow through a rectangular channel [7].

$$v(y,z)=\frac{3Q}{2WH}\left(1-\frac{4y^2}{W^2}\right)\left(1-\frac{4z^2}{H^2}\right)$$

Equation 2.1

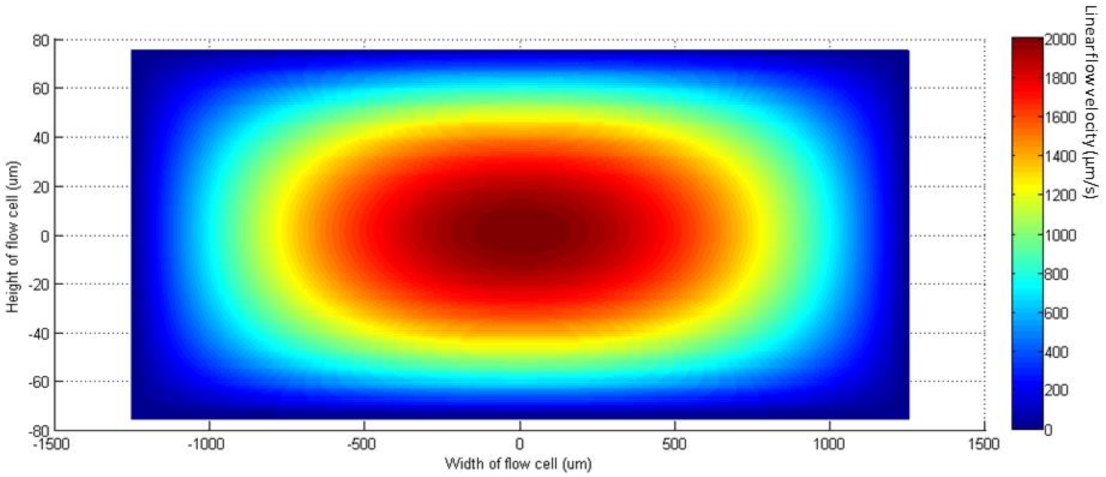

Figure 2.3: Linear flow velocity map generated by MATLAB using the velocity distribution equation for laminar flow through a rectangular channel. In the equation, y and z are the distances from the center of the channel in the horizontal and vertical directions respectively. Q is the volumetric flow rate and H and W are the height and width of the channel respectively. In this example, Q, W, and H are set to 30 µL/min, 2500 µm and 150 µm respectively.

The Q-switched Nd:YAG laser was previously demonstrated by the Shear lab to be a low-cost alternative to expensive mode-locked femtosecond lasers for printing protein-based microstructures [4]. A nanopositioner provided precise control in moving the sample stage relative to the stationary voxel, with a working space of 300 micrometers in three axes and a maximum travel speed of 200 µm/s. The stage movements were controlled with custom written LabView software that allowed printing of walls parallel to either the x- or y-axis.

I used NG108-15 cells as my model cell type for this application. NG108-15 cells readily proliferate in media supplemented with FBS. In conditions of reduced serum or elevated cyclic-adenosine monophosphate, they cease to proliferate and instead take on a neuronal phenotype, extending neurites and demonstrating electrical activity [8]. They are also capable of forming cholinergic synapses with myocytes [9]. Another option is to use primary neurons, but the Shear lab has previously observed greater sensitivity of primary cells to photosensitizer toxicity. NG108-15 cells have an advantage by being more resistant to harsh environmental conditions, and thus a better choice for preliminary studies. Primary neurons would be a natural next step for continued studies once toxicity in the system has been minimized.

Effect of flow rate on wall height

Under non-flow conditions, photoreaction-generated compounds diffuse from the reaction voxel uniformly in all directions. To prevent reactive compounds from reaching a site of interest at toxic concentrations, the linear velocity of fluid (v_f) opposing this diffusion can be set to be greater than the drift velocity (v_d) of reactive molecules toward the site. During diffusion, individual molecules undergo Brownian motion. Consequently, molecules move toward the cells in a distribution of drift velocities ($v_{d\ 1 \ldots n}$). Any v_f selected to oppose the diffusion can only prevent a fraction of the molecules from reaching the cell, with higher velocities opposing a larger fraction of molecules. Matching v_f to the mean v_d, is a reasonable first approximation.

Based on these conditions, a theoretical treatment allows the estimation of an appropriate v_f for the system. The average distance x traveled by the diffusing molecules in a time interval t is characterized by the root-mean-square of all displacements r undertaken by the molecules in one dimension in the same time. The mean-square displacement $<r^2>$ is related to t by Equation (2), where D is the diffusion coefficient [10].

$$<r^2> = 2Dt \tag{1}$$

The average drift velocity v_d of a molecule moving from the voxel to the site of interest is equal to the distance x from the voxel to the site, divided by the time t taken to cover that distance. It is expressed in terms of t in Equation (3) and in terms of $<r^2>$ in Equation (4).

$$v_d = \frac{x}{t} = \frac{\sqrt{<r^2>}}{t} = \frac{\sqrt{2Dt}}{t} = \sqrt{\frac{2D}{t}} \tag{2}$$

$$v_d = \frac{x}{t} = \frac{\sqrt{<r^2>}}{t} = \frac{\sqrt{<r^2>}}{\frac{<r^2>}{2D}} = \frac{2D}{\sqrt{<r^2>}} \tag{3}$$

The average drift velocity of a molecule is non-linearly related to the distance it must cover. As the molecule encounters more collisions along the longer path, it takes more time to cover each unit distance. Hence when the distance from the voxel to the site of interest is large, the average drift velocity is low and a lower flow velocity is needed to oppose the diffusion of the reactive molecule.

The diffusion coefficient, *D,* of reactive molecules in the solvent can be estimated as follows. The smallest reactive compounds generated by multiphoton excitation are singlet oxygen, peroxides and hydroxyl radicals, with molecular weights close to that of molecular oxygen. I approximated their diffusion coefficients with the diffusion coefficient of molecular oxygen, which is 2.1×10^{-5} cm^2/sec in water at 25°C [11]. However the reagent is an aqueous solution of BSA at a concentration of 300 mg/mL (at 37°C). The viscosity of this solution (measured by Ostwald viscometer) is ~7 cP, while the viscosity of water is 0.9 cP. The Stokes-Einstein equation relates the diffusion coefficient of a spherical particle in a fluid with the viscosity of the fluid, as seen in

Equation (5), where k_B is Boltzmann's constant, T is ambient temperature, η is the viscosity of a fluid, and R is the radius of a spherical particle diffusing through the fluid. [7].

$$D = \frac{k_B T}{6\pi \eta R} \tag{4}$$

If reactive molecules are treated as "spherical particles", the diffusion coefficient of a molecule through fluid is inversely proportional to the viscosity of the fluid. As the viscosity of reagent solution is about ten-fold greater than water, the diffusion coefficients of the reactive molecules will be approximately an order-of-magnitude smaller than the value given above. I therefore estimate the diffusion coefficient of reactive molecules through reagent solution is on the order of $\sim 10^{-6}$ cm^2/s, or ~ 100 μm^2/s.

Based on Equation (4) and this estimated diffusion coefficient, Table 2.1 summarizes the average drift velocity of a small reactive molecule diffusing across a range of distances in the reagent, and the fluid flow velocity needed to oppose the diffusion of at least half the molecules of that size.

Quantity	**Range of Values**		
Ave distance from voxel to site of interest $(x) = \sqrt{\langle r^2 \rangle}$	1 μm	10 μm	100 μm
Average drift velocity (v_d) = Required opposing flow velocity (v_f) $= 2D/\sqrt{\langle r^2 \rangle}$	200 μm/s	20 μm/s	2 μm/s

Table 2.1: Linear flow velocity required to oppose diffusion of small reactive molecules, for various distances x between voxel and site of interest. Diffusion coefficient D is assumed to be 100 μm^2/s.

The required volumetric flow rates are calculated as follows. To divert reactive molecules when printing a wall 1 µm from a site of interest, diffusion should to be opposed by a fluid with linear velocity (v_f) of 200 µm/sec. Given a flow chamber that is 0.15 mm tall and 2.5 mm wide, calculations presented in Figure 2.3 show that velocities up to 2000 µm/sec can be achieved in the center of the channel with a volumetric flow rate of 30 µL/min. Printing takes place within 10 µm of the glass surface and the linear velocity in this region is ~500 µm/sec, which is higher than the flow velocities needed to oppose diffusion. The system should be able to flush many reactive molecules away from cellular sites of interest, and experimental results can be used to determine if adjustments to the linear velocity are needed.

To demonstrate that structures can be printed in flowing reagent, I micro-3D printed walls of various heights in a flow chamber. Toward this end, a reagent with the protein composition described in the methods section and containing 7 mM FAD was circulated through the flow chamber at a range of volumetric flow rates. The average laser power at the objective back aperture was set to 9.3 mW. Walls were printed along the central axis of the flow chamber, and were spaced several tens of micrometers apart so non-linearity of flow caused by the presence of one wall would have a low impact on laminar flow around the next wall. Each wall was positioned with its length perpendicular to the flow direction, with a length of 100 µm and thickness 2.5 µm (6 lines, spaced 0.5 µm apart). The walls were printed to be 1, 3, and 5 layers tall, with each layer spaced by 0.5 µm along the vertical axis.

After the walls were printed, the samples were rinsed to remove reagent and prepared for SEM. Measured wall heights are presented in Figure 2.4. The SEM sample preparation process can shrink protein-based materials, and the measurements may understate the heights of the fully hydrated walls.

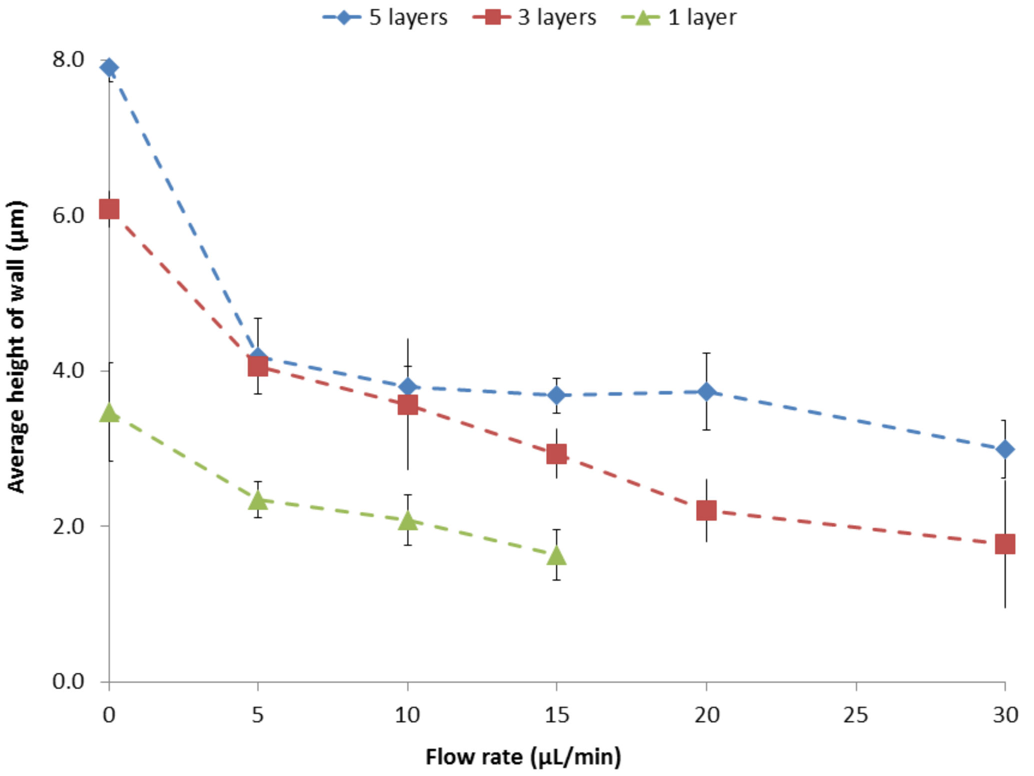

Figure 2.4: Plot showing the heights of walls produced when the volumetric flow rate was varied from 0-30 µL/min. Walls printed with 1 (▲), 3 (■), and 5(◆) layers are compared. n = 3, error bar indicates standard deviation.

A few features in the plot in Figure 2.4 are notable: (1) Under non-flow conditions, the walls printed with 1, 3, and 5 layers are 3.5 µm, 6 µm and 8 µm tall respectively; (2) As the reagent flow rate increases, the printed walls shorten in height; and (3) At flow rates higher than 10 µL/min, the 5-layer walls maintain a height of ~4 µm (with a slight decrease at the highest velocities).

The first feature is easily explained by the addition of material contributed by each printed layer. The second feature indicates that as the reagent spends less time within the reaction voxel, less material is printed and incorporated into the wall. The decrease in residence may also produce poorly crosslinked material that is easily detached from the walls. This is borne out by the observation that small fragments of newly printed material are seen breaking off the walls and flowing down the reagent stream during brightfield imaging. The third feature suggests that up to flow rates of 20 µL/min, there is a minimum height that 5-layer walls will reach. This may be because the linear velocity closer to the printing surface is slower and less disruptive to the printing process.

As estimated earlier, a volumetric flow rate of 30 µL/min would suffice to divert more than half of the reactive molecules away from cellular sites of interest. At such a flow rate, 4 µm tall walls can be built by printing 5 layers. SEM images of 5-layer walls, printed in non-flow and 30 µL/min flow conditions, are shown in Figures 2.5.

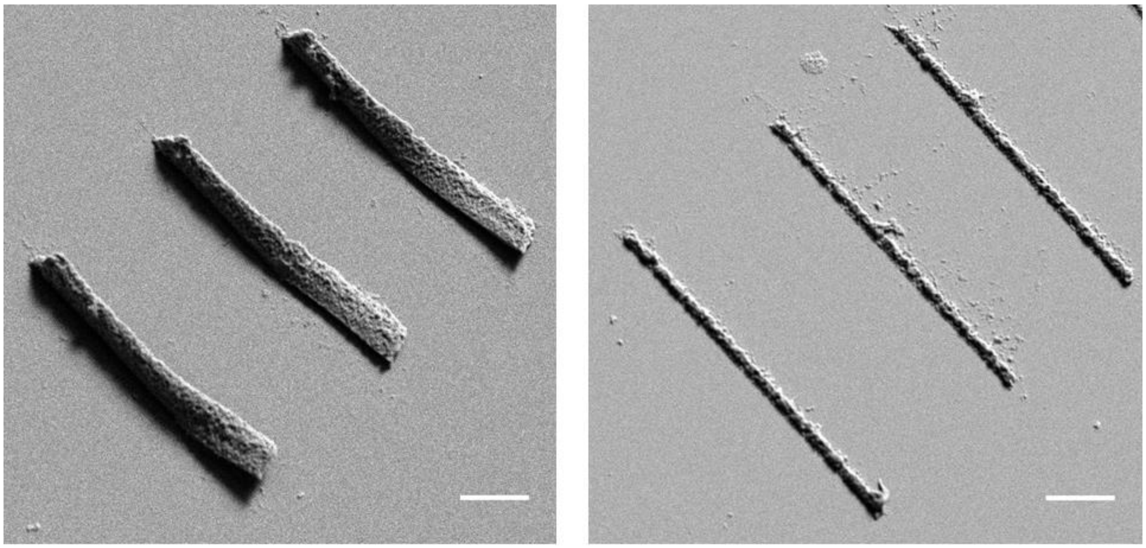

Figure 2.5: SEM images of walls. These were 5 layers tall, printed with reagent undergoing no flow (left) and 30 μL/min flow (right). Edges of walls detached from glass surface during sample preparation for SEM imaging. Scale bars = 20 μm

Effect of photosensitizer concentration on cell viability

The concentration of the photosensitizer in reagent affects the efficiency of the multiphoton photocrosslinking reaction induced by the Nd:YAG laser. Many proteins, including BSA, can be photocrosslinked without added photosensitizers, but the addition of photosensitizers increases crosslinking efficiency under the conditions used in these studies.

FAD is highly water-soluble and can dissolve in aqueous solutions at concentrations greater than 20 mM. It is fortuitously a photosensitizer with relatively low toxicity, serving as a good reagent for micro-3D printing in the vicinity of cells. To determine the concentration range of FAD which can be used with minimal cellular toxicity, a cytotoxicity assay was performed.

Initially, a conventional cell viability assay was attempted with C_{12}-resazurin and SYTOX Green (Molecular Probes, Eugene, OR) staining live and dead cells respectively. However, the NG108-15 cells were observed to detach from their substrates when in ill-health, even before apoptosis or necrosis occurred. This fact made the use of cell viability stains ineffectual in determining the fraction of cells that survive a given treatment. Instead, I performed a count of cells one day before and one day after exposure to reagent solution. Cells were classified as normal, vacuolar (containing visible vacuoles), and granular (a shriveled and grainy appearance) based on their morphology. The presence of vacuoles and granularity in NG108-15 cells is a sign of cell damage [12]. Figure 2.6 shows examples of normal, vacuolar and granular cells.

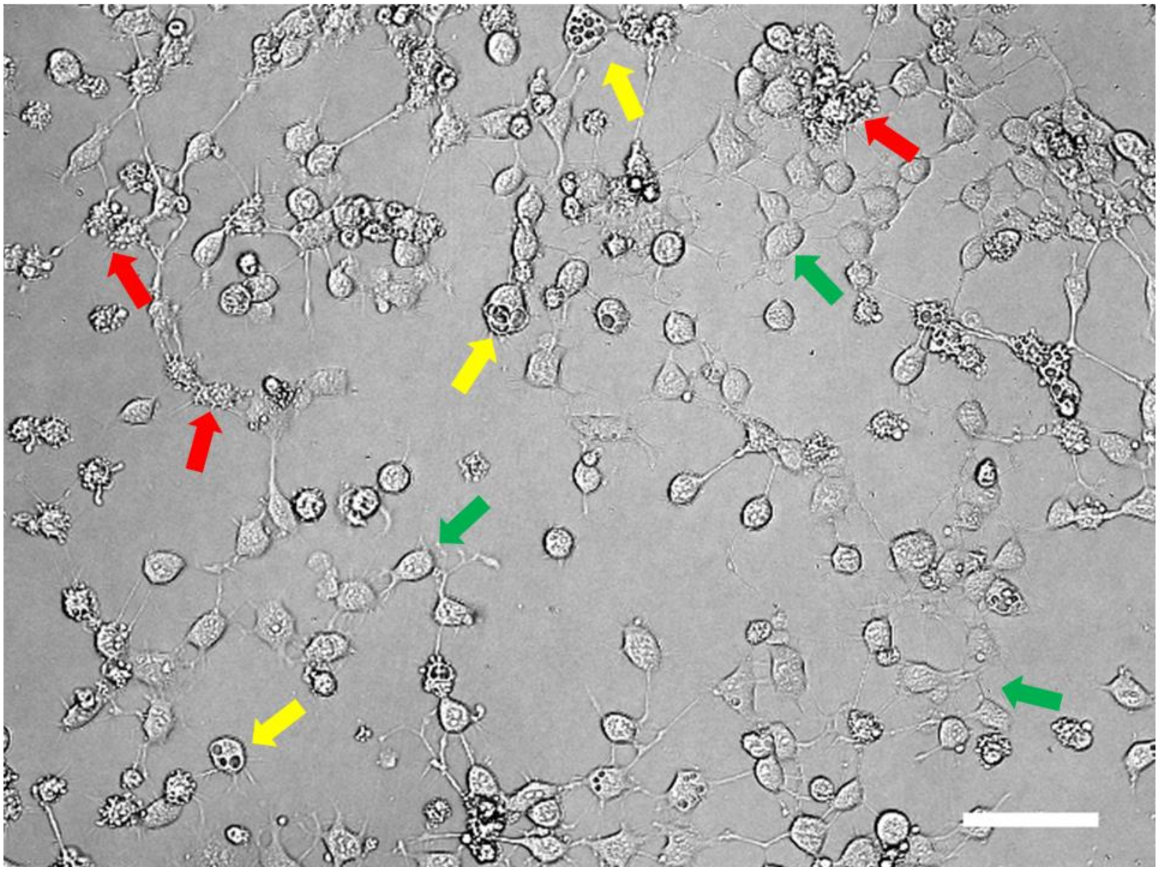

Figure 2.6: NG108-15 cells exposed to reagent solution containing 7.5 mM FAD for 1 hour. Normal morphology is indicated with green arrows (⬅), vacuolar morphology indicated with yellow arrows (⬅), and granular morphology indicated with red arrows(⬅). Scale bar, 100 µm.

The number of morphologically "normal" cells in each well, before (n_B) and after (n_A) exposure to reagent solution, were counted over an area of 3 mm^2 and the "fraction of normal cells remaining" (n_A/n_B) was calculated for each well. Since each FAD concentration was tested in duplicate, the average fraction was calculated for each concentration. Figure 2.7 shows the fraction of normal cells remaining after cells are exposed to reagent solutions containing difference concentrations of FAD.

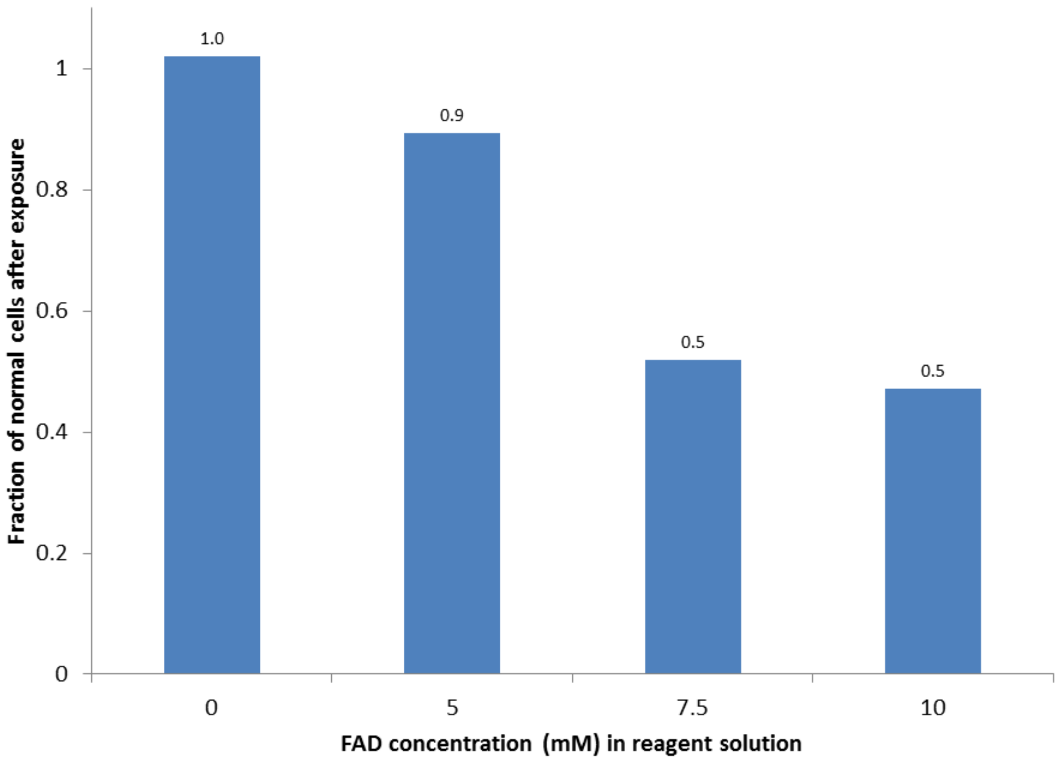

Figure 2.7: Plot showing the fraction of cells displaying normal morphology after exposure to different FAD concentrations. Cells were incubated in reagent solution for one hour at room temperature. 2 replicates for each concentration. Error bars indicate SD.

Based on these results, most cells exposed to 2.5 mM FAD remained healthy but concentrations greater than or equal to 7.5 mM resulted in cell damage in at least 50% of cells. The reagent solution must, therefore, be formulated with a concentration lower than this threshold.

Effect of photosensitizer concentration on printing

While high FAD concentrations are unfavorable for cell health, they increase reaction efficiency. With high photosensitizer levels, crosslinking density improves and printed structures maintain a robust shape. If the photoreaction occurs in a translating voxel, higher photosensitizer concentrations facilitate more reactions within a shorter laser dwell-time, so that structures can be printed relatively faster. All of these reasons favor the use of higher FAD concentrations.

To determine an optimum FAD concentration range that would minimize cytotoxicity while producing robust structures, a series of wall structures were micro-3D printed in a flow chamber with reagents containing 2 mM, 4 mM, and 7 mM FAD.

Lower FAD concentrations required higher peak intensities to initiate crosslinking, but the selection of laser power is constrained by two conditions. If the power is too low, the printing reaction will not initiate. If the power is too high, there will be cavitation explosions (explained in the next section). The range of usable powers varies with the FAD concentration in the reagent, so there is no one laser power that would print in all three FAD concentrations. In an attempt at consistency, I used the lowest power that appeared to initiate crosslinking at each FAD concentration. The average laser powers corresponding to these FAD concentrations (2 mM, 4 mM, and 7 mM) were set to 11 mW, 9.5 mW, and 6 mW at the objective back aperture respectively. Volumetric flow rates ranged from 0 to 30 μL/min and each wall was fabricated to be 5 layers tall. The resulting wall heights were determined using SEM. The plot in Figure 2.8 summarizes the findings.

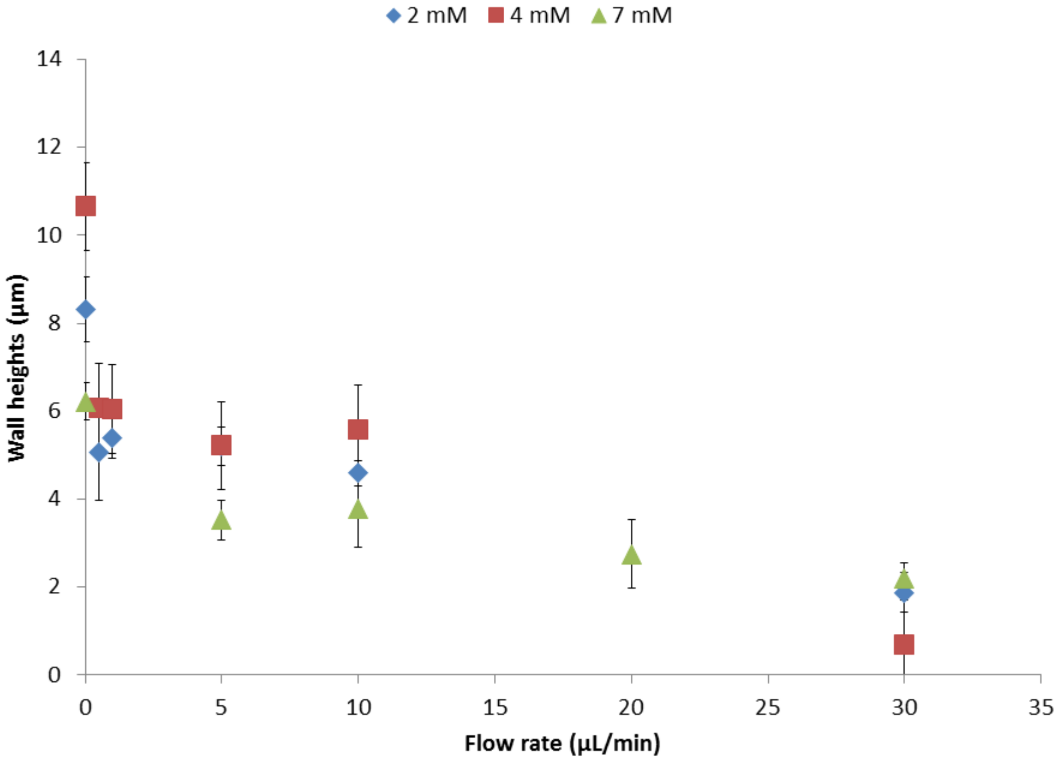

Figure 2.8: Plot showing the heights of walls produced when the volumetric flow rate varies from 0-30 µL/min. Walls printed with reagents containing 2 mM(◆), 4 mM (■), and 7 mM (▲) FAD are compared. n = 3, scale bar indicates SD.

The plot in figure 2.8 follows the general trend shown in Figure 2.4, in which the maximum heights of walls decrease with increasing flow rates. However, there is an unexpected feature. The walls produced by the 7mM reagent under non-flow conditions are unexpectedly low. This discrepancy can be explained by the difficulty of selecting an appropriate laser power for each FAD concentration. . While I used the lowest power that appeared to initiate crosslinking at each FAD concentration, the selection was based on visual assessment it is quite likely that the reaction efficiencies for each combination of laser power and FAD concentration were not comparable to each other, and that the 6mW and 7 mM FAD combination was inefficient at crosslinking compared to the other combinations.

These observations highlight the importance of laser power selection when printing. The next section explores the usable laser powers for reagents with different FAD concentrations.

Effect of laser power on printing

Although lower FAD concentrations make printing less efficient, this effect can be mitigated by increasing laser power so that the crosslinking density remains similar. However, as the laser power increases, there is a higher incidence of cavitation explosions. This is a phenomenon in which the laser energy causes localized overheating that produces a small pocket or cavity of vapor within the fluid [13]. When the cavity collapses, it triggers a shock wave that destroys printed structures and injures cells within several tens of microns of the explosion site. Avoiding these cavitation explosions is necessary for the integrity of printed structures and the well-being of cells.

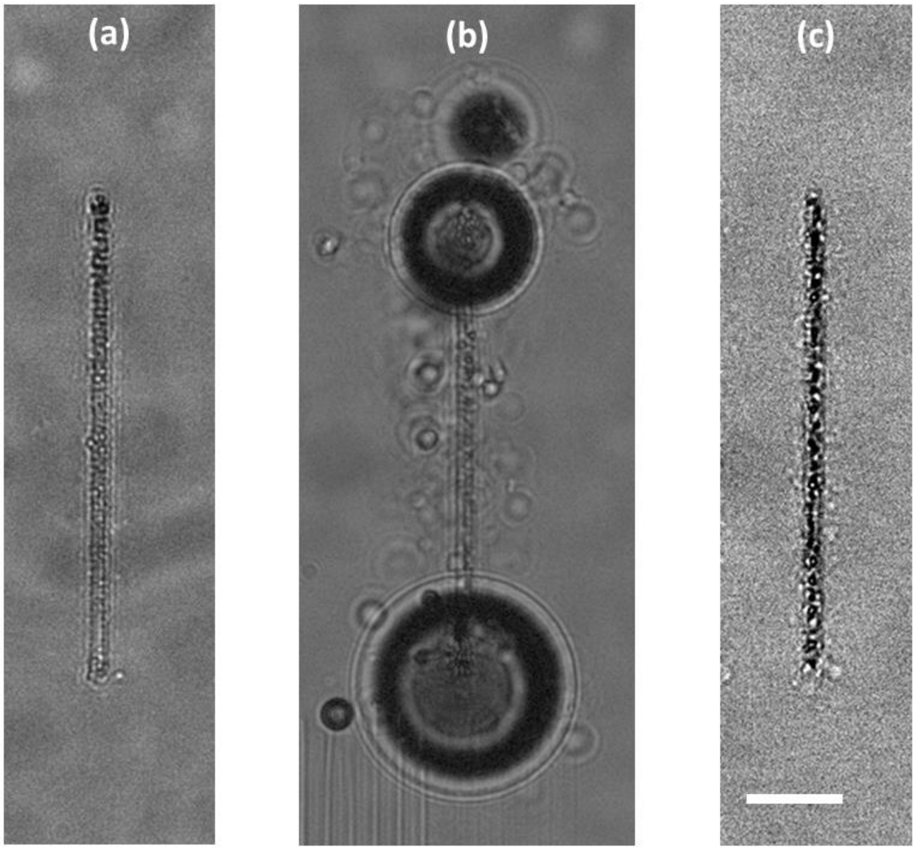

Figure 2.9: Brightfield microscope images of walls, 5 layers tall, printed under non-flow conditions. Wall on left (a) was printed with 3.5 mM FAD reagent with 7 mW laser power. Wall in center (b) was printed with 3.5 mM FAD reagent with 8 mW laser power. The circles are the sites of cavitation explosions. Wall on right (c) was printed with 7 mM FAD reagent with 5 mW laser power. All laser powers measured at objective back-aperture. Scale bar = 10 µm.

Figure 2.9 shows how different laser powers affect printing when two different reagent solutions are used. In (a) and (b), lines were printed using reagent containing 3.5 mM FAD. The power in (a) was 7 mW and produced poor walls. The power in (b) was 8 mW and produced cavitation explosions. The range of powers capable of producing robust lines without explosions was very narrow, and possibly non-existent. In contrast, the line in (c) was printed with reagent containing 7 mM FAD, at a power of 5 mW. The line was thick and substantial, and no explosions occurred during printing. These lines were all printed in no-flow conditions.

Figures 2.10 and 2.11 summarize the effects of printing with different powers and FAD concentrations.

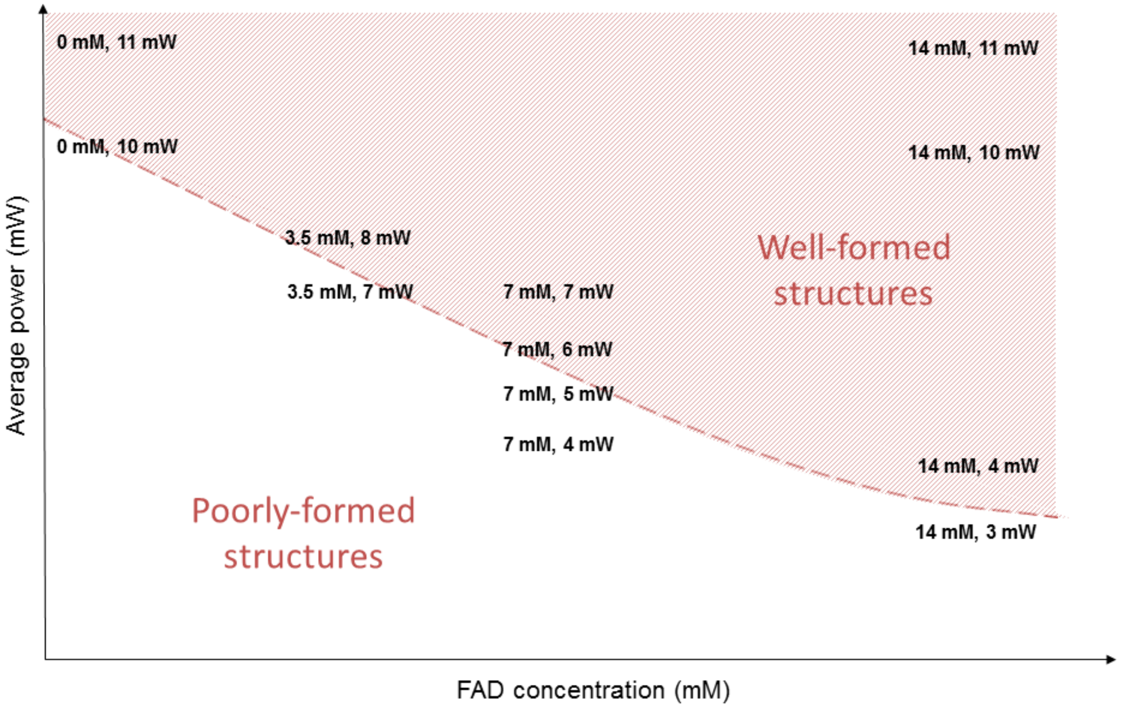

Figure 2.10: Parameter space showing combinations of average laser powers and FAD concentrations that produce well-formed structures (pink region) and poorly-formed structures (white region). Dashed boundary indicates that transition is gradual, not sharp.

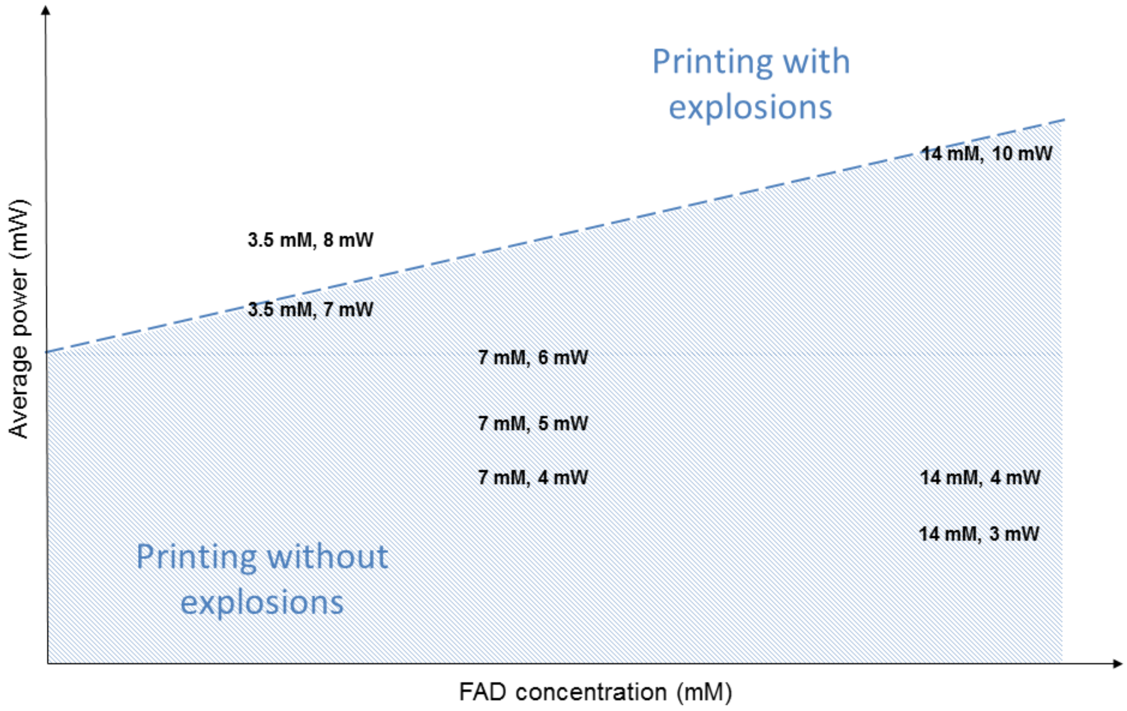

Figure 2.11: Parameter space showing combinations of average laser powers and FAD reagent concentrations that print without generating cavitation explosions (blue region) and with cavitation explosions (white region). Dashed boundary indicates that transition is gradual, not sharp.

Figure 2.10 shows that within the parameter space of average laser powers and FAD concentrations, there are combinations of powers and concentrations that produce well-formed structures with thick lines, and poorly-formed structures with thin lines. Higher FAD concentration reagents need lower levels of power to print well-formed structures. Figure 2.11 shows that within the same parameter space, there are combinations of powers and concentrations that avert the occurrence of explosions. At higher FAD concentrations, higher powers can be used without triggering explosions.

Summary of conditions

Cell toxicity effects placed a ceiling on usable FAD concentrations. On the other hand, the need to avoid cavitation explosions places a limit on maximum laser powers, and higher FAD concentrations are needed to produce robust structures at lower laser powers. The entire parameter space of FAD concentrations and average laser powers is summarized in Figure 2.12.

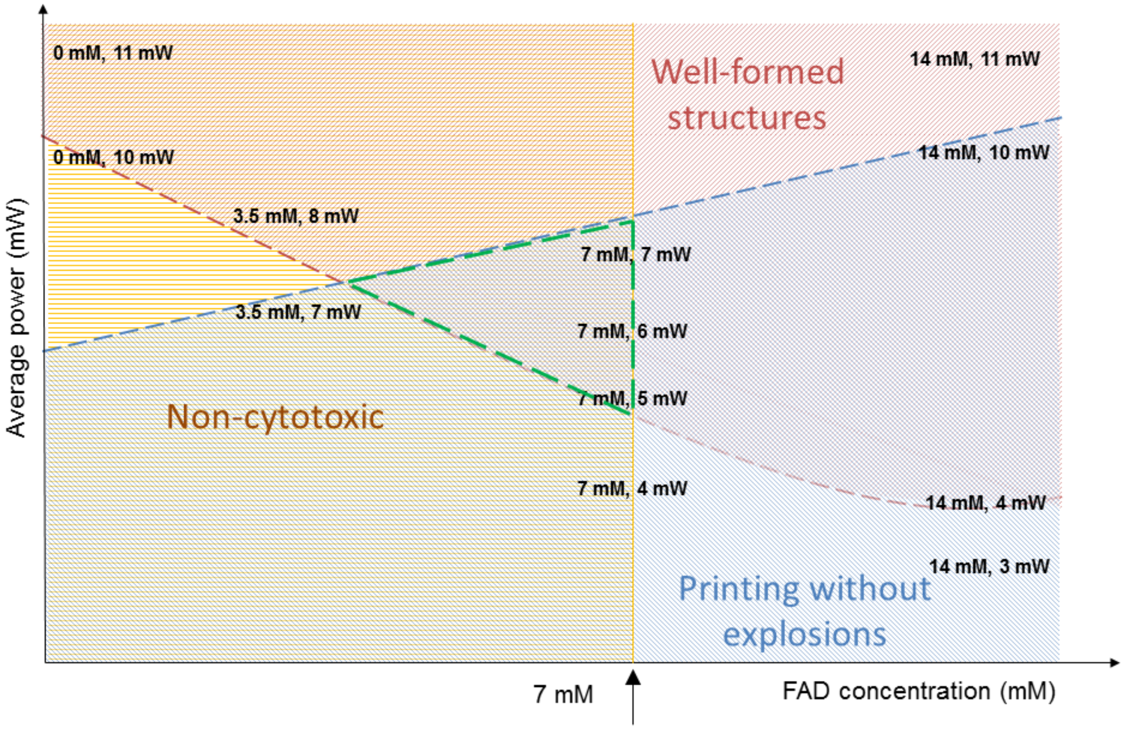

Figure 2.12: Parameter space showing combinations of average laser powers and FAD reagent concentrations that produce well-formed structures without cavitation explosions (purple region, where pink and blue regions overlap) in no-flow conditions. The graph also shows the region where FAD reagent concentrations have low cytotoxicity (yellow region). The optimum parameter space (outlined in green) contains power and concentration specification that may enable printing in the vicinity of cells. Dashed boundary indicates that transition is gradual, not sharp.

Within this parameter space, there was a small window in which FAD caused low-to-moderate toxicity, and enable printing of fairly robust structures in no-flow conditions without triggering cavitation explosions. This window limited the usable FAD concentrations to the 5-7 mM range. The optimal laser power for printing at these concentrations was 5-7 mW. These conditions were tested in the next section.

Effect of printing walls in vicinity of cells

While I was optimizing experimental conditions that would print robust walls while preserving cell health, I also attempted printing walls within cultures of NG108-15 cells. I began by fabricating walls in non-flow conditions. I cultured cells as described in the methods section, and then differentiated them with low serum media for two days to express a neuronal phenotype. Media was replaced with reagent solution for the 1-2 hours it took to print walls around cells. Then the reagent was replaced with media and the cells were returned to the incubator.

During the exchange of fluids, it was noticed that many cells detached from the culture surface and were subsequently washed away. Since many of the cells had formed cell-cell adhesions, a few detached cells would tug on other cells attached to the surface and pull them off as well, until entire sheets of cells were disrupted.

Several attempts were made to enhance the attachment of cells to the glass surface. In case cell damage was affecting cell adhesion, the cells' exposure time to FAD was limited. Illumination was restricted to red light to minimize photodamage. In case low serum levels were disrupting cell adhesion, cells were instead differentiated with cyclic-AMP in complete media [8]. These attempts did not appreciably improve cell adhesion.

One strategy that reduced disruption to cells after printing was to replace the reagent solution with media by one-third of its volume at a time. The cells were most fragile at the end of the printing sessions because they had been exposed to FAD, room temperature conditions, and photoreactive molecules. Rinsing the reagent vigorously produced turbulence that detached cells from the surface. By replacing the fluid in small increments, the reagent was diluted out without dramatically dropping the fluid level in the well, which minimized their disruption. After the cells were returned to the incubator in fresh media, they generally were observed to stabilize.

During the printing session, cells were examined carefully to identify distinct neurites that were extending toward an area clear of cells. Walls parallel to the x- or y-axis were printed with the goal of blocking the extending neurite and deflect its growth in another direction. After rinsing the reagent, the cells were kept in the incubator and monitored over the next few days.

In many cases, the neurites did not encounter the target walls. Although the neurites continued to grow, the cell bodies also moved relative to the printed walls. Consequently, the neurites grew in directions that did not lead them to encounter a wall, as shown in Figure 2.13. A wall was printed in the path of an extending neurite at a distance of ~40 μm, but two days later the neurite was growing in a direction that avoided the wall entirely. It is possible that the neurite encountered the wall at some point but move away before the image was taken. This highlights the importance of temperature-controlled imaging chambers that would enable live-cell imaging.

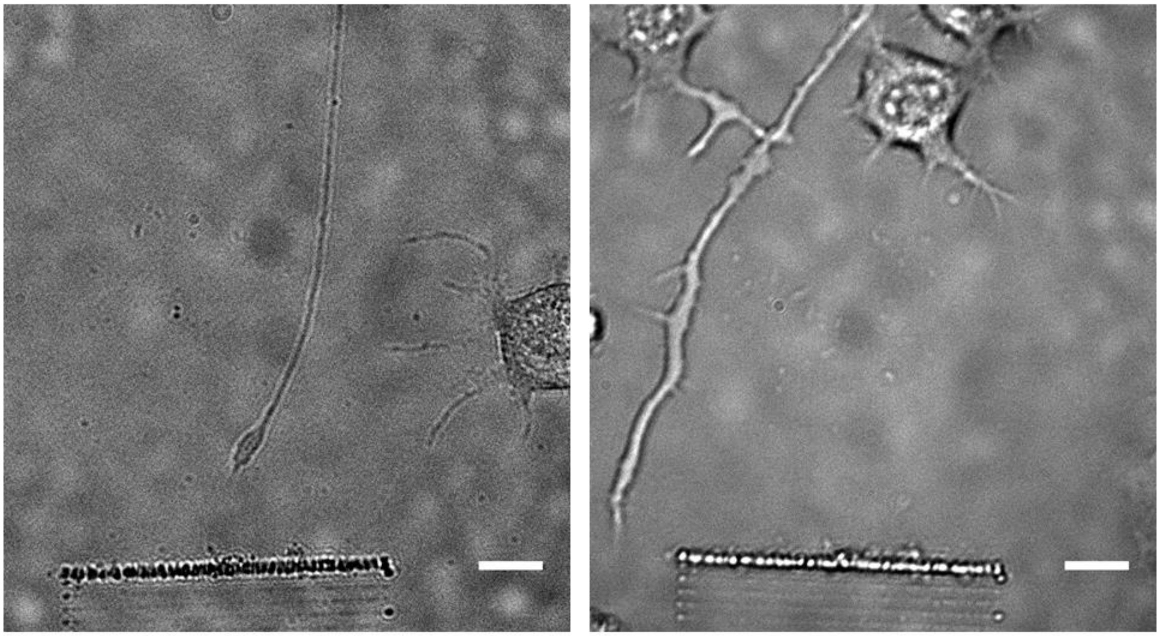

Figure 2.13: A 5-layer wall was printed in the path of an extending neuron. Two days later, the neurite had shifted and avoided the wall entirely. Scale bar 20 µm

NG108-15 are not classified as motile cells, but because of their relatively weak cell-surface adhesions and their stronger cell-cell adhesions they have a tendency to drift from their positions under environmental influences such as fluid flow or movement of adjacent cells. Several attempts were made (described above) to improve cell-surface adhesion but none were able to stop cell body drift. One technique did reduce cell drift somewhat. When I printed single lines (not walls) in the vicinity of cells of interest, cells were less likely to drift over them although they could still rotate in place and move neurites away from target walls. Figure 2.14 shows an example of this phenomenon.

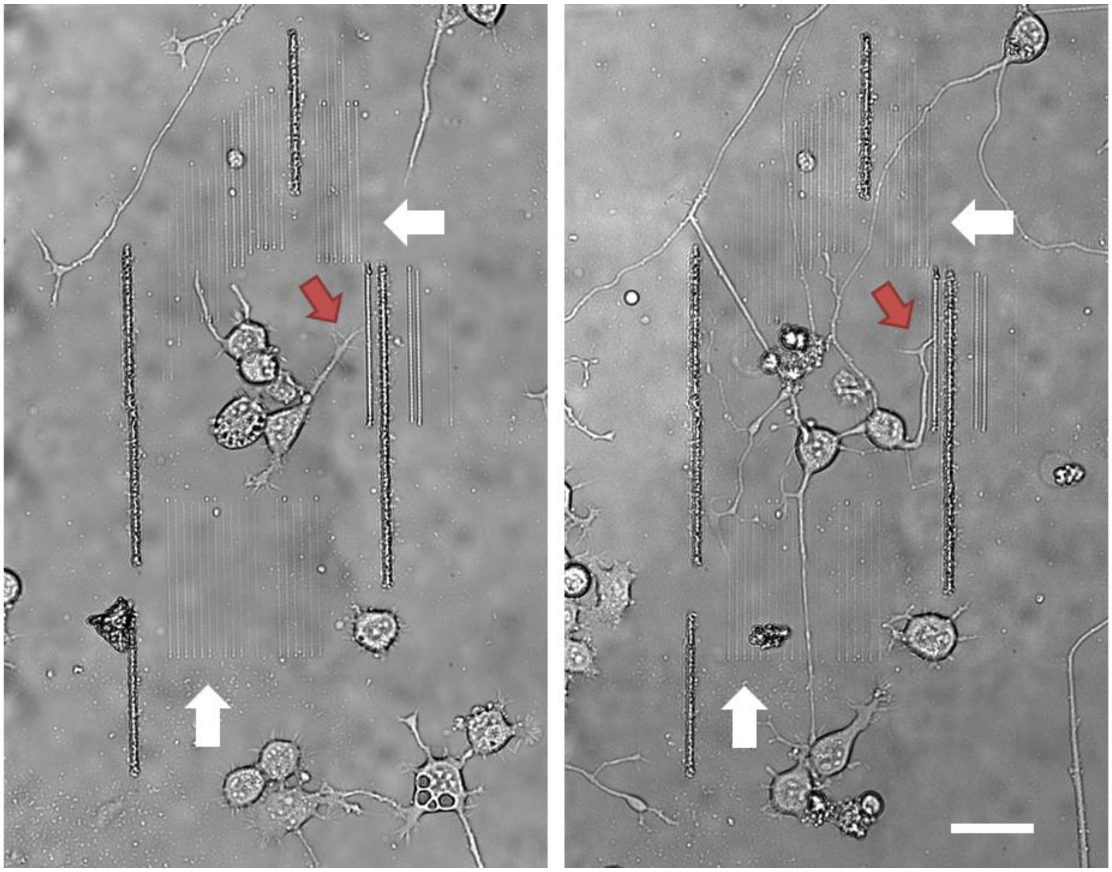

Figure 2.14: A cell extends a neurite (red arrow) that is blocked by a 5-layer wall (left panel). One day later, the neurite encountered and was deflected by the wall (right panel). Fine printed lines (white arrows) in the area around the cells may have kept the cells from drifting too far from their initial position. Scale bar 50 μm.

Although there were individual instances where a neurite encountered a wall and changed its direction of growth, these instances comprised a small fraction of all attempts to deflect neurites. It seemed even less likely for neurites to extend after deflection to contact a desired target cell, which was one of the primary goals of this project. In all, these results indicated that printed walls in this particular set-up will not readily be developed into a reproducible means to guide NG108-15 neurites.

2.4 CHALLENGES

A few changes to the experimental setup likely would have improved the outcome of these studies. Neuronal cells are distressed by changes in temperature and pH, and measures could be taken to stabilize these. Cells experienced large variations in temperature from 19°C on the microscope stage to 37°C in the incubator. A temperature-controlled environmental chamber on the microscope stage would have maintained the cells at a constant 37°C throughout a procedure. An environmental chamber would also permit time-lapse imaging of the cell culture, yielding more insights into movement of cells and interaction of neurites with walls. In addition, the cell culture media DMEM is a carbonate-based media which requires a 5% CO_2 concentration in air to maintain a neutral pH. Under atmospheric conditions, with a 0.04% CO_2 concentration, the media experiences a pH increase by 2 points over 24 hours. Using a non-carbonate-buffered media would help keep the cells at a neutral pH.

While these modifications would improve cell health and possibly enhance neurite stability, other conditions continued to pose a problem. Although fabrication was conducted in a parameter space that provided the best outcome in terms of cell health and fabrication, it was difficult to fabricate robust structures using FAD at concentrations that didn't cause moderately toxic effects in a measurable portion of cells. Fabrication under flow may lower phototoxic effects, but it would not affect non-photogenerated cytotoxicity from FAD. Furthermore, observations by other members of the Shear lab indicated that at high concentrations, BSA and other proteins may be toxic to cells. It would be far preferable to have an experimental system in which cells did not have to be incubated in potentially cytotoxic or phototoxic reagents.

Another challenge in these studies was the selection of an appropriate model cell line for this application. NG108-15 is a hardy cell line, but it has mostly been used in electrophysiology and neuronal function studies [14]. It has not been extensively validated as a model for neurite guidance studies and may not be suitable for topographical neurite guidance studies. This realization led to an examination of the literature for other cell types that may be better models for my application. PC12 cells have been used as model for neuron polarization and neurite guidance [15–17]. They can also form synapse-like structures with each other [15], but there is no evidence that these structures are capable of synaptic communication. In fact, to date there are no well-characterized cell lines capable of forming synapses with their own cell type. Studies in the literature on neurite guidance and synaptogenesis rely on hippocampal and cortical neurons from rodent brain tissue explants [18–20], but these cells are highly sensitive to environmental conditions, particularly the presence of photosensitizers.

At this point, I felt it was important to reflect on the project as a whole and consider whether topographical guidance of neurites for synaptogenesis is a viable goal. A revisit of the literature showed a number of reasons why the avenue of *in situ* printing of walls to guide neurites for synaptogenesis would be challenging.

In the literature, the majority of neurite guidance studies use chemical cues, both diffusible and immobilized, to direct the directional growth of neurites [21]. Diffusible cues, in particular, can be targeted to reflect the actual morphology and distribution of cells, which generally cannot be predicted *a priori*. Topographical neurite guidance has been demonstrated through surfaces with sub-micron features such as ridges, posts or pits [22], but these effects are relatively minor and can primarily be observed statistically on a large population of cells. There are relatively few studies that demonstrate small numbers of neurons being directed to connect with each other via topographical cues [23–25]. The disparity in the number of publications using chemical versus topographical cues to guide neurites may reflect a greater technological challenge in achieving the latter.

2.5 CONCLUSION

The work presented in this chapter details a number of interesting findings about micro-3D printing in cell culture. To print robust walls without incurring the risk of cavitation explosion, the photosensitizer concentration needs to be increased but at excessive concentrations it can be cytotoxic. Phototoxicity may be reduced by fabricating walls under laminar flow, but this will not remove cytotoxic effects. Additionally, there is a dearth of cell lines that would serve as a good model for the targeted neurite guidance studies that were a primary goal of this project. Because of these challenges, I decided to consider alternative experimental goals.

At its core, my interest is in researching the influence of topographical cues on cell behavior. While topographical neurite guidance may be difficult to achieve, there are other cellular responses to topography that may be more feasible to study. One of the most extensively studied cell behaviors is the alignment of certain cells, particularly fibroblasts, to topographical anisotropy. Fibroblasts undergo morphological changes when they grow on fibrous or grooved surfaces, taking on a long and narrow bipolar shape instead of the spread-out and stellate shape they generally adopt on flat surfaces. This behavior has been studied since the early 20th century and there is a considerable volume of literature that explores its nuances and mechanisms [26]. Additionally, there is an established mouse embryonic fibroblast cell line (NIH-3T3) that has been extensively characterized [27] and used as a model for topographical response studies [28,29], and might serve as a better model for a new method to study cellular responses to dynamic topographies.

In addition to selecting a new cell line for my studies, I also re-evaluated my micro-3D printing setup. As described earlier in this chapter, the setup consisted of a stationary laser beam focused on a printing surface that was translated in three dimensions with a nanopositioner-controlled stage. Although the nanopositioner could be programmed to move the stage through any path in three dimensions, each path had to be programmed individually, which could take hours to days depending on the path's complexity. This limits the versatility of this system for creating more complex topographies in future studies. The stage was also limited to a maximum linear velocity of 200 μm/s. The resolution of printed structures would be improved by increasing the linear velocity of the printed voxel, resulting in structures with more structural integrity.

Over the past few years, the Shear lab has developed another micro-3D printing configuration that uses scanning mirrors to translate the laser beam in a fast-moving raster pattern. Coupled with a dynamic mask, this setup prints structures more quickly and in a more versatile range of shapes than the nanopositioner-based setup [30,31]. As a result, I redesigned my printing setup to take advantage of these innovations. This redesign had a few experimental consequences. Because the scanning mirrors translated the laser beam at a maximum linear velocity of 68,000 μm/s, the system needed a laser with a higher repetition rate than the Q-switched Nd:YAG laser offered. A mode-locked, femtosecond pulsed titanium:sapphire laser was used in its place, which was tuned to a light output of wavelength 740 nm, compared with the 532 nm wavelength of the Nd:YAG laser. When using 740 nm light to excite FAD via two-photon absorption, this species is less effective as a photosensitizer, making it necessary to identify an alternate approach. Although these changes require the re-optimization of experimental parameters, the advantage of a faster and more versatile printing setup makes the tradeoff worthwhile.

The use of the new setup also enabled a new technique, called imprinting, which offered the advantage of altering the topographical environment of cells without incubating the cells in potentially cytotoxic or phototoxic reagents. As will be discussed in the next chapter, cells in an imprinting experiment are plated on a substrate which is loaded with photosensitizer. Cells are only exposed to the low levels of photosensitizer molecules that diffuse out of the substrate into a large volume of cell culture media.

The change in experimental direction has proven to be fruitful. In the next chapters, I describe the use of dynamic mask-based micro-3D printing and imprinting to successfully introduce topographical changes into a culture of fibroblast cells and influence their behavior.

2.6 REFERENCES

1. Tathireddy P, Rieth L, Sharma A, Solzbacher F. Implantable microsystems and neuro electronic interfaces. 2009 IET Bionic Health: Next Generation Implants, Prosthetics and Devices. 2009. p. 1–22.

2. Rutten WLC, Smit JPA, Frieswijk T., Bielen J., Brouwer AH, Buitenweg JR, et al. Neuro-electronic interfacing with multielectrode arrays. IEEE Engineering in Medicine and Biology Magazine. 1999 May;18(3):47–55.

3. Kaehr B, Allen R, Javier DJ, Currie J, Shear JB. Guiding neuronal development with in situ microfabrication. Proc Natl Acad Sci USA. 2004 Nov 16;101(46):16104–8.

4. Kaehr B, Ertas N, Nielson R, Allen R, Hill RT, Plenert M, et al. Direct-write fabrication of functional protein matrixes using a low-cost Q-switched laser. Anal Chem. 2006 May 1;78(9):3198–202.

5. Pitts JD, Campagnola PJ, Epling GA, Goodman SL. Submicron Multiphoton Free-Form Fabrication of Proteins and Polymers: Studies of Reaction Efficiencies and Applications in Sustained Release. Macromolecules. 2000 Feb 5;33(5):1514–23.

6. Lu CY, Liu YY. Electron transfer oxidation of tryptophan and tyrosine by triplet states and oxidized radicals of flavin sensitizers: a laser flash photolysis study. Biochim Biophys Acta. 2002 May 10;1571(1):71–6.

7. Bird RB, Stewart WE, Lightfoot EN. Transport Phenomena, 2nd Edition. 2 edition. New York: Wiley; 2001. 895 p.

8. Krystosek A. Neurite formation by neuroblastoma-glioma hybrid cells (NG108-15) in defined medium: stochastic initiation with persistence of differentiated functions. J Cell Physiol. 1985 Nov;125(2):319–29.

9. Higashida H, Furuya S. Cholinergic synapse formation between NG108-15 and muscle cells and modulation of transmission. Neurosci Res Suppl. 1990;13:S75–79.

10. Einstein A. Investigations on the Theory of the Brownian Movement. BN Publishing; 2011. 132 p.

11. Truskey GA, Yuan F, Katz DF. Transport Phenomena in Biological Systems. 2 edition. Upper Saddle River, N.J: Prentice Hall; 2009. 888 p.

12. Kaehr BJ. Defining Cellular Microenvironments Using Multiphoton Lithography [Doctoral]. [Austin, TX]: The University of Texas at Austin; 2007.

13. Nielson RY. Nonlinear laser microfabrication in biological environments [Doctoral]. [Austin, TX]: The University of Texas at Austin; 2007.

14. Liu J, Tu H, Zhang D, Zheng H, Li Y-L. Voltage-gated sodium channel expression and action potential generation in differentiated NG108-15 cells. BMC Neuroscience. 2012 Oct 25;13(1):129.

15. Greene LA, Tischler AS. Establishment of a noradrenergic clonal line of rat adrenal pheochromocytoma cells which respond to nerve growth factor. Proc Natl Acad Sci U S A. 1976 Jul;73(7):2424–8.

16. Foley JD, Grunwald EW, Nealey PF, Murphy CJ. Cooperative modulation of neuritogenesis by PC12 cells by topography and nerve growth factor. Biomaterials. 2005 Jun;26(17):3639–44.

17. Singh AV, Gailite L, Vyas V, Lenardi C, Forti S, Matteoli M, et al. Rapid prototyping of nano- and micro-patterned substrates for the control of cell neuritogenesis by topographic and chemical cues. Mat Sci Eng C. 2011 Jul 20;31(5):892–9.

18. Vogt AK, Brewer GJ, Offenhäusser A. Connectivity patterns in neuronal networks of experimentally defined geometry. Tissue Eng. 2005 Dec;11(11-12):1757–67.

19. Vogt AK, Brewer GJ, Decker T, Böcker-Meffert S, Jacobsen V, Kreiter M, et al. Independence of synaptic specificity from neuritic guidance. Neuroscience. 2005;134(3):783–90.

20. Vogt AK, Wrobel G, Meyer W, Knoll W, Offenhäusser A. Synaptic plasticity in micropatterned neuronal networks. Biomaterials. 2005 May;26(15):2549–57.

21. Offenhäusser A, Böcker-Meffert S, Decker T, Helpenstein R, Gasteier P, Groll J, et al. Microcontact printing of proteins for neuronal cell guidance. Soft Matter. 2007 Feb 14;3(3):290–8.

22. Hanson JN, Motala MJ, Heien ML, Gillette M, Sweedler J, Nuzzo RG. Textural guidance cues for controlling process outgrowth of mammalian neurons. Lab Chip. 2009 Jan 7;9(1):122–31.

23. Merz M, Fromherz P. Polyester Microstructures for Topographical Control of Outgrowth and Synapse Formation of Snail Neurons. Adv Mater. 2002 Jan 16;14(2):141–4.

24. Zhang J, Venkataramani S, Xu H, Song Y-K, Song H-K, Palmore GTR, et al. Combined topographical and chemical micropatterns for templating neuronal networks. Biomaterials. 2006 Nov;27(33):5734–9.

25. Law JK-Y, Yeung C-K, Li L, Rudd JA, Ingebrandt S, Chan M. The Use of SU-8 Topographically Guided Microelectrode Array in Measuring Extracellular Field Potential Propagation. Ann Biomed Eng. 2012 Mar 1;40(3):619–27.

26. Curtis A, Wilkinson C. Topographical control of cells. Biomaterials. 1997 Dec;18(24):1573–83.

27. Albrecht-Buehler G. Filopodia of spreading 3T3 cells. Do they have a substrate-exploring function? J Cell Biol. 1976 May;69(2):275–86.

28. Todaro GJ, Green H. Quantitative Studies of the Growth of Mouse Embryo Cells in Culture and Their Development into Established Lines. J Cell Biol. 1963 May 1;17(2):299–313.

29. Wang JH-C, Celechovsky C, Woo SL-Y. Effects of silicone microgrooves on 3T3 fibroblasts. [Engineering in Medicine and Biology, 1999 21st Annual Conference and the 1999 Annual Fall Meetring of the Biomedical Engineering Society] BMES/EMBS Conference, 1999 Proceedings of the First Joint. 1999. p. 781 vol.2.

30. Kaehr B, Shear JB. Mask-Directed Multiphoton Lithography. J Am Chem Soc. 2007 Jan 30;129(7):1904–5.

31. Nielson R, Kaehr B, Shear JB. Microreplication and Design of Biological Architectures Using Dynamic-Mask Multiphoton Lithography. Small. 2009 Jan 1;5(1):120–5.

Chapter 3: Multiphoton 3D-imprinting of hydrogels

3.1 INTRODUCTION

The hydrogel is a class of materials consisting of an extended three-dimensional network of hydrophilic polymer chains that are dispersed as a colloid in an aqueous medium. The high water content makes the material soft and deformable, while the three-dimensional network structure helps the bulk material retain its shape. Hydrogels can be synthesized from naturally-occurring substances such as alginate and gelatin, as well as from synthetic precursors such as acrylate, methacrylate and acrylamide monomers [1]. Hydrogels are often favored for biomedical applications because their water content and mechanical properties are similar to that of biological tissue [2]. For example, there is presently a developed market for the clinical use of hydrogels as contact lenses and wound dressings. Extensive research is being conducted for tissue engineering and controlled drug delivery, and these applications are beginning to reach clinical fruition.

Within the broad area of hydrogels, stimuli-responsive hydrogels are a particularly interesting category. These are materials whose properties, such as their crosslinking density, stiffness, hydrophilicity, and degradation rate, can be varied through the application of stimuli. Such stimuli could be exposure to light, pressure, or electricity, or changes in temperature, pH, or concentration of certain molecules [3]. Light has particular advantages over other stimuli as it can be delivered from a remote source and allows control over the spatiotemporal resolution of stimulation [2]. Photoresponsive hydrogels have been used in cell culture applications as two-dimensional surfaces and as three-dimensional matrices that encapsulate cells. Light stimulus has been used to release bioactive molecules, create chemical patterns, and vary local adhesion and stiffness [2].

A serendipitous observation in the Shear lab led to the use of light stimulation to introduce topographical changes to hydrogel surfaces. The Shear lab uses multiphoton excitation to chemically functionalize micro-3D printed materials by placing them in a solution of bioactive molecules functionalized with a photoreactive moiety, and scanning the material with a focused, pulsed laser beam. The high photon flux in the voxel locally photocrosslinks the molecule of interest to the material. Lab members Eric Ritschdorff and Jodi Connell noted that at high laser powers, the surface of the scanned material appeared to “collapse” relative to the adjacent unscanned material. While this phenomenon was undesirable in the context of chemical patterning, it had potentially interesting applications of its own. When material was printed in the form of a flat uniform pad, selective scanning produced a topographical relief pattern on the pad surface, such as the one shown in Figure 3.1. This phenomenon was dubbed “imprinting”.

While the mechanism behind this phenomenon was not fully understood, it was theorized that when material is first printed, it is only partially crosslinked. That is, it retains a population of crosslinkable residues. When the pad is scanned again, a fraction of these residues undergo crosslinking within the gel, leading to localized contraction of the gel that propagates to the surface of the material. This produces topographical changes on the surface.

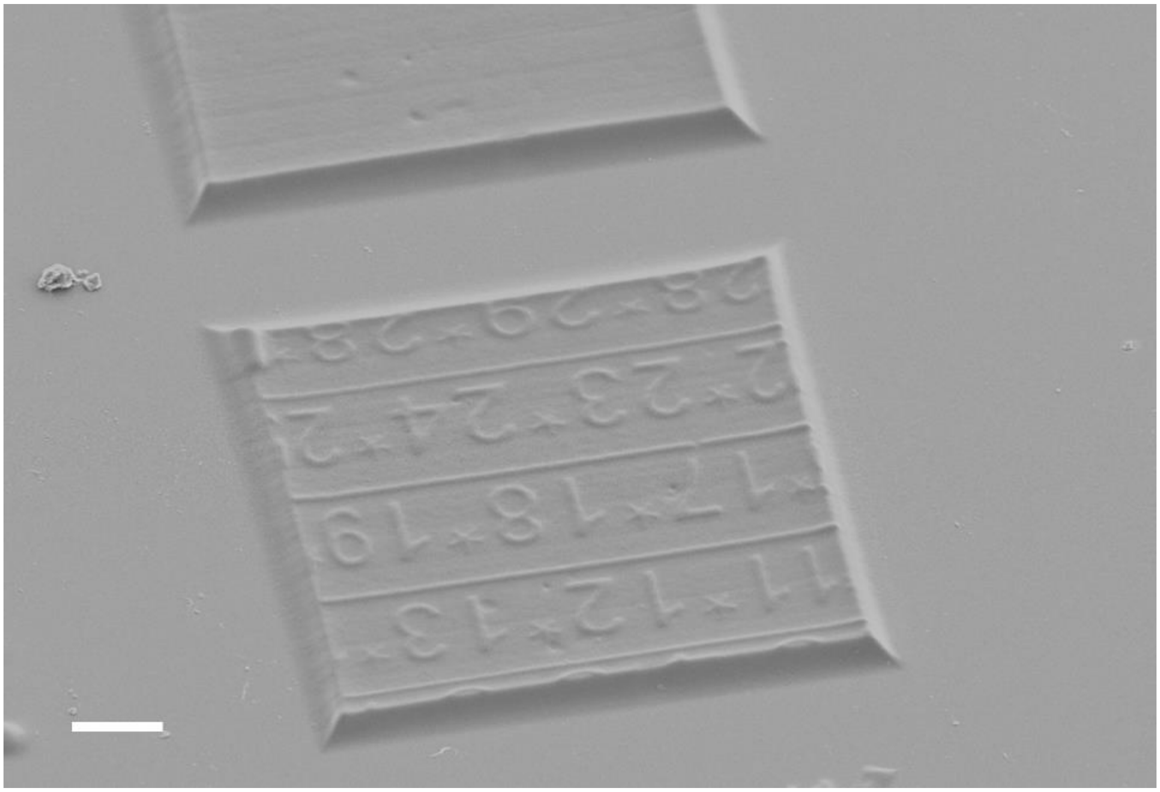

Figure 3.1: A micro-3D printed tile imprinted with a pattern of Arabic numerals, with an unimprinted tile in the background. Scale bar is 10 µm.

The imprinting phenomenon suggests a number of interesting applications. In biological environments, imprinting can introduce topographical changes to cell substrates, an application that is developed further in Chapter 4. There are distinct advantages of the use of imprinting in creating topographically varied surfaces when compared with other lithographic techniques (discussed in Chapter 1 and Chapter 2). The small voxel allows for fine control over the resolution of topographical changes in both the x-y plane (affecting the size of the imprinted pattern) and the z-direction (affecting the depth of imprinting). Temporal control over laser-scanning allows real-time imprinting, so the final pattern can be adapted on the fly to the spatial arrangement of cells rather than established at the beginning of the design cycle. A number of parameters, including laser power, photosensitizer concentration, number of scans, and location of scan, can be adjusted to control the final dimensions of the imprint.

This chapter explores the effects of many of these parameters on the imprinting process. First, the laser rig used for micro-3D printing and imprinting is detailed and the micro-3D printing of standardized hydrogel tiles is described. Next, there is an exploration of how depth of imprinting is affected by variations in the scanning process.

Finally, there is an examination of the loading and retention of photosensitizers in the printed material. The consistency of photosensitizer concentration and imprinting over the course of a 24 hour experiment is tested. By characterizing the imprinting parameters, a foundation is laid to develop applications where precise control of surface topography allows manipulation of micron-scale systems, including cellular microenvironments.

Further work on micro-3D imprinting, complementary to the work presented in this dissertation, has been conducted by Eric Ritschdorff, Jodi Connell, and Derek Hernandez. These studies were unpublished at the time of writing this dissertation, and the interested reader is encouraged to contact the Shear lab for details.

3.2 METHODS

Design and construction of a micro-3D-printing rig

The light source was a mode-locked titanium-sapphire (Ti:S) laser (Model 900 Mira, Coherent Inc., Santa Clara, CA) tuned to 740 nm. It produced ~150 fs pulses with a pulse repetition rate of 76 MHz. The beam was shuttered using an in-house constructed solenoid shutter (Magnetic Sensor Systems, Van Nuys, CA). The beam was scanned in a raster pattern using a small-beam-diameter scanning galvo mirror system (Thor Labs, Newton, NJ).

A series of lenses and mirrors (Thor Labs, Newton, NJ) were used to expand the laser beam and the scan area, as shown in Figure 3.2. The laser beam and scan area were focused and collimated in conjugate planes. The first lens (L1; focal length 60 mm) collimated the scan area while focusing the laser beam. The second lens (L2, focal length 150 mm) and third lens (L3, focal length 250 mm) expanded the laser beam and scan area, eventually focusing the beam onto a digital mirror device (DMD) from a repurposed digital projector (BenQ MP510 DLP Projector, BenQ, Costa Mesa, CA). The DMD had a pixel resolution of 800 by 600. It acted as a dynamic mask, displaying a super video graphics array (SVGA) image that selectively reflected or deflected portions of the raster scan. The masked scan pattern was then focused by the fourth lens (L4; focal length 300 mm), reflected off a dichroic filter, and focused through a high-power objective (60X, 1.4 NA, Nikon Instruments, Melville, NY) on an inverted microscope (TE-2000; Nikon Instruments, Melville, NY) onto a printing surface. To enable three-dimensional printing, the surface was translated vertically using a piezo-controlled nanopositioner (E-710, Physik Instrumente, Auburn, MA).

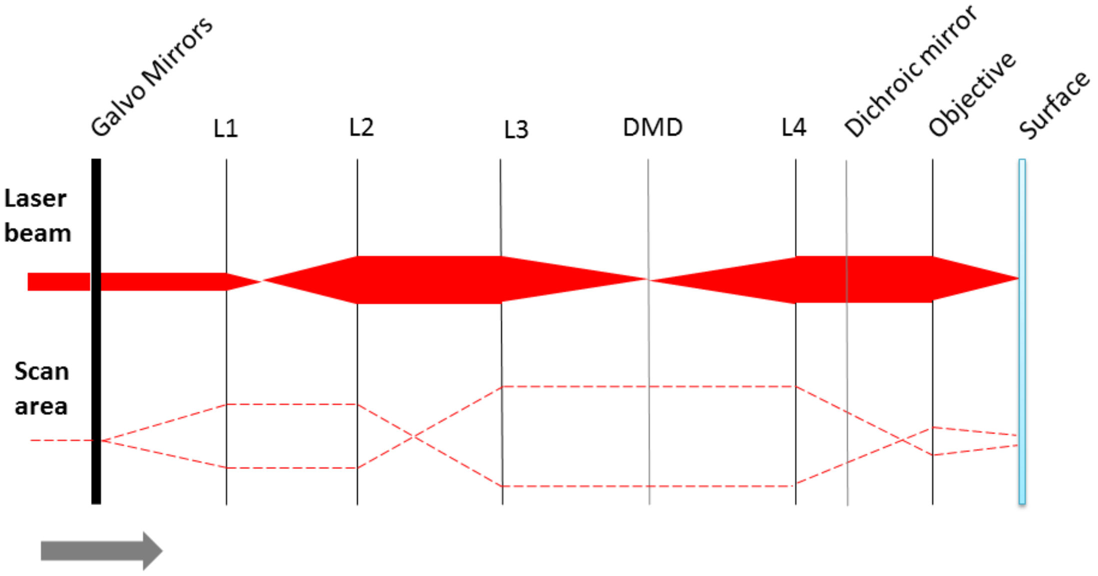

Figure 3.2: Schematic showing the arrangement of optical components that focus the laser beam and boundary of the laser scan area. The laser beam is scanned at the galvo mirrors, focused by lens L1, collimated by L2, focused by L3, and collimated by L4. The scan area is collimated by L1, focused at L2, collimated at L3, and focused at L4. The DMD mirror masks the scan area, and the dichoric mirror reflects the beam up to the objective, which focuses it onto the printing surface.

The repurposed digital projector was modified for this application as follows. The external casing was cut open, and the lens array in front of the DMD chip was removed to expose the chip to air. The projector lamp was removed and its circuit was closed with a jumper. This set of modifications is effective for converting the BenQ MP510 DLP Projector into a dynamic mask unit for the printing rig. Repurposing of other projector models may require different modifications.

Software control of rig components

The software for controlling and coordinating all instrument components of the micro-3D-printing rig was written using the LabView 2011 Professional Development System (National Instruments, Austin, TX).

The software was used to control the following instruments:

- The solenoid shutter was opened and closed to transmit or block the laser beam as needed.
- The scanning galvo mirror system was activated to scan the laser beam in a raster pattern. The scan angle and scan frequency were set using the software.
- The DMD chip image display was changed as needed so that the appropriate digital mask was used for each raster scan. The masks were binary JPEG files measuring 800 by 600 pixels. The mirror angles of the DMD chip tend to skew and rotate the raster scan, producing a distorted printed image. To rectify this distortion, the software applied a reverse skew and rotation transformation to the mask image files.
- The microscope stage translated the printing surface vertically in user defined steps that were coordinated with each raster scan and mask display.

Control signals were delivered to the solenoid shutter and scanning galvo mirror system through a PCI Digital Acquisition (DAQ) card (PCI-MIO-16XE-50; National Instruments, Austin, TX). The digital mirror device was controlled via a Super Video Graphics Array (SVGA) input. The nanopositioner was controlled via a General Purpose Interface Bus (GPIB) input (PCI-GPIB; National Instruments, Austin, TX).

Formulation of printing reagent solutions

Two formulations of the printing reagent solution were used for the experiments detailed in this dissertation. The formulation used for most experiments (referred to as low-gel) was based on a photosensitizer solution of 15 mM rose bengal (RB) in phosphate-buffered saline (PBS). To each 1 mL of this solution, 300 mg of bovine serum albumin (BSA) and 100 mg of type A porcine gelatin (gelatin) were added. The other formulation (referred to as hi-gel) consisted of a 9 mM RB solution in PBS, with 250 mg of gelatin and 25 mg of BSA added to each 1 mL of RB solution.

Each formulation was prepared by first adding the BSA to the RB solution in a 1.5 mL Eppendorf vial, mixing them on a vortexer, then heating the mixture to 60°C in an oven to dissolve. The gelatin was then added to the solution, vortexed to disperse it within the solution, and the final mixture was heated to 60°C to completely dissolve the gelatin.

The reagent solutions were plated on an ink-marked glass-bottom well (Mattek, Ashland, MA) for printing. The low-gel solution was applied to the glass with a transfer pipette while in the molten state. The hi-gel solution was too viscous for this method. Instead it was plated in the gel state– a small volume of the gel at room temperature was placed on the glass-bottom well and then melted at 60°C to spread onto the glass. Both types of solutions were cooled to a gel at room temperature and covered with a small volume of water to maintain hydration during printing.

Micro-3D-printing of the hydrogel tile

To maintain focus on the characterization of the imprinting process, I used a standardized printing protocol to produce structures. The glass-bottom well containing printing reagent solution was placed on the stage of the inverted microscope that formed part of the micro-3D-printing rig. The upper surface of the glass served as the printing surface. The laser beam was set to an average power of 35 mW at the objective back aperture and focused onto the printing surface. The beam was scanned in a raster pattern and masked to produce a square printing area measuring 70 μm by 70 μm. The scan along the fast axis consisted of a triangle wave with amplitude of 2 V and frequency of 200 Hz. The scan along the slow axis was also a triangle wave, with amplitude of 1.5 V and frequency of 0.1 Hz at an offset of 270°. These settings produced a velocity of 68,000 µm/s on the fast axis and 25 µm/s on the slow axis. The voxel was translated to a height H_0 = 10 µm above the glass surface using the nanopositioner, and then stepped downward one micrometer increments. The 1 µm step size was experimentally determined to produce solid structures through sufficient overlap of voxels in adjacent printed layers. The laser beam was scanned through the 70 µm by 70 µm printing area once per step until the printed structure was anchored to the glass surface. The gel consistency of the printing reagent at room temperature helped maintain the shape of the printed structure until it was anchored. The laser-scanned region was covalently photocrosslinked into a solid structure, while the unscanned region was melted and rinsed away using PBS warmed to 60°C. The remaining structure had lateral dimensions of 70 µm by 70 µm, and a nominal height of 10 µm, and is referred to as a “tile”. While the nominal height of the tile was set by the total distance that the printing voxel was translated along the optical axis into the solution to print the top layer of the tile, the actual height of the tile could vary for a number of reasons. For one, the voxel itself is elongated along the optical axis. If the waist of the voxel is focused 10 µm above the glass, the highest point of the voxel may extend above it by a micron or more, depending on the light intensity and the photoreaction efficiency of the reagent solution. Printed structures are also known to undergo swelling when the reagent solution is rinsed away, increasing the height by approximately a micron.

The printed tile was stored overnight in a 50% ethanol solution, which extracted much of the RB photosensitizer. The next day, the ethanol solution was replaced with a 5 mM solution of the biocompatible photosensitizer eosin Y in PBS. The printed tile was loaded with eosin overnight and then stored in the same solution. It was transferred to PBS immediately before use.

Imprinting pattern into tile surface

The glass-bottom well containing the printed tile structure was emptied of the eosin-loading solution and filled with PBS to keep the tile hydration. The well was placed on the stage of the micro-3D-printing rig, and the voxel was focused on the glass surface at the bottom of the printed tile. A mask was selected in a pattern corresponding to the desired imprinting pattern. In this chapter, each tile was imprinted uniformly so the mask was a flat square corresponding to the size of the tile. Uniform imprinting changed the height of the tile as the entire material contracted and pulled the surfaces downward.

The voxel was moved to a height H_0 above the glass surface (Figure 3.3 (a)), then stepped downward one micrometer at a time (Figure 3.3 (b)) until the voxel was within at least 3 µm of the glass (Figure 3.3 (c)). Each plane during this downward sequence was raster scanned by the laser focus in a pattern set by the imprinting mask, maintaining a fast axis velocity of 68,000 µm/s and slow axis velocity of 25 µm/s. For imprinting done with multiple scans, the voxel was again returned to height H_0 and the procedure was repeated one or more times as indicated. The structure was stored in PBS until further use to maintain hydration.

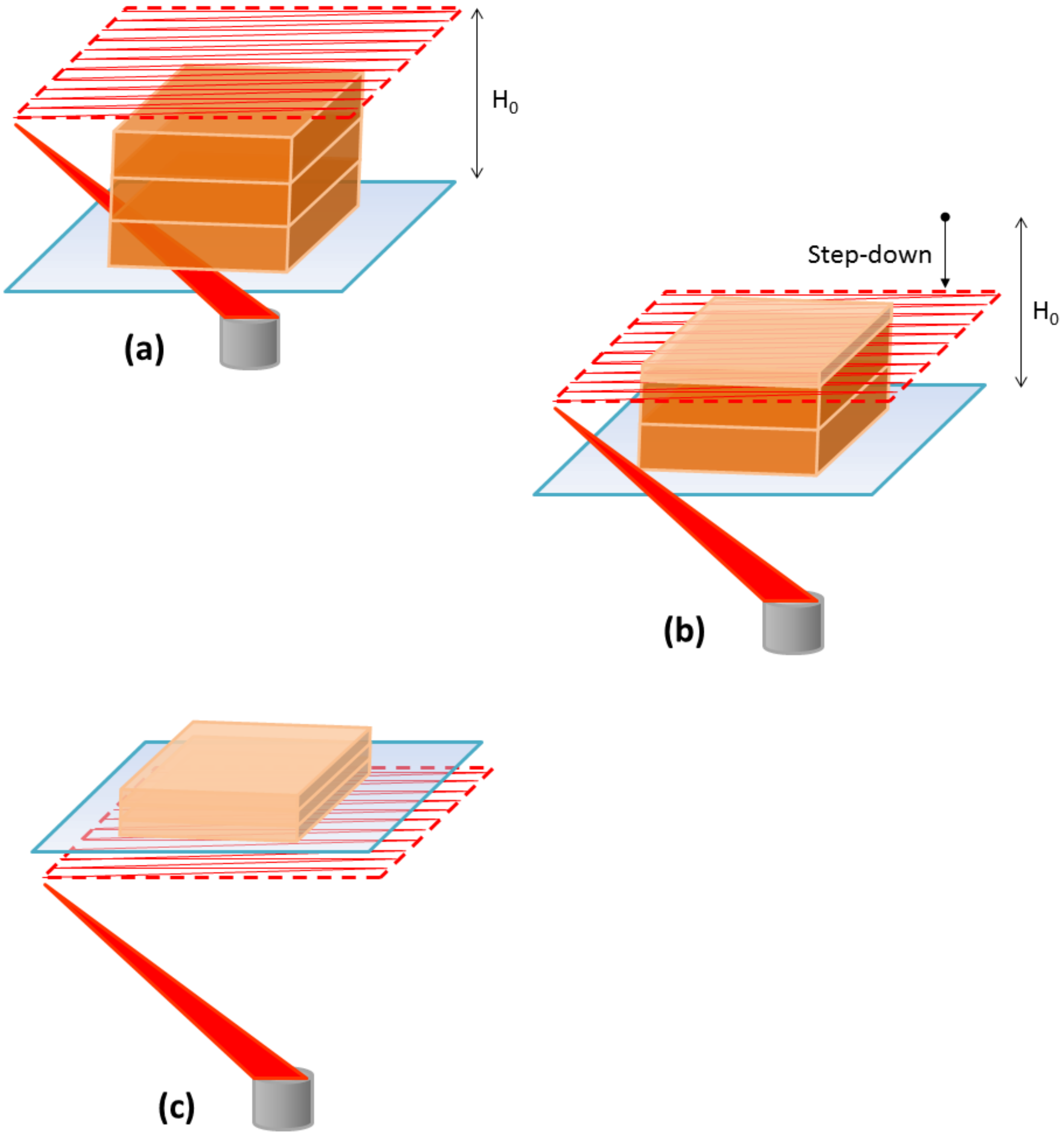

Figure 3.3: A schematic of the imprinting process. The laser beam voxel, scanned in a raster pattern, is positioned at H_0 (a). It is stepped down 1 μm at a time (b) until it is below the glass surface. The tile structure is imprinted layer-by-layer as the laser beam passes through it. Dark orange represents unimprinted material and light orange represents imprinted material, which has undergone a change in height.

Measurement of the height of a tile

Although tiles were printed with a nominal height of 10 μm, they needed to be measured to confirm the actual heights after removing the reagent solution. Variations between the nominal heights and actual heights may arise from material swelling, from imperfect focusing of the voxel on the glass, and from the portions of the printing voxel extending above the top plane. Additionally, the surface patterns and/or heights of structures needed to be determined after imprinting. Negative-space confocal imaging was used to measure the heights of these tiles. The region around the printed tiles was flooded with a fluorescent dye, and the space occupied by the printed tile was distinguished by its much lower fluorescence signal. The fluorescent dye was a 35-40 mg/mL solution of fluorescein isothiocyanate conjugated to dextran molecules of molecular weight 2 MDa (FITC-dextran; FD2000, Sigma Aldrich, St. Louis, MO). It had an excitation wavelength maximum at 490 nm and emission maximum at 520 nm. The large tethered dextran molecules prevented the fluorescein from penetrating the printed tiles, thus providing a high fluorescence signal contrast between the tiles and the surrounding region.

The PBS was removed from the glass-bottom wells containing printed tiles and quickly replaced with the dye to prevent dehydration. The tiles and their surrounding regions were imaged on a confocal microscope (SP2 AOBS; Leica Microsysrems, Buffalo Grove, IL) using a 63X (HCX APO, 1.4NA) oil objective. The samples were excited with a 488 nm Argon laser. Emitted light was collected in the range 496nm - 675nm. Longer wavelength emission was excluded to avoid collecting light emitted from eosin in the structures. PMT gain was set to 480 V to maximize contrast between the structures and the FITC-dextran dye. The pinhole size was 20.0 μm (0.17 airy disk), and the laser scan rate was 400 Hz. Voxel dimensions were 465 nm × 465 nm × 115 nm. Images were captured in the form of stack files.

Orthogonal projections of the images were computed using the imaging software FIJI [4], and tile dimensions were obtained from pixel measurements. The measured heights of structures without imprinting were denoted H_i, and the heights of imprinted structures were denoted H_f.

Measurement of photosensitizer concentration in tile

The concentration of eosin in the printed tile was calculated from Beers' law after measuring the relative transmittance of light passing through the tile. As the small size of the tile made standard UV/Vis spectrophotometers an unsuitable instrument for measuring relative transmittance, these measurements were made on an inverted microscope (Axiovert 135; Zeiss Microscopy, Thornwood, NY). Near monochromatic light was obtained by filtering full spectrum light from a tungsten-halogen lamp through a 530 nm bandpass filter (FB530-10; ThorLabs, Newton, NJ). The condenser diaphragm of the microscope was closed to minimize variation in light path lengths. A 10X objective (UPlanFl 10X/0.3 NA; Olympus America, Center Valley, PA) collected light that passed through printed tiles and the surrounding regions. Brightfield images of 16-bit depth were collected with a scientific-grade complementary metal oxide semiconductor (CMOS) (ORCA-Flash2.8; Hamamatsu Photonics, Bridgewater, NJ) camera controlled by HCImage Live software (Hamamatsu). Pixel intensities were measured from images of both printed tiles and surrounding regions without printed structures.

The molar absorptivity of the eosin in the printed structures was needed to calculate approximate concentrations of the dye remaining in tiles at different times. A series of hi-gel solutions was prepared containing eosin concentrations less than or equal to 10 mM. These gels were sandwiched between pairs of coverslips separated by 30 μm glass beads. Gel sandwiches were imaged on the inverted microscope through the 530 nm filter, and relative transmittance measurements were obtained from pixel intensity values of images captured by the CMOS camera. Although the absorbance was measured away from the absorbance peak of eosin at 517 nm, a calibration curve confirmed that absorbance at 530 nm varies linearly with concentration. Using the Beer-Lambert law, the molar absorptivity coefficient was calculated to be 33,000 $(M\ cm)^{-1}$ at 530 nm. This value was verified using protein-free eosin solutions measured using a cuvette-based UV-Vis spectrophotometer (8453 UV-Vis; Agilent Technologies, Santa Clara, CA).

Diffusion of photosensitizer from tile

To measure diffusion of eosin out of printed tiles, the tiles were removed from 5 mM eosin solution and placed in Liebovitz-15 media containing 1% bovine calf serum, then maintained at 37°C in a non-CO_2 incubator. The media and temperature conditions were selected to match cell culture conditions that will be relevant in Chapter 4. At several time points, the concentration of eosin in the tiles was measured using the method described previously.

Imaging via Scanning Electron Microscopy

Selected structures were fixed using a 5% solution of gluteraldehyde (Ted Pella, Redding, CA) in PBS for one hour, then rinsed with deionized water to remove buffer salts. Structures were serially dehydrated in 50% ethanol and twice in 100% ethanol, then dried in a carbon dioxide critical point dryer (Samdri 790 CPD; Tousimis, Rockville, MD) in which liquid carbon dioxide was exchanged five times. The dried structures were mounted on SEM pin stubs, sputter coated to a nominal thickness 8 nm of platinum-palladium, and imaged in a field emission-scanning electron microscope (Supra 40 VP, Zeiss Microscopy, Thornwood, NY) using the secondary electron detector. The extra high tension (EHT) was set at 5.0 kV and the working distance was 16.0 mm.

3.3 RESULTS

The purpose of the work presented in this chapter was to develop the imprinting phenomenon observed in the Shear lab into a method for introducing topographical variations to the surfaces of protein-based hydrogel structures. During preliminary studies, it was observed that a wide range of parameters influence the extent of imprinting that a structure experiences when scanned with a laser. Imprinting is affected by the qualities of the structure material, which in turn depend on the printing process. The composition of the reagent solution, the power and dwell-time of the laser, and the step-size of the voxel translation all affect the crosslinking density and the stiffness of the printed material. The laser power, dwell-time and step-size, also determine the extent of imprinting, as does photosensitizer concentration.

The materials developed in this section fall in the class of protein hydrogels. Proteins were used as precursors for the printed structures because of their demonstrated utility in micro-3D printing [5–8]. The selected proteins, BSA and gelatin, have been shown to make good precursors for biologically relevant hydrogels because of their biocompatible nature, particularly their similarity to proteins in blood sera and ECM [9]. The resulting printed structures have both high water content and flexibility. The amount of each protein can be varied to produce structures with different properties. For this project, BSA was used to provide structural support and stiffness while gelatin lowered the gelation temperature of the reagent solution, permitting top-down printing of structures. Gelatin may also contribute collagen-like moieties to facilitate cell adhesion.

Of the two formulations used in this project, the structures printed with hi-gel solution were softer and more easily distorted than structures from low-gel solution. One reason is that the hi-gel formulation has a lower total protein concentration (275 mg/mL) than the low-gel formulation (400 mg/mL), as higher protein content makes for denser and stiffer material. Secondly, BSA has more crosslinking residues than gelatin, as discussed previously in Chapter 1. Structures containing more BSA can potentially contain more covalent crosslinks, leading to a stiffer material. At elevated temperatures (e.g. those suited for cell culture, around 37°C) hi-gel structures can become even softer as physical crosslinks (intertwined collagen-like triple helices) between gelatin strands denature. Figure 3.4 shows a hi-gel structure deforming under the contractile force of a cell adhered to it. Because it produces structures more suited for the applications in Chapter 4, the low-gel formulation is the primary focus of the characterization performed in this chapter.

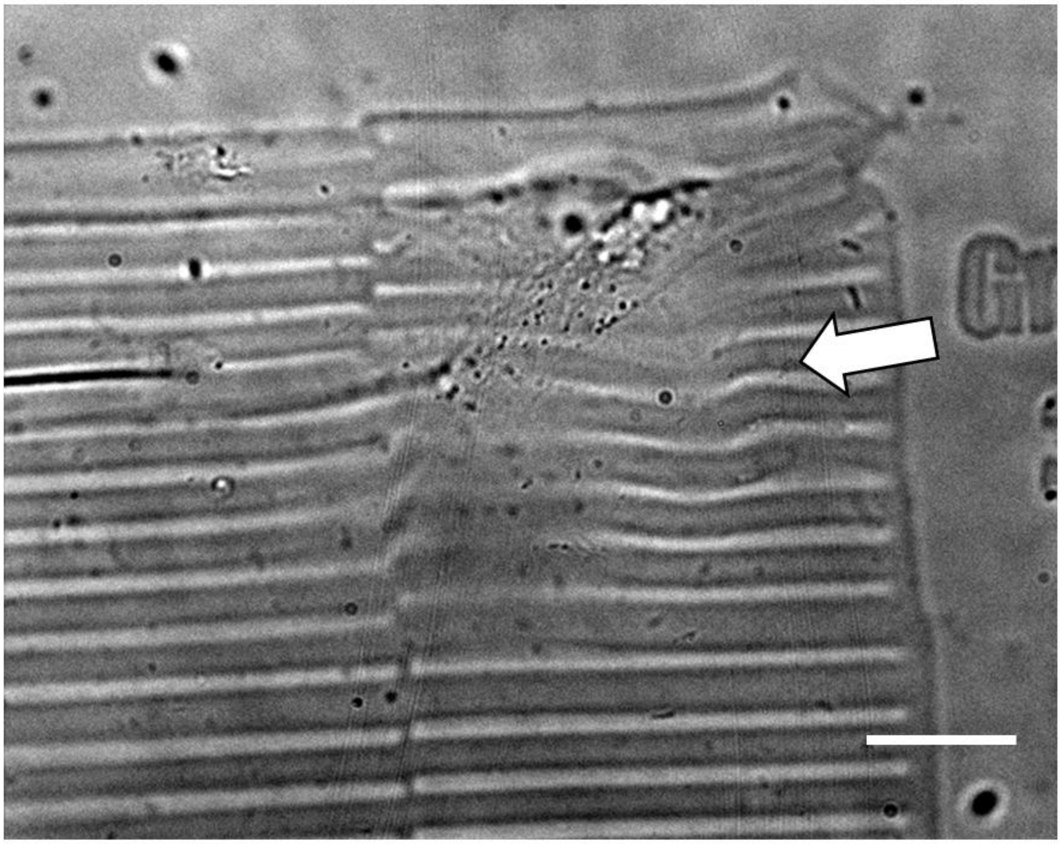

Figure 3.4: Hi-gel material distorted under applied force. A hi-gel micro-3D printed tile was imprinted with parallel grooves. A fibroblast that was adhered to the cell applied contractile forces that were strong enough to distort the material at 37°C, as indicated by the arrow. Scale bar is 20 µm.

The other important component of the reagent solution, the photosensitizer, was selected based on crosslinking efficiency and biocompatibility. Rose bengal is a more efficient photosensitizer than eosin and sensitizes more photocrosslinking reactions. However, it is also more cytotoxic. To print robust structures that maintain their shape over time, I used rose bengal as the photosensitizer for the printing reagent solution. I then rinsed out the rose bengal and reloaded the material with eosin. This yielded a more biocompatible imprinting material that could be used for the cell studies detailed in Chapter 4.

Dimensions of printed structures

The dimensions of micro-3D printed tile structures were measured using negative space confocal imaging. These tiles were formulated with low-gel printing reagent and their nominal heights, as determined by the set-point of the printing voxel above the glass printing surface, were 10 µm. The nominal length and width of each tile, as determined by the raster scan mask, were 70 µm each. A total of 18 tiles were printed in three different wells. Table 3.1 summarizes the averaged length, width, and height measurements of the tiles.

Dimension	Mean (µm)	Standard Deviation (µm)
Height	10.5	0.4
Length	69.4	1.2
Width	70.7	1.0

Table 3.1: The dimensions of micro-3D printed tile structures were measured. The mean and standard deviation are shown. Sample size n = 18.

The resolution of the confocal image is 0.115 µm in the z-axis, and 0.465 µm in the x- and y-axes. The standard deviation arises from measurement noise, which is three pixels in magnitude in all three dimensions (0.345 µm on the z-axis and 1.395 µm on the x- and y-axes).

Effect of imprinting on tile height as the number of scans varies

Imprinting a structure by scanning multiple times produced deeper patterns than a single scan. To quantify these effects, a series of tiles were printed and then imprinted by scanning with a laser beam layer by layer through their entire height. Different tiles were scanned once, twice, or three times. A total of 3 tiles were subjected to each scanning pattern.

To ensure the entire height of the tile was scanned, the initial position of the voxel (H_0) was placed at 15 µm, which was higher than the heights of the tiles. After imprinting, the heights of these tiles were compared, as shown in Figure 3.5.

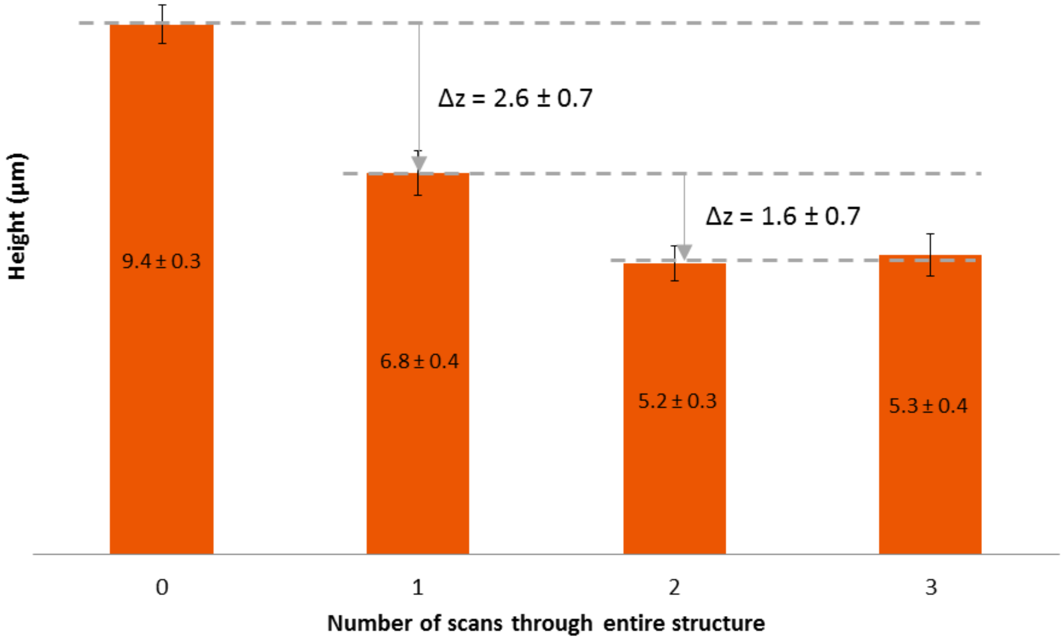

Figure 3.5: Number of imprinting scans. The mean and standard deviation of tile heights (µm) are shown, after scanning once, twice, or three times through the entire structure. Δz represents change in height produced by the last scan. n = 3.

The first scan through the tile produces the most dramatic change in height, from an average of 9.4 µm to 6.8 µm, a change of 30% from the original height. The second scan produces a smaller height change, from 6.8 μm to 5.2 μm, a change of 24% from the first scan. A t-test (assuming unequal variances) was performed to compare the mean heights after the second and third scans. The null hypothesis, that the two sets of heights had the same mean, could not be rejected as the p-value was 0.61. Thus, it was concluded that the third scan doesn't change the height further by a significant amount

The effects of scanning multiple times can be explained by considering that within each tile, there is a finite population of crosslinkable amino acid residues available to undergo photocrosslinking during imprinting. The first imprinting scan induces a reaction in a large fraction of them, producing covalent bonds that contract the material and reduce the tile height. The second imprinting scan crosslinks a large fraction of the remaining residues, further reducing the tile height. By the third scan, the number of available residues is so small that crosslinking does not contract the material significantly. Therefore the height does not change further.

Effect of imprinting on tile height as the scan height varies

There may be circumstances in which one would like to imprint a structure while minimizing the exposure of the structure surface to the scanning laser. This may be necessary if the surface of the structure is being used as a substrate for cell growth. It may also be needed if the surface has been functionalized with chemistry that is susceptible to photo-damage. In these cases, imprinting can be achieved by placing the voxel at a height H_0 that is lower than the maximum height of the structure, and then scanning downward layer by layer until the glass level is reached. By scanning through a fraction of the full height of structure, the localized contraction necessary for imprinting can be attained while leaving the top surface of the structure unexposed. Here, H_0 is referred to as "scan height". To quantify the effect of varying the scan height, a series of tiles were printed and then imprinted starting from scan heights of 8 µm, 10 µm, 12 µm, and 14 µm. Each tile was scanned twice, from the scan height down to the glass level. A total of 6 tiles were subjected to each scanning pattern. The results are displayed in Figure 3.6.

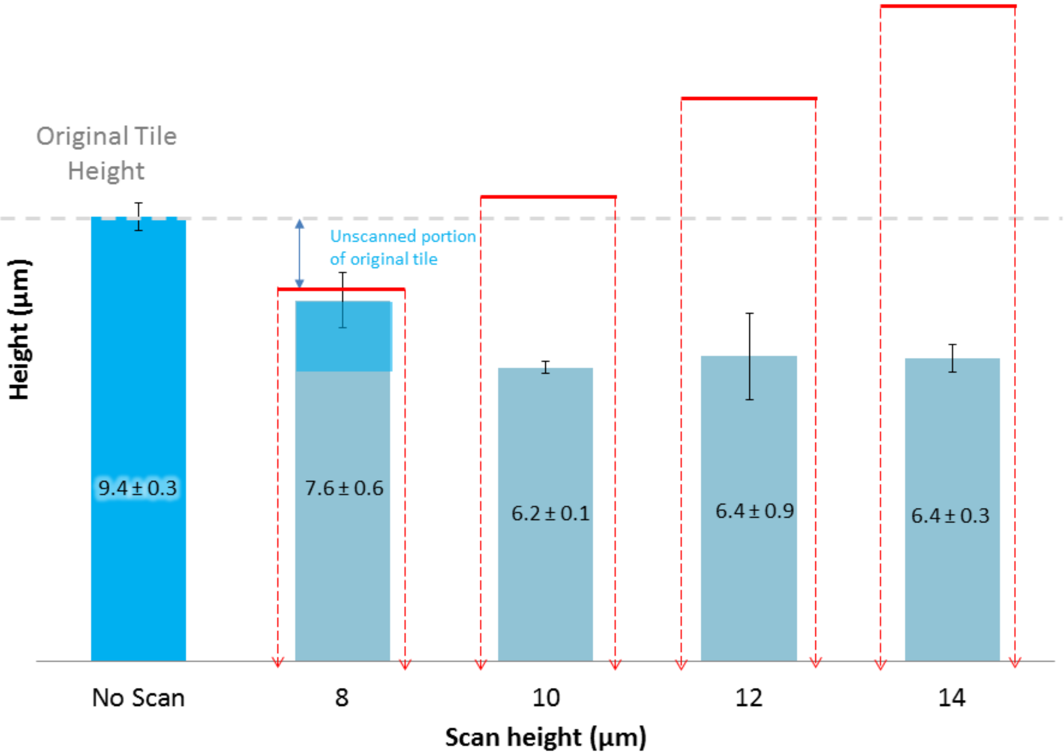

Figure 3.6: Imprinting scan height. The mean and standard deviation of tile heights are shown after being scanned twice through different scan heights (indicated by horizontal red bars). Dark blue indicates unscanned portions of tiles. Light blue indicates scanned portions. n = 6.

When the scan height (H_0) is less than the initial height (H_i) of the tile, as in the case of 8 µm scan height, the imprinted tile consists of a contracted section at the bottom (light blue in Figure 3.6) and an uncontracted section at the top (dark blue in Figure 3.6). The heights of both these sections contribute to the final height of the structure, H_f.

On the other hand, when the scan height (H_0) is more than the initial height (H_i) of the tile, as in the case of 10 µm, 12 µm and 14 µm scan heights, the entire structure is scanned. As a result, the final height (H_f) reflects the fact that the entire tile structure underwent contraction.

Photosensitizer concentration in printed tiles

The presence of photosensitizer in the structure appears to be necessary for imprinting, as it enables the photocrosslinking reactions that are responsible for contracting the material. However, the photosensitizer used for imprinting in this work, eosin, is water-soluble. Since printed hydrogel structures are kept in aqueous solution to prevent dehydration damage, the photosensitizers can diffuse out of the structures by dissolving in the aqueous solution. If the photosensitizer levels are depleted too much, imprinting can be affected.

To achieve reproducible imprinting, it was important to maintain photosensitizer concentrations in the pad at levels that induce a sufficient amount of photocrosslinking reactions. To ensure that photosensitizer levels were consistent, a reliable method for measuring the photosensitizer concentration was needed. Since eosin has an easily detectable absorbance peak of 517 nm and a high molar absorptivity, spectrophotometry was used for concentration measurements.

It wasn't possible to use conventional UV-Vis spectrophotometers, which use micro-well plates or cuvettes to hold samples, as the printed gel tiles were too small. Instead, an inverted microscope was used to image the tiles under near-monochromatic light. The relative intensity of light transmitted through the pad was taken from pixel intensity measurements from images captured by a CMOS camera, and the Beer-Lambert Law was used to calculate the concentration of eosin in the tile.

The Beer-Lambert law relates the attenuation of light to properties of materials through which it passes, such as concentration and path length. It can be expressed in the form of Equation (1), where I_0 is the intensity (power per unit area) of the incident light, I is the intensity of the transmitted light, c is the concentration of the light-attenuating material, l is the path length of light passing through the material, and ε is the molar absorption coefficient, a constant of proportionality that is specific to the material.

$$A = \log\left(\frac{I_0}{I}\right) = \varepsilon c l \qquad \textbf{(5)}$$

For the Beer-Lambert law to be valid, there are certain conditions that need to be upheld in the system being measured. The molecules in the material must interact with light independently of each other. The material must be homogeneous and not scatter light and the incident light must consist of parallel rays that traverse the same path length through the material. Finally, the light must be either monochromatic,or at the least have a bandwidth narrow enough that absorbance does not vary across it [10].

In this setup, these conditions were met as follows. The sample was illuminated with light from a microscope condenser, with the condenser diaphragm minimized so that light rays were limited to a small range of path lengths. The light was made monochromatic using a 530 nm filter with a bandwidth of 10 nm. Although this wavelength deviated slightly from the wavelength of maximum absorbance for eosin (λ_{max} = 517 nm), a measured absorbance vs. concentration curve showed that it followed the Beer-Lambert law. As the tile was thin and optically clear, the assumption was made that it did not scatter or interact with light.

The intensity ratio of incident (I_0) to transmitted light (I) was inferred from measured pixel intensities in an image of the illuminated sample captured with a CMOS camera. This ratio (I/I_0) was taken as equal to the ratio of pixel intensities on the sample vs. the surrounding area. Here, the eosin-loaded gel was the material absorbing the incident light. The light passed through a path length (l) equal to 10 μm, the thickness of the tile. The light detected by the CMOS camera had been attenuated by the eosin in the material. The light passing through a surrounding region would not undergo the same attenuation before being detected by the CMOS camera. In an analogy with a conventional spectrophotometry measurement, the surrounding region was the "reference" and the loaded tile was the "sample". One caveat: a true "reference" would consist of a printed tile that had been completely depleted of eosin. Such tiles were found to have the same pixel intensity as the surrounding area without printed tiles so for convenience, areas surrounding loaded tiles were treated as sample references.

The molar absorption coefficient (ε) for eosin at 530 nm was experimentally found to be 33,000 $(\mathrm{M\ cm})^{-1}$ using the "sandwich method" described in the Methods section. The plot of absorbance vs. concentration-times-path length used to find ε is shown in Figure 3.7. Using the path length, molar absorption coefficient and intensity ratio, the concentration of eosin loaded in the printed material was calculated.

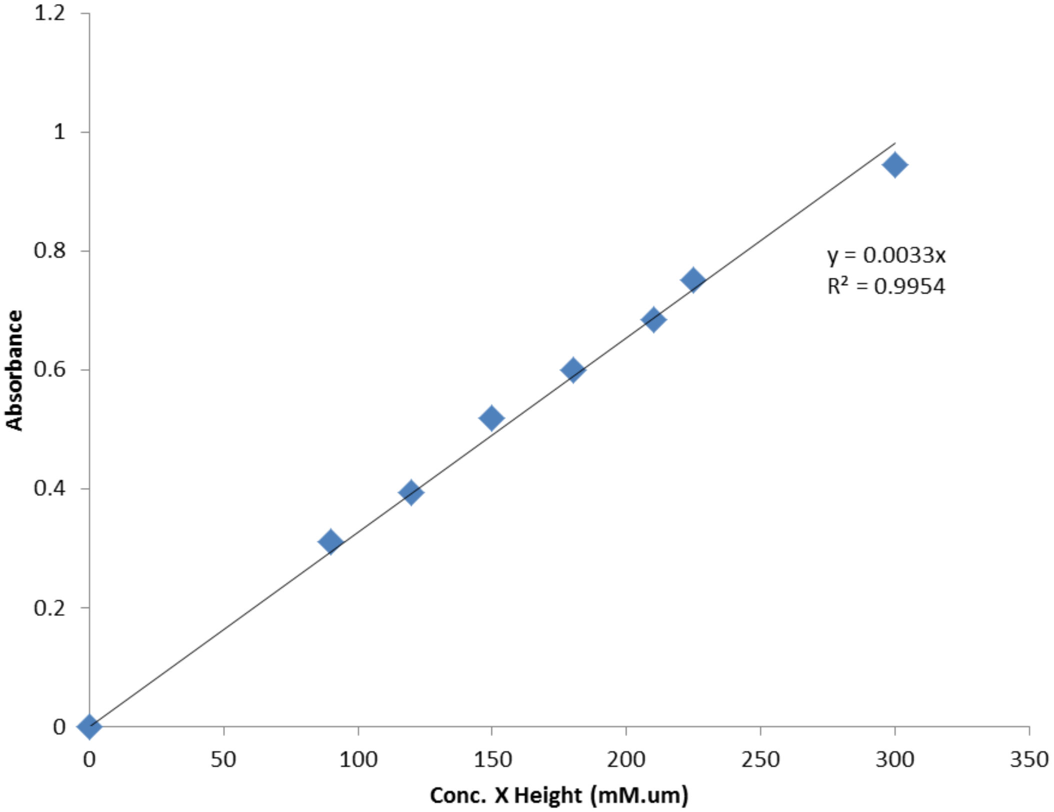

Figure 3.7: Calculation of molar absorption coefficient of eosin in hi-BSA tile. The slope of this linear regression shows that the molar absorption coefficient was 0.0033 (mM µm)$^{-1}$ or 33,000 (M cm)$^{-1}$.

The concentration of eosin was measured in structures that had been loaded with the photosensitizer by equilibration in a 5 mM eosin solution overnight. Immediately after removal from the loading solution, the material had an eosin concentration of 33 ± 2 mM, which was much higher than the loading solution concentration. The distribution ratio of eosin between the protein gel phase and aqueous phase was calculated to be 6.6. The high distribution ratio is supported by literature that documents the high affinity between BSA proteins and xanthene dyes such as eosin and rose bengal [11,12].

To assess how long eosin is retained in structures when kept in aqueous media, loaded tiles were incubated in L-15 media at 37°C. The concentration of eosin in the tiles was measured at various time intervals and plotted. Figure 3.8 plots the change in concentration in three samples over 24 hours.

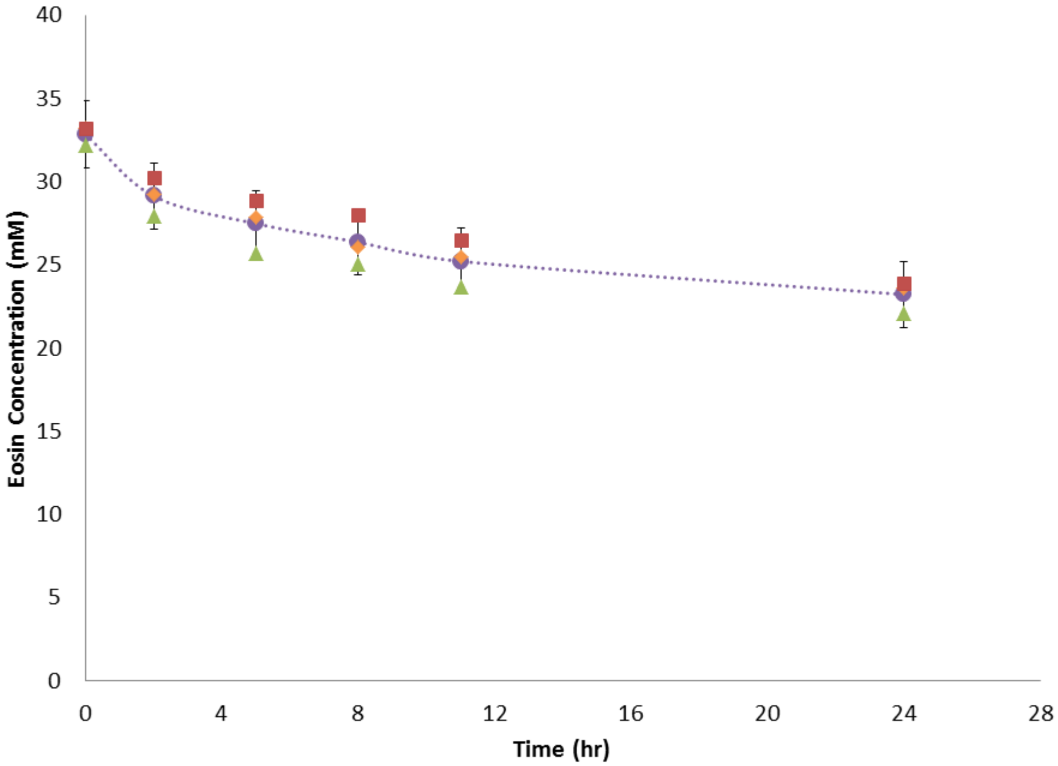

Figure 3.8: The concentration of eosin in the loaded tile structure plotted against time for 24 hrs. The symbols ◆, ■ and ▲ represent replicates while ● represents their average. Error bars represent the standard deviation of measurement.

Over 24 hours, the eosin concentration of a second set of tiles decreased from an initial value of 33 mM to 23 mM, and the release rate decreased with concentration. The change in concentration in another set of samples over 9 days is shown in Figure 3.9.

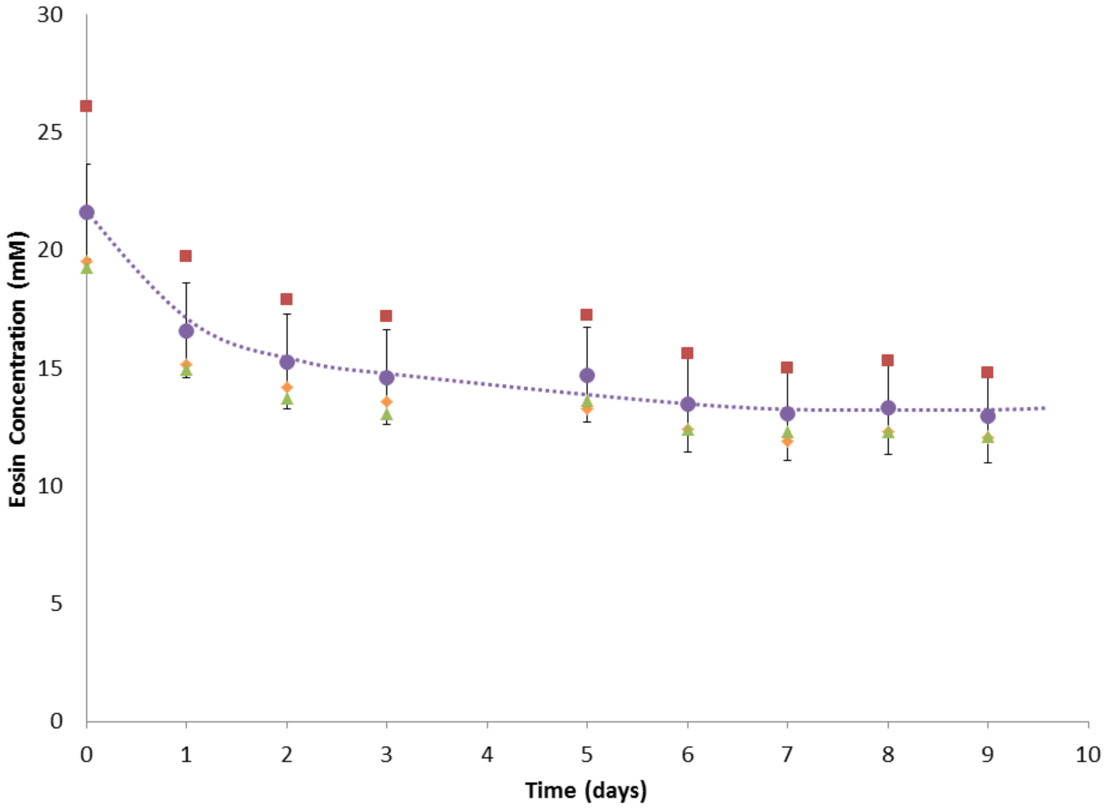

Figure 3.9: The concentration of eosin in the loaded tile structure plotted against time for 9 days. The symbols ◆, ■ and ▲ represent replicates while ● represents their average. Error bars represent the standard deviation of measurement.

Over 9 days, the concentration decreased from 22 mM to 13 mM in an initial burst over 2 days followed by a slower change during the next 7 days. Toward the end, the concentration reached a near-steady state at a non-zero concentration. The two distinct trends – the initial concentration dependent release rate and the later constant release rate – suggest that the eosin was released from the material by at least two distinct mechanisms, denoted Mechanism 1 and Mechanism 2 respectively.

The eosin concentration curves in Figure 3.8 and 3.9 are not directly comparable because of the different initial concentrations. (This variation in eosin loading concentration possibly stemmed from small variations in BSA content when printing reagents were mixed). However, when presented as fractional concentration curves (relative to their respective initial concentrations) they can be concatenated as shown in Figure 3.10. This fractional concentration curve was used to project the data from Figure 3.8 over 9 days, also shown in Figure 3.10 via the right-hand axis.

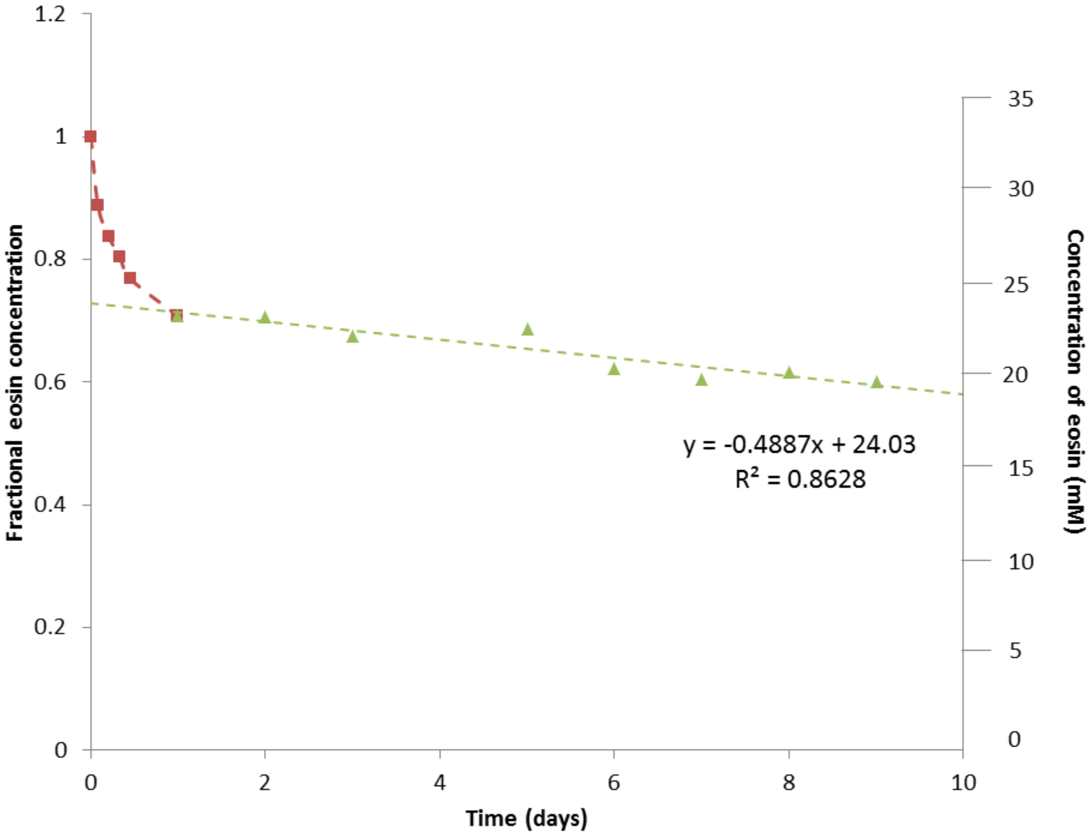

Figure 3.10: Plot of the concentration of eosin in structures over 9 days, presented as a fraction of initial concentration (left axis) and as total concentration (right axis). The ■ markers indicate the phase where Mechanism 1 dominates, and the ▲ markers indicate the phase where Mechanism 2 dominates. The total concentration values in the latter phases were estimated from the fractional concentrations. The segmented linear regression shows how concentration varies linearly with time over the observed period when Mechanism 2 dominates.

The red markers indicate data that was measured during the first 24 hours of eosin release. This part of the curve also corresponds to the phase when Mechanism 1 dominates over Mechanism 2. The green markers indicate data that was estimated from fractional concentration data over 9 days. This part of the curve corresponds to the phase when Mechanism 2 dominates.

The concentration change from Mechanism 2, when modeled as a linear relationship with time using a simple linear regression, yields an R^2 value of 0.86. In other words the release rate is constant at 0.49 mM/day (5.8×10^{-6} mM/sec) and independent of the concentration of eosin. This indicates that the release of eosin from the material by Mechanism 2 follows zero-order release kinetics over the time-scale of interest. The release of eosin by Mechanism 1 can be calculated by subtracting the contribution of Mechanism 2 from the total concentration data. This produces an adjusted concentration curve in which the concentration decreases from 9 mM to 0 mM, instead of 33 mM to 20 mM.

A semi-empirical equation can be used to assess the eosin release behavior from the structure via Mechanism 1. The Ritger-Peppas Power Law is used to determine the diffusional exponent (n), a parameter that is indicative of the transport mechanism [13]. A diffusional exponent n of 0.50 indicates Fickian diffusion, i.e. following Fick's laws of diffusion. A diffusional exponent of 1 indicates zero-order i.e. concentration independent diffusion. An exponent between these limits displays characteristics between these two limits, and is described as non-Fickian.

If M_t is the total amount of eosin that has diffused out of the structures via Mechanism 1 by time t, and M_∞ is the amount released after infinite time, the data can be fit to Equation (2).

$$\frac{\mathbf{M}_t}{M_\infty} = k\,t^n \tag{6}$$

When the log of fractional release (M_t / M_∞) was plotted versus the log of time (t), the diffusional exponent was determined to be 0.696 from the slope. This indicates a non-Fickian release behavior, although the character is more Fickian than zero-order. An attempt can be made to model the release of eosin from the tiles using Fick's second law of diffusion, Equation (3).

$$\frac{\partial C}{\partial t} = D\frac{\partial^2 C}{\partial x^2} \tag{7}$$

The model assumes a constant diffusion coefficient D for eosin diffusing out of the material, a plane sheet of thickness *l*. The material has an initial uniform eosin concentration $C(x, t=0) = C_0$, in which one surface is impermeable (anchored to glass, so $\partial C(x=0)/\partial x = 0$) and the other surface is held at a constant eosin concentration of $c(x=l) = C_S$. The aqueous media around the printed structures can be treated as a "perfect sink" for eosin, as the media volume is 10^8 times the volume of the structures. I am also making the assumption that eosin diffusing out of the structure immediately dissipates instead of accumulating in the vicinity of the pad. This assumption is facile because the aqueous media was not well-mixed, but it simplifies the calculation enough to allow an analytical solution. The solution to the differential equation of diffusion with the initial and boundary conditions listed above is given in Equation (4) [14].

$$\frac{C - C_0}{C_S - C_0} = 1 - \frac{4}{\pi}\sum_{n=0}^{\infty}\frac{(-1)^n}{2n+1}\exp\left[\frac{-(2n+1)^2\pi^2 D}{4l^2}t\right]\cos\frac{(2n+1)\pi x}{2l} \tag{8}$$

Equation (4) can be expressed in terms of fractional release, as shown in Equation (5). At short time-scales (M_t / $M_\infty < 0.60$), the approximation in Equation (6) can be used [13].

$$\frac{M_t}{M_\infty} = 1 - \sum_{n=0}^{\infty} \frac{8}{(2n+1)^2 \pi^2} \exp\left[\frac{-(2n+1)^2 \pi^2 D}{4l^2} t\right] \tag{9}$$

$$\frac{M_t}{M_\infty} = 4\left[\frac{Dt}{\pi l^2}\right]^{\frac{1}{2}} \tag{10}$$

When the M_t / M_∞ data below 0.60 is plotted versus $t^{1/2}$, the diffusion coefficient D for Mechanism 1 is found to be 2.7×10^{-12} cm^2/sec. As shown before, Mechanism 2 shows zero-order release behavior with a diffusion rate of 5.8×10^{-6} mM/sec. Mechanism 1 displays some concentration dependence, which is probably because it represents eosin that was dissolved in the bulk fluid of the hydrogel and diffused out to the surrounding media. The remaining eosin was more strongly bound to the structures, and the slower diffusion in Mechanism 2 likely indicates electrostatic and hydrophobic interactions with the BSA in the material [11,12].

This analysis provides an understanding of the diffusion kinetics of eosin from printed structures, and gives insight into the timescales over which there remains a usable reservoir of photosensitizer for imprinting. Knowledge of these timescales is critical when planning experiments that last several hours or days. The analysis also provides a model for the use of these printed materials as controlled release devices for delivery of bioactive molecules into a cellular microenvironment from the substrate. This opens the door to possible future applications in tissue engineering.

Effects of photosensitizer concentration on imprinting

Since the eosin level in micro-3D printed structures decreases over time, and eosin concentration influences the crosslinking efficiency during a photochemical reaction, it is important to determine whether imprinting effects will remain consistent over the course of a multi-hour experiment. Here I incubated eosin-loaded tile structures in L-15 media at 37°C to mimic the cell culture conditions discussed in Chapter 4. At several time points over the course of 24 hours, I recorded the concentration of eosin in the tiles and scanned the tiles to observe imprinting effects at these eosin concentrations.

Each tile was imprinted over its entire area by scanning twice from a scan height of 12 µm. The concentration of eosin in each tile was measured immediately before imprinting. The post-imprinting height was measured from each tile and subtracted from the 10.5 µm average height of unimprinted tiles. Finally, a regression analysis was performed to test whether there was any correlation between concentration and change in height from imprinting during the first 24 hours of incubation. The results of the analysis are shown in Figure 3.11.

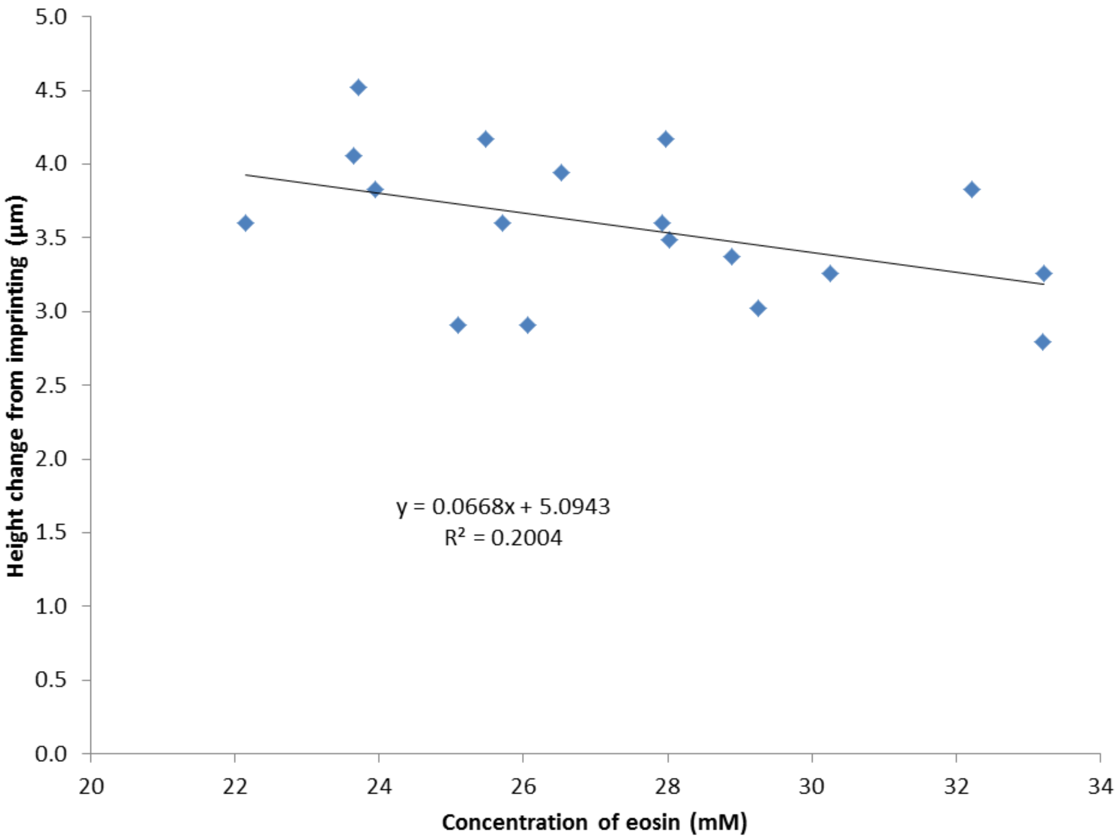

Figure 3.11: A linear regression plot of the concentration of eosin in tiles structures versus height change caused by imprinting. Number of measurements (n) is 18.

Linear regression showed that the slope of the regression line (β_1) was 0.0668 µm/mM, suggesting a correlation between height change and eosin concentration. A higher concentration correlates with a smaller height change, which is counterintuitive to the proposition that higher concentrations of eosin lead to stronger imprinting. However, there is a high variance to the data, as indicated by the small R^2 value of 0.2. The large residual sum-of-squares (Res SS = 3.33) compared with the small regression sum-of-squares (Reg SS = 0.83) shows that the data is a poor fit to the regression line, and the correlation should be viewed with skepticism.

A t-test for simple linear regression can be applied to the data to test the significant of the correlation. The null hypothesis H_0: $\beta_1 = 0$ proposes that there is no relationship between the concentration and imprinted height change. The t-statistic for the data was found to be 2.00 and the resulting p-value was 0.06, just above the 0.05 threshold that is used to consider a relationship statistically significant. The hypothesis cannot be rejected and the possibility exists that there is no relationship between eosin concentration and height change. It would be more informative to speak in terms of confidence intervals. The data suggests that one can be 95% confident that the slope β_1 falls between -0.0039 and 0.1376, and conclude that there is little to no significant association between concentration and height change within the first 24 hours after loading structures with eosin.

3.4 CONCLUSIONS

The studies presented in this chapter contribute toward a feasible method to imprint topographical features to the surfaces of protein hydrogels. By varying the number of scans and scan heights of a laser voxel through a tile structure, topographical features with height differences of over 3 μm can be introduced. Although the photosensitizer eosin can diffuse out of the structures, the change in concentration over the first 24 hours after loading with eosin does not significantly affect the imprinting depth.

Certain improvements can be made to the system to increase its versatility. The diffusion of photosensitizer from the structures can be prevented by covalently conjugating the photosensitizer to the protein material. The surface of the material can be functionalized through the photochemical conjugation of bioactive molecules. The stiffness of the material can be varied by changing the composition of the printing reagent solution and the printing laser parameters.

Moreover, this technique allows precise control over the specific time and location at which imprinting is performed. When coupled with the imprinting technology, the printed material functions as a photoresponsive hydrogel surface that is capable of undergoing dynamic topographical changes. Such a surface can be used for a tremendous range of applications, particularly for the study of topographical guidance in cell cultures. New topographical cues can be presented to cells at any point in their history by imprinting the substrate they grow on. Potential areas for study include the polarization and alignment of cells to grooves and the differentiation of stem cells, as well as cell migration and pathfinding behaviors. Alignment of cells to grooves is discussed in Chapter 4.

3.5 REFERENCES

1. Buddy D. Ratner, Allan S. Hoffman. Synthetic Hydrogels for Biomedical Applications. Hydrogels for Medical and Related Applications [Internet]. American Chemical Society; 1976 [cited 2014 Jul 6]. p. 1–36. Available from: http://dx.doi.org/10.1021/bk-1976-0031.ch001

2. Tomatsu I, Peng K, Kros A. Photoresponsive hydrogels for biomedical applications. Adv Drug Deliv Rev. 2011 Nov;63(14–15):1257–66.

3. Qiu Y, Park K. Environment-sensitive hydrogels for drug delivery. Adv Drug Deliv Rev. 2001 Dec 31;53(3):321–39.

4. Schindelin J, Arganda-Carreras I, Frise E, Kaynig V, Longair M, Pietzsch T, et al. Fiji: an open-source platform for biological-image analysis. Nat Methods. 2012 Jul;9(7):676–82.

5. Pitts JD, Campagnola PJ, Epling GA, Goodman SL. Submicron Multiphoton Free-Form Fabrication of Proteins and Polymers: Studies of Reaction Efficiencies and Applications in Sustained Release. Macromolecules. 2000 Feb 5;33(5):1514–23.

6. Basu S, Campagnola PJ. Properties of crosslinked protein matrices for tissue engineering applications synthesized by multiphoton excitation. J Biomed Mater Res A. 2004 Nov 1;71(2):359–68.

7. Allen R, Nielson R, Wise DD, Shear JB. Catalytic Three-Dimensional Protein Architectures. Anal Chem. 2005 Jul 15;77(16):5089–95.

8. Kaehr B, Shear JB. Multiphoton fabrication of chemically responsive protein hydrogels for microactuation. Proc Natl Acad Sci. 2008 Jul 1;105(26):8850–4.

9. Jonker AM, Löwik DWPM, van Hest JCM. Peptide- and Protein-Based Hydrogels. Chem Mater. 2012 Mar 13;24(5):759–73.

10. Harris DC. Quantitative Chemical Analysis. Eighth Edition edition. New York: W. H. Freeman; 2010. 750 p.

11. Abuin E, Aspée A, Lissi E, León L. Binding of Rose Bengal to Bovine Serum Albumin. J Chil Chem Soc. 2007 Jun;52(2):1196–7.

12. Birla L, Cristian A-M, Hillebrand M. Absorption and steady state fluorescence study of interaction between eosin and bovine serum albumin. Spectrochim Acta A Mol Biomol Spectrosc. 2004 Feb;60(3):551–6.

13. Ritger PL, Peppas NA. A simple equation for description of solute release I. Fickian and non-fickian release from non-swellable devices in the form of slabs, spheres, cylinders or discs. J Controlled Release. 1987 Jun;5(1):23–36.

14. Crank J. The Mathematics of Diffusion. Clarendon Press; 1956. 364 p.

Chapter 4: Cellular response to dynamic topographical changes induced by micro-3D-imprinting

4.1 INTRODUCTION

Chapter 1 discussed how subjecting cells to various environmental cues can uncover important information about their behavior. In particular, dynamic cellular microenvironments are used in attempts to replicate the complex spatio-temporal milieu that cells experience *in vivo*. An important field of research is the development of dynamic two-dimensional cell substrates, which reveal how cells respond when the surfaces they grow on undergo changes. These can be changes in topographical features or mechanical stiffness, or the introduction or removal of chemical cues.

In recent years, there have been many interesting developments in creating dynamic substrates. The most versatile methods use an external trigger to induce changes at specific time points, allowing observation of how cells respond to such changes at specific points in their life-cycle. The triggers can be in the form of chemical reactions, electrical stimulation, mechanical deformation, temperature changes, or light exposure. Recent developments in click-chemistry techniques permit the non-toxic, and nearly instantaneous, chemical functionalization of surfaces with bioactive molecules such as Arg-Gly-Asp (RGD). This enables researchers to control cell adhesion dynamically on demand [1]. Electroresponsive materials can be used to trigger cell detachment by using an electric current, delivered through gold electrodes, to desorb a self-assembled monolayer of cell antibodies [2]. Mechanoresponsive materials have been used to increase adhesivity by exposing RGD-containing peptides upon stretching [3], detach biofilms by destabilizing surface topographies through electrical stimulation [4], and align cells by magnetically-induced wrinkling of the substrate [5]. Thermoresponsive smart polymers have been used to align cells to parallel grooves [6–8] and differentiate stem cells [9]. Photoresponsive materials have been used for the controlled detachment of cells from substrates through multiphoton photodegradation of hydrogels [10].

Three of the studies cited above use thermoresponsive shape-memory polymers, such as polycaprolactone, to change cell morphology [6–8]. There is a great diversity in groove dimensions used in these experiments, from 5 μm trough width and 0.3 μm depth [6] to 100 μm width and 15 μm width [7]. The substrates transitioned from grooved to flat substrates over 1-2 hours in some cases [6,8], and over 19 hours in others [7]. The cell types used were mouse embryonic fibroblasts and human mesenchymal stem cells, both of which exhibit a detectable response to substrate topographies. The cells took 12-30 hours to fully change from aligned to stellate morphologies. Although these surfaces succeed in altering the topography of cell substrates dynamically, they display certain shortcomings. Thermoresponsivity, by definition, requires the substrate to undergo a temperature-induced transition to trigger the topography change. Consequently, the cells growing on the substrate often spend long periods of time at temperatures that were not optimal for cell culture. Furthermore, the topography changes took place over the course of hours, which is much slower than the time course of extracellular matrix remodeling in the body [11]. In addition, the thermoresponsive substrates are produced by casting a polymer material, such as polycaprolactone, into premade molds. Thus, each time a substrate pattern requires modification, a new mold has to be manufactured. Because of this, features cannot be made in response to cell morphology and orientation, which is unknown at the outset of an experiment. It also adds a long turn-around time into the experimental cycle, and dimensional parameters cannot be modified on-the-fly.

The imprinting technique developed in Chapter 3 has many advantages over thermoresponsive methods. Photoresponsive protein hydrogels can be imprinted with well-defined patterns using a laser raster scan and a digital mask, thereby avoiding temperature conditions that could disrupt cell cultures. New imprinting patterns can be generated in a matter of minutes, resulting in a short experimental cycle. Moreover, the protein hydrogel material is soft and has high water content, making it a better substitute for the extracellular matrix than a material like polycaprolactone.

With these advantages, this imprinting technique is a highly attractive tool for introducing dynamic topographical changes to a cell substrate with minimal disturbance of the cell culture. It facilitates *in vitro* studies that endeavor to mimic the *in vivo* topographical changes that arise through extracellular matrix remodeling.

In this chapter I present a novel approach for invoking dynamic topographical responses in cultured cells. A large micro-3D printed pad is used as a substrate for cell culture. Once cells have adhered and spread on this flat substrate, grooves are imprinted on the surface. The cellular response to this change in topography is observed and analyzed.

4.2 METHODS

Micro 3D-printing a substrate for cell culture

Low-gelatin reagent solution was prepared by dissolving 300 mg of BSA and 100 mg of gelatin in 1 mL of 15 mM rose bengal. This solution was melted and mixed at a temperature of 60°C, then applied by transfer pipette to an ink-marked glass-bottom well (Mattek, Ashland, MA). When the solution cooled to a gel, a small amount of water was applied to keep it hydrated while printing.

The printing of material proceeded as described in the methods section of Chapter 3. The glass-bottom well was placed on the stage of the inverted microscope of the micro-3D-printing rig. The average laser power used for printing was 35 mW at the objective back aperture, and the beam was focused through a 60X objective (Plan Apo, Nikon Instruments, Melville, NY), and raster-scanned at a velocity of 68,000 µm/s in the fast axis and 25 µm/s in the slow axis. A mask was projected on the digital micromirror device (DMD) to produce a tile of desired shape. In most experiments, the mask produced a square "tile". In a few experiments, a "shell"-shaped mask was used. The voxel was translated to a height H_0 = 10 µm above the glass surface, and then stepped downward one micrometer at a time. The laser beam was scanned through the printing area once per step until the printed structure was anchored to the glass surface. The nominal size of the printed tile structure was 70 µm (x) by 70 µm (y) in area, and 10 µm in height. After the tile was printed, the sample was translated manually in the x and y dimensions, and more tiles were printed so that an extended pad of material measuring at least 500 µm by 400 µm was printed. Adjacent tiles were overlapped by up to 10 µm to produce a continuous pad without gaps that exposed the underlying glass. However, the seams between pads were not topographically flat. They manifested as single grooves of ~1 µm depth, and had the potential to act as topographical guidance cues for cells. To decouple the topographical influence of imprinted grooves from these seams, attempts were made to orient the grooves in directions that did not coincide with the orientations of these seams. The shell-shaped tiles was one such attempt (shown in Figure 4.6). The most successful strategy was to orient the grooves at 45° to tile seams, and this was used for most experiments.

The pad was rinsed in 50% ethanol to extract residual rose bengal, which is cytotoxic, and then reloaded in 5 mM eosin.

Construction of temperature-controlled imaging chamber

As cell cultures grow optimally at physiological temperatures, a temperature-controlled chamber was constructed in-house to enclose the microscope stage (TE 2000, Nikon Instruments, Melville, NY) for long-term cell observation. The chamber was constructed out of 6.3 mm plexiglass with dimensions 28 cm by 18.5 cm by 10 cm. A window was cut into the chamber roof and fitted with an optical flat for illumination from the microscope condenser. A heating element and fan unit were extracted from a dismantled heat gun (Westward 4FWK1; W. W. Grainger, Lake Forest, IL) and used to direct warmed air through 3.8 cm diameter polyethylene tubing (Pool and Spa Hose, Home Depot, Austin TX) into the chamber through a port at the chamber front. A similar length of tubing carried air from the rear of the chamber back to the heating element housing. The tubing and the floor of the chamber were insulated with pipe insulation tape (Armaflex, Armacell, Mebane, NC). A thermocouple located at the heated-air entry port delivered temperature information to a proportional-integral-derivative (PID) controller (E5GN, Omron, Hoffman Estates, IL) which switched the heating element on or off to maintain a 37±1 °C temperature within the chamber.

Cell culture

NIH3T3 fibroblast cells were obtained as frozen samples, the first as a much-appreciated gift from the lab of Dr. Stanislav Emilianov, and the second from ATCC (CRL-1658 , Mannasas, VA). Cells from both sources were used between passage 7 and passage 20 after the cells were thawed. Cells were grown in complete media consisting of Dulbecco’s Modified Eagle’s Medium (DMEM; High glucose, with L-glutamine and sodium pyruvate; Hyclone, Thermo Fisher Scientific, Waltham, MA) with 10% bovine calf serum (Hyclone, Thermo Fisher Scientific, Waltham, MA). For observation under a microscope, the cells were plated in plating media, comprised of Leibovitz’s L-15 medium (Hyclone, Thermo Fisher Scientific, Waltham, MA) with 1% bovine calf serum and 1% penicillin-streptomycin (GIBCO, Grand Island, NY). If cells were being plated on a printed pad, they were deposited at a high density in a small volume (~150 μL) of plating media and incubated at 37°C in the microscope imaging chamber for 2-4 hours until the cells adhered to the pad. This small volume was necessary to minimize fluid movement that caused the cells to drift off the pad before they adhered. Vacuum grease was used to seal the well lid to the dish to minimize evaporation.

Cell adhesion was monitored visually through a 10X objective (Plan Apo, Nikon Instruments, Melville, NY) until approximately 50 cells adhered over a 500 μm by 400 μm area. Then the well was filled with plating media and the un-adhered excess cells drifted off the pad, leaving cells plated at a density of ~5,000 cells/cm^2. Imaging was performed using illumination through a far-red longpass filter, which minimized photosensitizer excitation.

Imprinting grooves into substrate

The printing of material proceeded as described in the methods section of Chapter 3. For the imprinting of control grooves, the glass-bottom wells containing the printed pads were emptied of the eosin loading solution and filled with Phosphate buffered saline (PBS; GIBCO, Grand Island, NY). Eosin was used as a biocompatible photosensitizer. The well was placed on the stage of the micro-3D-printing instrument, and the voxel was focused through a 60X objective (Plan Apo, Nikon Instruments, Melville, NY) on the glass surface at the bottom of the printed tile. A mask was selected in a pattern that imprinted long parallel grooves into the pad. Three variations of groove patterns were imprinted: 3 μm ridges and 4 μm troughs with a 7 μm pitch [3+4], 5 μm ridges and 10 μm troughs with 15 μm pitch [5+10], and 5 μm ridges and 15 μm troughs with 20 μm pitch [5+15] (see Figure 4.1).

The voxel was moved to a height H_0 above the glass surface, then stepped down one micrometer at a time until the voxel was well within the glass. Each plane was raster scanned with the laser through the imprinting mask, with a fast axis velocity of 68,000 μm/s and slow axis velocity of 25 μm/s. For imprinting done using multiple scans, the voxel was again returned to height H_0 and the procedure was repeated one or more times as indicated. Each structure was stored in PBS until further use to maintain hydration.

For the imprinting of dynamic grooves, a similar procedure was followed with the following differences. The well was plated with cells in plating media. Once the cells adhered and spread on the substrate in a stellate morphology, approximately 4 hours after plating, imprinting was performed as described above. Then, the cells were observed over 24 hours and timelapse images were captured at 5 min intervals.

Cell toxicity assessment

A cell viability test was performed to examine whether NIH3T3 cells could withstand exposure to a scanned laser beam. Cells in plating media were seeded on an ink-marked, 8-well chambered coverglass (Nunc® Lab-Tek®, Sigma Aldrich, St. Louis, MO). After incubating for one day at 37°C in a humidity-controlled incubator (at atmospheric air composition), the wells were placed on the stage of the printing rig. A laser beam with average power of at 35 mW at the objective back aperture was focused through a 60X objective and raster scanned through the cells three times over an area of 700 μm by 300 μm. The cells were incubated for another 8 hours, then stained with calcein AM and ethidium homodimer (Molecular Probes, Eugene, OR). Fluorescent images were taken via tetramethylrhodamine isothiocyanate (TRITC) and fluorescein isothiocyanate (FITC) filter sets to identify living and dead cells.

Measuring depth of imprinted grooves

A set of tiles was printed according to the standard protocol. Grooves were imprinting using a mask that produced grooves of styles [3+4], [5+10], and [5+15]. Scan heights were 8 µm, 10 µm, 12 µm, and 14 µm. Negative-space confocal imaging was used to measure the dimensions of these grooves. Here, the region around the imprinted tiles was flooded with a highly concentrated fluorescent dye, and the space occupied by the printed tile was distinguished by its much lower fluorescence signal. The fluorescent dye was a 35-40 mg/mL solution of fluorescein isothiocyanate conjugated to a 2 MDa molecular weight dextran molecule (FITC-dextran; FD2000, Sigma Aldrich, St. Louis, MO). It had an excitation wavelength maximum at 490 nm and maximum emission at 520 nm. The large tethered dextran molecules prevented the fluorescein from penetrating the printed tiles, thus providing a high fluorescence signal contrast between the tiles and the surrounding region. These were imaged using a confocal microscope (SP2 AOBS; Leica Microsystems, Buffalo Grove, IL) using a 63X (HCX APO, 1.4NA) oil objective. The samples were excited with a 488 nm Argon laser. Emitted light was collected in the range 496nm - 675nm. Higher wavelengths were excluded to avoid collecting light emitted from eosin in the structures. Photomultiplier tube (PMT) gain was set to 480 V to maximize contrast between the structures and the FITC-dextran dye. The pinhole size was 20.0 µm (0.17 airy disks), and the laser scan rate was 400 Hz. Voxel dimensions were 465 nm (x) × 465 nm (y) × 115 nm (z). Images were captured in the form of stack files.

Orthogonal projections of the images were computed using the imaging software FIJI [12], and the structure heights at the plateaus and troughs were obtained from pixel measurements. The groove depths were calculated by taking the difference in height between plateaus and troughs.

Quantifying cell alignment to grooves

Timelapse images of cells were captured every 5 minutes over 24 hours with an inverted microscope in brightfield mode using a scientific charge-coupled device (CCD) camera (CoolSNAP fx, Photometrics, Tuscon, AZ). A shutter (VS25, Uniblitz, Rochester, NY) was used to limit illumination to 200 ms every 5 minutes while each image was taken. From the full ~289 frames of images, 11-14 frames were extracted for analysis of each experimental run.

Although imprinting a single 70 µm by 70 µm area takes only two minutes, coverage of the entire experimental area can take up to 2 hours. For each dynamic imprinting sample, the midpoint of the imprinting time was calculated and ascribed the time-point t = 0. For each control surface, including pre-imprinted grooves (positive control) and unimprinted flat surfaces (negative controls), the time-point t = 0 was ascribed to the time when cells began to adhere to the pad. For each experimental category and positive control, 4 or 5 cells on each of 3 samples were selected and tracked from the beginning to the end of the experiment. For the negative control, 12 cells were tracked. Each cell was measured from leading edge to trailing edge, and the angle it made with respect to the direction of the grooves was recorded from -90° to 90°, with 0° indicating that the cell was parallel to the grooves. In the case of the negative control, an arbitrary direction was selected to compare cell angles against. The cell alignment angles were plotted versus time.

Imaging of actin cytoskeleton

The actin filaments comprising the cytoskeletons of cells were imaged by staining with Alexa 488-phalloidin. After cells were cultured in a glass-bottom well, the media was gently removed with a transfer pipette. The cells were fixed in a 3.4% solution of formaldehyde (Macron Fine Chemicals, Center Valley, PA) in Cytoskeleton Buffer [13] for 20 min. Next, the cell membranes were permeabilized by replacing the formaldehyde solution with a 0.5% solution of Triton X-100 (Sigma, St. Louis, MO) in PBS, and incubating on ice for 10 min. The permeabilizing solution was removed and the cells gently rinsed. Non-specific binding sites in the cell were blocked by incubating the cells in antibody diluting solution (Abdil) [13] for 10 min. Then, the cells were incubated in an actin-staining solution of Alexa Fluor® 488 Phalloidin (Molecular Probes, Eugene, OR) for 20 min. After rinsing in PBS, they were incubated in a 5 μg/mL solution of 4',6-diamidino-2-phenylindole (DAPI; Molecular Probes, Eugene, OR). Finally, the DAPI solution was rinsed away, and the cells were kept in PBS for a few hours until imaging.

Cells were imaged using a confocal microscope (SP2 AOBS; Leica Microsystems, Buffalo Grove, IL) using a 63X (HCX APO, 1.4NA) oil objective. The samples were excited with 405 nm and 488 nm argon lasers. Emitted light was collected in the ranges 409 nm – 483 nm (for DAPI), 494 nm – 515 nm (for Alexa Fluor® 488), and 616 nm – 834 nm (for eosin), via three PMT channels. A fourth channel collected transmitted light. PMT gain was set to 680 V, 504 V, 512 V, and 192 V for each channel respectively. The pinhole size was 114.6 μm (1.00 airy disks), and the laser scan rate was 400 Hz. Voxel dimensions were 465 nm × 465 nm × 115 nm. Images were captured in the form of z-stack files.

Stack slices from the top to the bottom of the cells were extracted into a substack, to isolate fluorescence images of actin from extraneous signals in other slices. A zprojection was taken of these images using the sum algorithm in FIJI [12], and the brightness and contrast of the final image was adjusted for maximum clarity of the actin filaments.

4.3 RESULTS AND DISCUSSION

The purpose of this work was to develop a method for delivering dynamic topographical cues to cells and observe changes in their behavior. Particular effort was made to minimize other perturbations to the cells, such as temperature fluctuations and photo-damage. This goal was pursued by first preparing a large cell culture substrate through micro-3D printing. Mouse embryonic fibroblast (NIH3T3) cells were plated on this substrate, letting them adhere and flatten into a stellate morphology. Once the cells were established on the substrate, the substrate was imprinted with a pattern of parallel grooves. The cells responded to these new topographical cues by changing their shape from stellate to bipolar, and aligning parallel to the grooves.

Individual fibroblast cells are generally 10-50 µm in size and migrate over areas several times larger than the cell size over the course of a day. A single printed tile of 70 µm by 70 µm would be too small to accommodate and observe these cells. Therefore, a large pad was built by printing several tiles together over a large area, at least 500 µm by 400 µm. The edges of the tiles were slightly overlapped to form a continuous material. The mask for the printed tile is shown in Figure 4.1 (a).

On these large pads, approximately half the area was imprinted with grooves before any cells were plated, using masks of the style shown in Figure 4.1 (b) and (c). These grooves served as a positive control, to confirm that static topographical cues could induce bipolar morphologies in cells that are plated on them. On the other half area of the pads, grooves were imprinted after cells were plated, adhered, and spread on the flat surface. These grooves presented dynamic topographical cues to the cells. Both control and dynamic grooves were oriented at 45° from the seams of the tiles that comprised the pads. This was to ensure that any topographical influence of the seams could be distinguished from the influence of the grooves. Each set of grooves was defined by the groove widths (the widths of ridges and troughs respectively) and the scan height used for imprinting grooves to a particular depth. Figure 4.1 shows a schematic of an imprinted pad with these dimensions indicated.

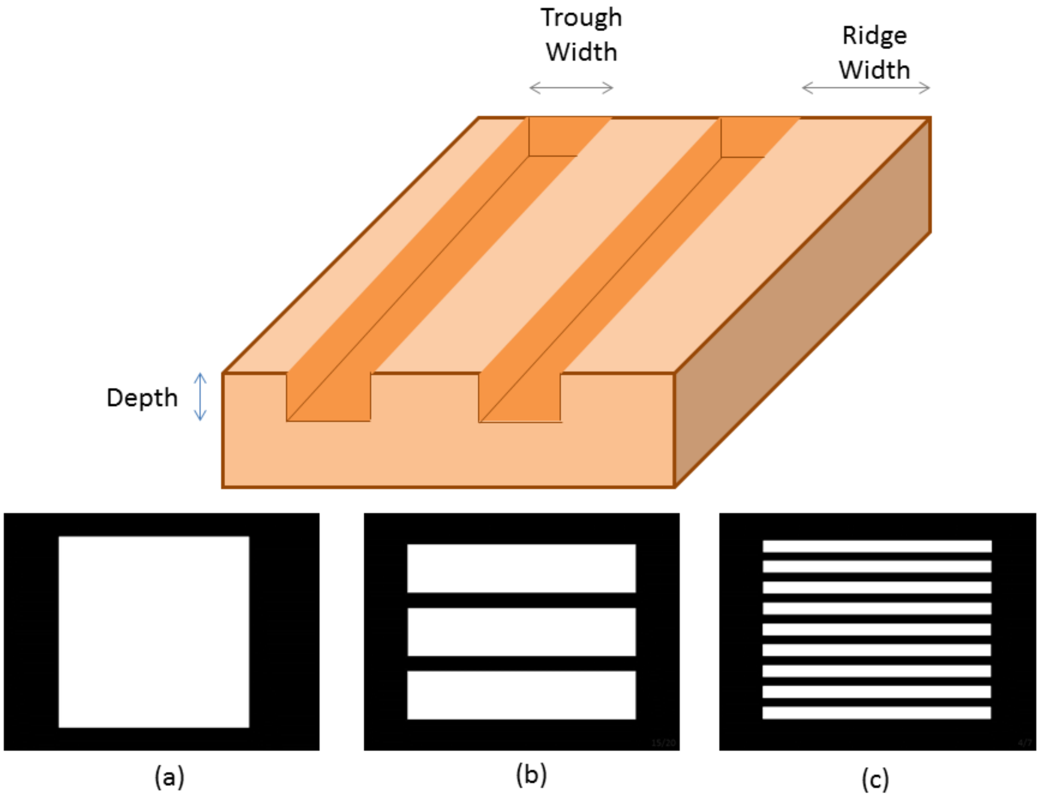

(a) (b) (c)

Figure 4.1: Schematic of imprinted pad and masks. Diagram (top) indicates trough width, ridge width, and depth of grooves. Masks projected on the DMD (bottom) are used to print 70 µm by 70 µm tiles (a), [5+15] grooves (b), and [3+4] grooves (c).

Since dynamic grooves were produced by scanning the cell substrate with a high-peak-power laser, it was important to select experimental conditions to minimize cell damage. The replacement of rose bengal with eosin was intended to minimize cytotoxicity by using a more cell-compatible photosensitizer. At one point, the addition of eosin to the cell culture media was considered as a means to prevent the diffusion of photosensitizers from the cell substrate. However, eosin concentrations high enough to eliminate diffusion were toxic to cells and this option was rejected. Efforts were also made to imprint with a laser scan height that avoided exposing cells to the laser voxel.

Viability of cells after laser exposure

Phototoxicity, or damage to cells caused by exposure to light energy, is a well-recorded phenomenon. In fact, it is the basis for photodynamic therapy [14], a treatment for a range of pathologies including cancer. Photodynamic therapy involves localizing photosensitizers to living cells and exciting them with light of appropriate wavelengths in the presence of oxygen. The formation of reactive oxygen species causes injury to proximal cells, eventually leading to cell death. Since the imprinting process brings living cells, photosensitizers, and high levels of light energy in close proximity, it is necessary to consider the possibility that cells may be damaged by the imprinting process.

However, in the experiments performed in this chapter, significant levels of cell death were not observed when the cell substrate was scanned. Few cells in an experiment, if any, proceeded to undergo apoptosis or necrosis in the ~20 hours following scanning. For a quantitative assessment of cell survival after scanning, cells plated on glass were scanned three times with the laser voxel focused on the plane of cell adhesion, and a fluorescence assay for cell viability was performed. This assay could not be performed on cells plated on printed pads because the eosin loaded in the pads fluoresced strongly over wavelengths emitted by commonly available viability assay dyes. However, other experimental conditions were kept similar to those in imprinting experiments. 8 hours after scanning, the cell count was 94% ± 1pp of its pre-scanned value. The cells were next stained with calcein AM (an indicator of intracellular esterase activity) and ethidium dimers (a nucleic acid stain indicating permeable cell membranes). As Figure 4.2 shows, the majority of cells remained vital after scanning.

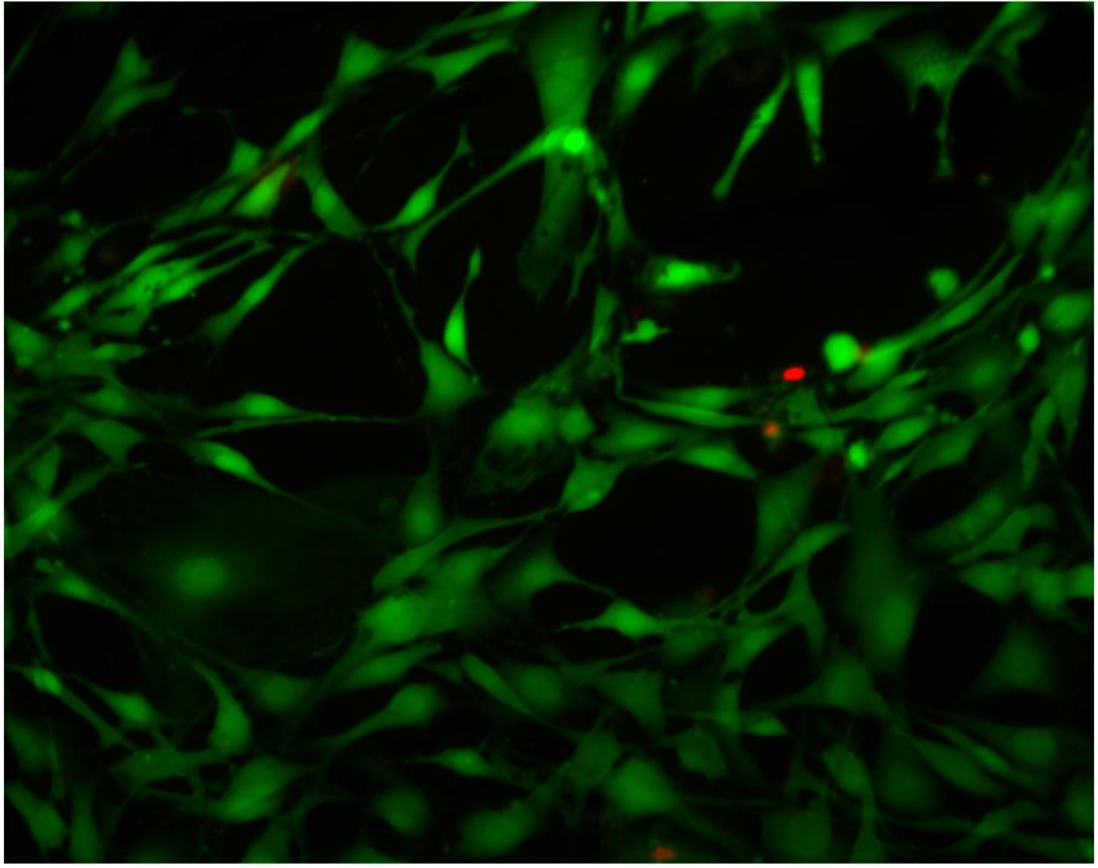

Figure 4.2: Viability assay of laser-scanned cells. After scanning with a laser, most cells remain viable. Green indicates intracellular esterase activity (live cells) and red indicates a damaged cell membrane (dead cells).

Cells plated on eosin-loaded pads also demonstrated similar cell-counts after scanning with a laser. Although viability assays using fluorescent dyes could not be performed on cells plated on pads, brightfield microscopy observations showed that scanned cells continued to migrate and demonstrate other behaviors of healthy cells. This implies that damaged caused to these cells by laser-scanning was minimal.

The absence of major cell damage is surprising, but can be explained by a number of factors. Firstly, although cells were growing on pads that were loaded with photosensitizer, the eosin was not taken up by the cells. This places the cells at a distance (tens to hundreds of nanometers) from the excited photosensitizers. Reactive oxygen species have to diffuse out of the 3D-printed protein hydrogel before they can damage cells, and in the process they can be quenched by the amino acids in the hydrogel or by vitamins in the cell culture media. It appears that reactive oxygen species do not diffuse to the cells in large enough amounts to cause major damage.

Imprinting grooves of desired dimensions

The literature on topographical response shows many instances of cells, particularly fibroblasts, aligning parallel to grooves when plated on a grooved substrate [15]. Such grooves can be imprinted on printed protein hydrogel by scanning the material with a laser as detailed in Chapter 3. The widths of groove ridges and trenches are controlled by designing masks that are projected on the DMD chip, as shown in Figure 4.1 (a-c). White areas of the mask reflect the scanned laser beam and imprint the corresponding area on the printed material. Black areas deflect the beam and leave the corresponding area on the material unimprinted.

The depths of grooves are controlled by varying the scan height and number of scans, two parameters whose effects on tile heights were summarized in Figures 3.5 and 3.6. The effects of scan parameters on groove depths were assessed by imprinting 70 μm by 70 μm tiles with grooves measuring 5μm wide at the ridges and 15μm wide at the troughs [5+15]. The number of scans was 2 in all cases. As shown in chapter 3, a single scan would not imprint deeply enough whereas a third scan would not provide any advantage over two scans. The scan height parameter was varied from 8 µm to 14 µm. Confocal images were taken of the space excluded by the tiles by flooding it with fluorescent dye. Orthogonal views of the tiles are shown in Figure 4.3. The groove depth was measured as the difference between heights at the ridge and trough. A bar graph summarizing these measurements is shown in Figure 4.4.

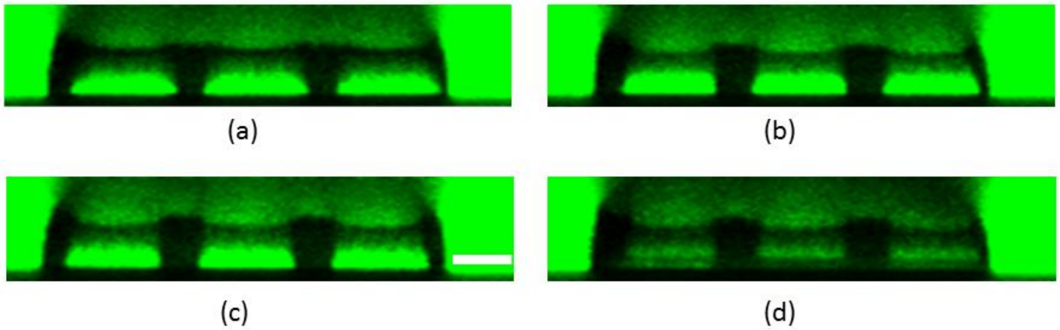

Figure 4.3: Orthogonal view of grooved tiles. Negative space confocal image of tiles imprinted with grooves from scan heights 8 µm (a), 10 µm (b), 12 µm (c) and 14 µm (d). High fluorescence in regions beneath troughs is an artifact of excitation light scattered by imprinted material. Scale bar is 10 µm.

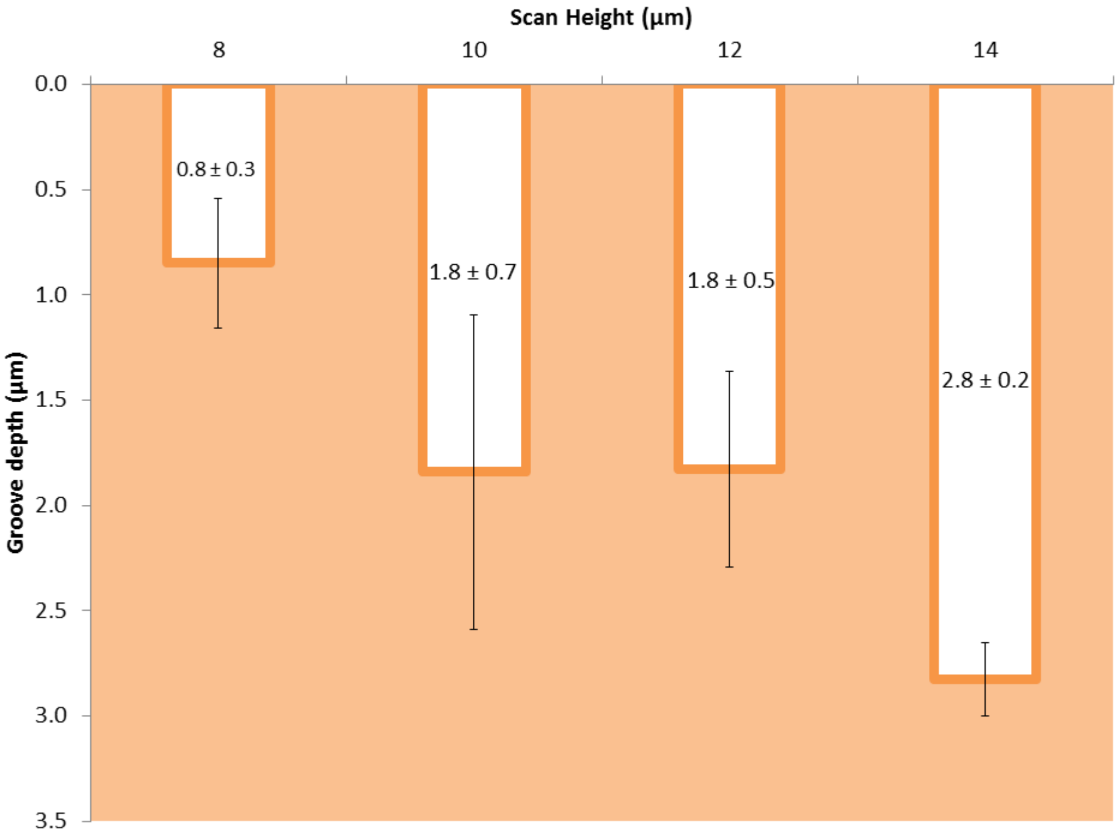

Figure 4.4: Plot of groove depths produced by imprinting [5+15] grooves from various scan heights. Error bars indicate standard deviation. 6 replicates were measured for each scan height.

The height changes produced by the groove mask are much smaller than those produced by the flat square mask, shown in Figure 3.6. When the flat square mask was used, the tile imprinted from a scan height of 8 µm was reduced by ~2µm. Tiles imprinted from 10 µm, 12 µm, and 14 µm were reduced by ~3 µm each. When the grooved mask was used, the heights were reduced by 0.8 µm, 1.8 µm, 1.8 µm, and 2.8 µm respectively.

This disparity is because the printed material has a non-zero shear modulus. The groove mask places imprinted and unimprinted regions in close proximity with each other. When imprinted regions contract and pull toward the underlying glass surface, they experience shear stress from surrounding unimprinted regions. This force opposes the downward motion of the imprinted surface and reduces the overall height reduction of the imprinted region.

It is interesting to note that imprinting from a 14 µm scan height induces a larger height change than imprinting from 10 or 12 µm, even though the nominal height of the tile is 10 µm. This apparent paradox can be explained by considering the elongated shape of the laser voxel, which introduces uncertainty in focusing the laser beam on the glass plane. During printing it can increase tile height by up to a micron. Material swelling can increase height by a further micron. During imprinting, even when the voxel focused 14 µm above the glass plane, the lowest point of the imprinting voxel can overlap with the highest point of the printed pad. Thus the voxel can overlap with the printed material even when positioned 14 µm above the glass plane.

Based on these measurements, a scan height of 12 µm was selected for imprinting grooves. It provides a groove depth of ~2 µm with a small standard deviation. Moreover, compared to a scan height of 14 µm, it reduces the scanning of the laser through cells plated on the pad surface.

Effects of groove widths on cell alignment

Before testing whether cells can align to dynamic grooves, it is necessary to confirm their ability to align to control grooves. The ability of cells to align is closely linked to the dimensions of the grooves on which they are plated, such as the widths of the ridges and the troughs. In this study, cell alignment was tested on grooves of several widths and the effects of three sets of widths are discussed.

Initially, alignment was observed using the NIH3T3 cells obtained from the Emilianov lab on grooves with 3 µm ridge width and 4 µm trough width (designated

[3+4]). The cells aligned readily to control grooves, as seen in Figure 4.5 (a), although they did not align to dynamic grooves. (Here, the grooves were imprinted parallel to seams between pads. At the time of this experiment, attempts had not been made to decouple the topographical influence of imprinted grooves from seams.)

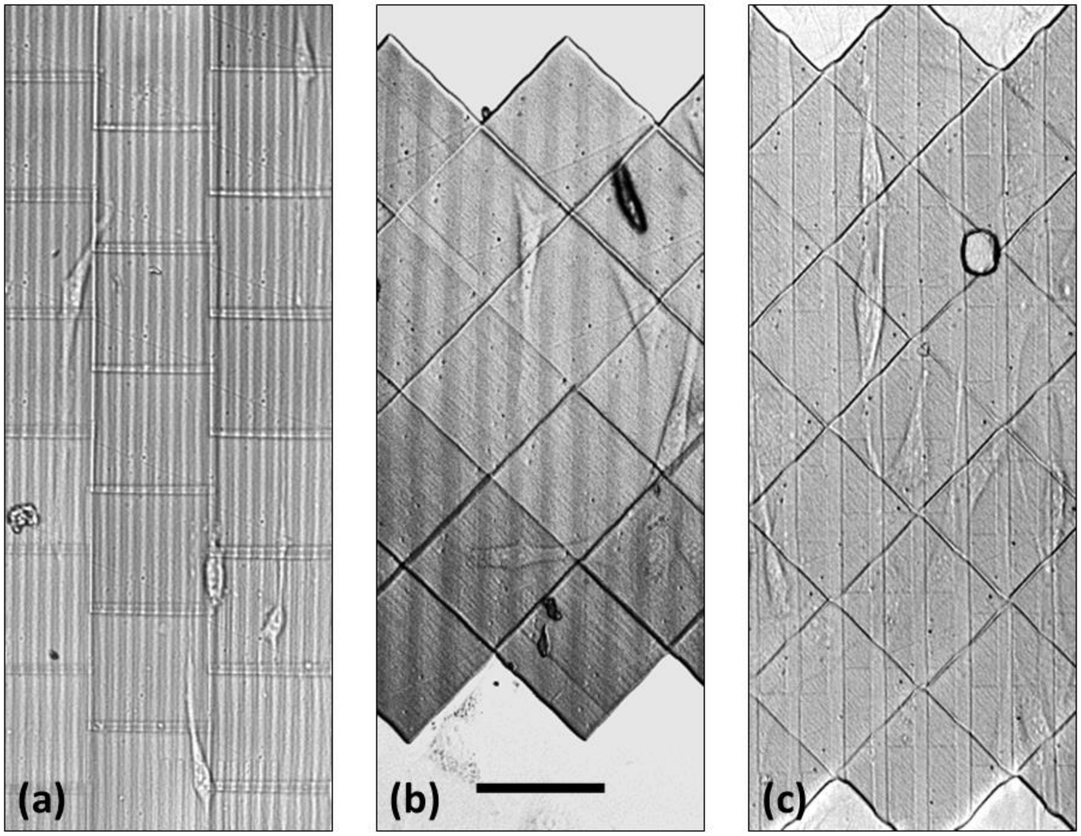

Figure 4.5: Cell alignment on various groove widths. Cells are plated on grooves previously imprinted on micro-3D-printed pads. Groove styles are [3+4] (a), [5+10] (b), and [5+15] (c). Scale bar is 70 um.

In contrast, the NIH3T3 cells obtained from ATCC did not align to control grooves of these dimensions. Although the cells in both batches were ostensibly the same type, the different provenances of the batches suggest that they are likely to have notable phenotype differences, such as varying sensitivity to topographical features of different dimensions. The groove dimensions need to be calibrated for each cell batch to ensure alignment.

Fortunately, the rapid turnaround time for imprinting masks meant that new groove dimensions could be tested quickly. In the first trial, the groove ridges and troughs were both widened to 5 µm (designated [5+5]). A close examination of a cell plated on these grooves revealed an interesting behavior: the leading edge of the cell extended on a ridge and elongated parallel to the grooves. However, the leading edge was wider than the pitch of the grooves and, as it probed the surroundings of the cell, it spanned the adjacent trough and made contact with the next ridge. It then began to spread over the ridges and took on a stellate morphology. The cell's movement is shown in the montage in Figure 4.6. This sequence of events indicates that when a cell can span multiple ridges, it treats the surface as continuous. Widening the groove troughs could prevent the cells' leading edges from spanning multiple ridges, thereby confining them to a single narrow surface on which to extend.

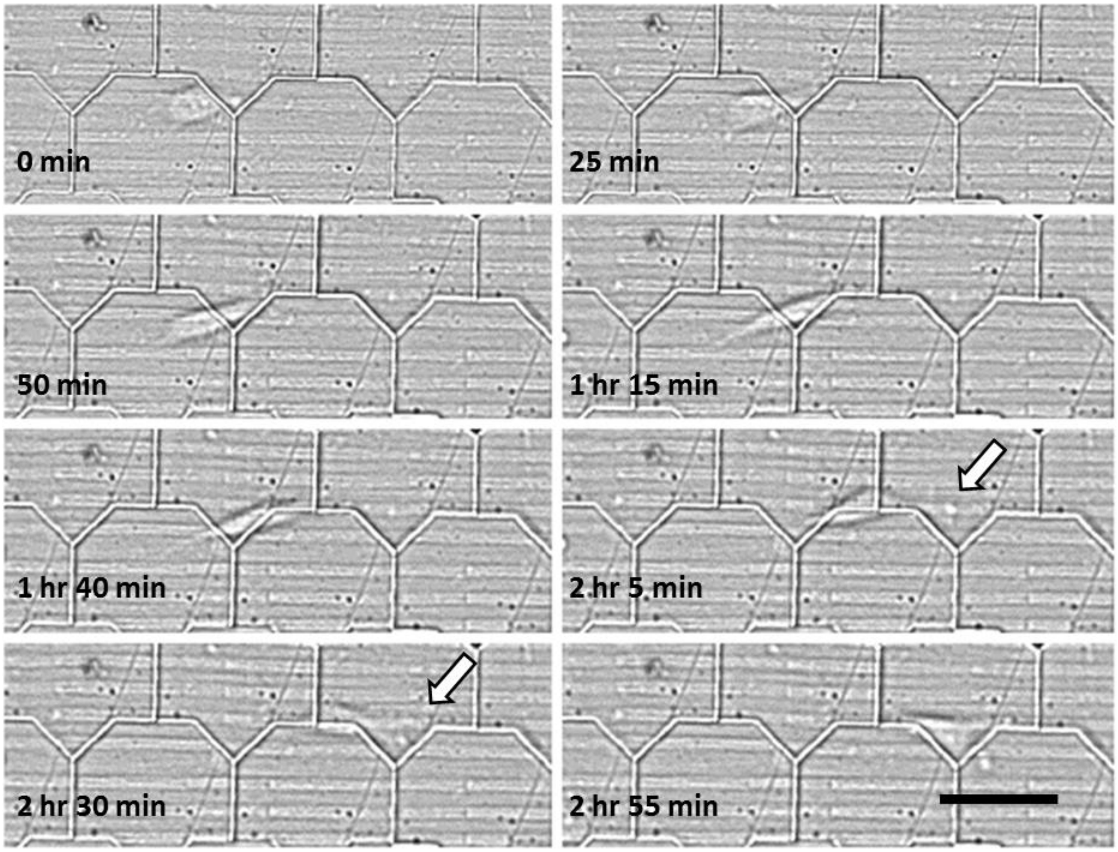

Figure 4.6: A montage of a cell migrating over a grooved surface. The leading edge of the cell probes its surroundings, initially crawling along a ridge and eventually branching across multiple ridges. Groove configuration [5+5], and scan height 12 µm. Scale bar is 50 µm.

To test this theory, troughs were widened to 10 µm (groove configuration [5+10]). In the first trial, cells aligned intermittently (Figure 4.5b). However, when the troughs were widened further to 15 µm (groove configuration [5+15]) the cells distinctly aligned to the grooves (Figure 4.5c). The alignment of cells to control grooves with configurations [5+10] and [5+15] is compared in Figure 4.7 with that of cells that were plated on a flat surface. The angle of alignment is measured between a cell (specifically, a line segment drawn from the leading to trailing edge of the cell) and the grooves on its substrate.

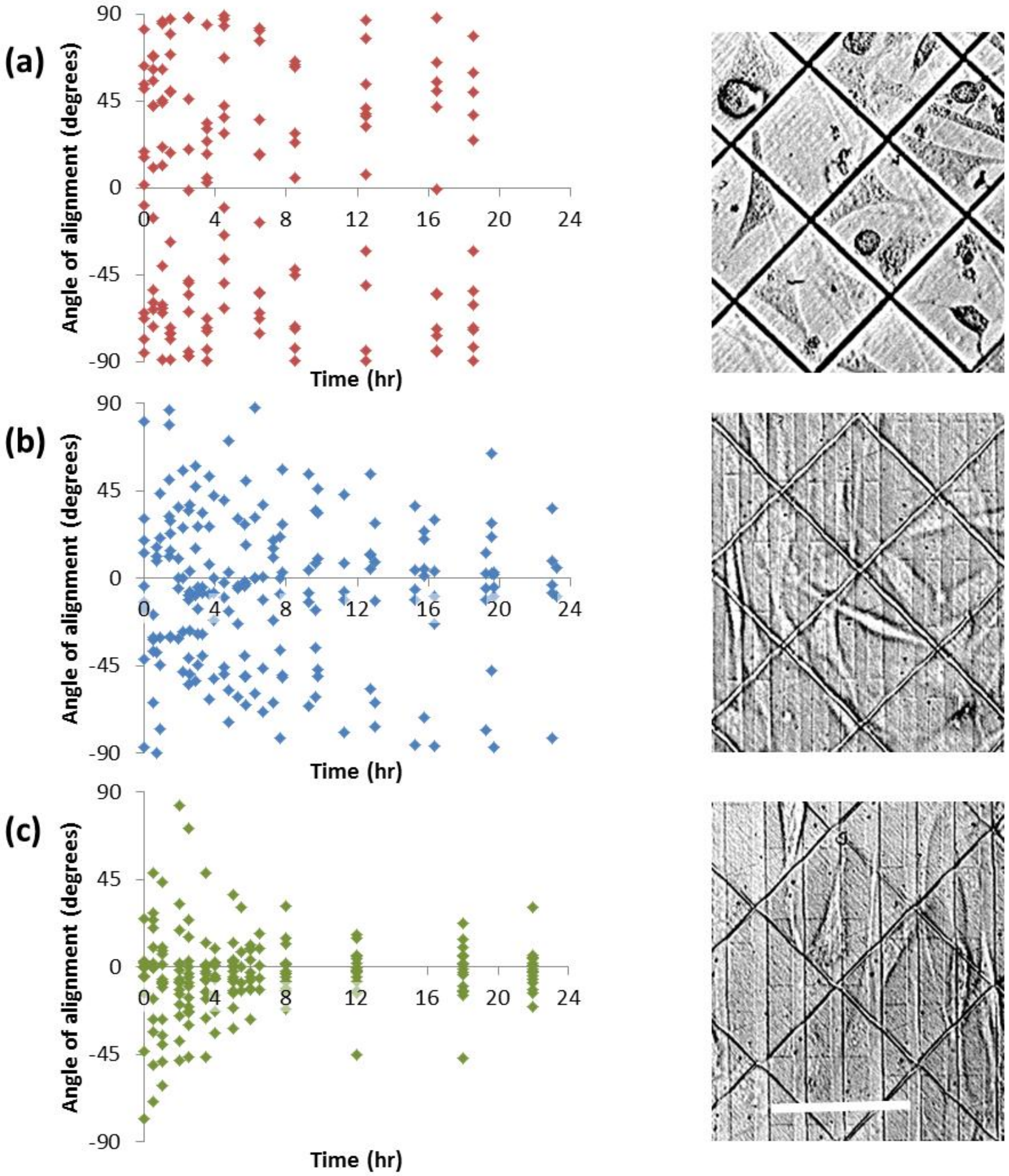

Figure 4.7: The angles of alignment of cells plotted versus time. Cells were plated on 3 types of substrates: unimprinted (a; red), imprinted with [5+10] grooves (b; blue), and imprinted with [5+15] grooves (c; green). Scan height is 12 µm. The brightfield microscope images show examples of cells growing on such substrates. Scale bar is 70 µm.

In Figure 4.7 (a), we see that cells plated on a flat substrate without imprinted grooves tend to orient randomly. In Figure 4.7 (b), plotted angles started to cluster around the 0° mean, indicating that cells plated on [5+10] grooves showed some tendency toward alignment. However, the alignment was far more dramatic on [5+15] grooves. This suggests that 15 μm troughs were wide enough that cells could not easily span them. The cells instead extended in the direction of the grooves. Based on these results, the [5+15] groove configuration was used for testing cell response to dynamic grooves.

Cell alignment to dynamic grooves

In previous sections, it was shown that cells aligned very well to grooves on substrates that were imprinted before cells were plated on them. The optimum groove dimensions were found to be 5 μm ridge width and 15 μm trough width, indicated by [5+15], and 2 μm depth produced by imprinting from a scan height of 12 μm. The next step was to see if cells would align when their flat substrate was dynamically transformed into grooves of these dimensions (i.e. if they would align to dynamic grooves). Printed pads were plated with NIH3T3 cells. Approximately 6 hours after plating, the substrate was imprinted with the grooves described above. Observations over the course of 24 hours showed that cells, initially in a stellate shape with random angular orientations, became bipolar with their long axes oriented parallel to the imprinted grooves. Figure 4.9 shows a montage of cells aligning to control and dynamic grooves over time.

Alignment data from 3 replicates was pooled together and plotted versus time in Figure 4.8. The zero time-point indicates the midpoint of the imprinting process, which was performed section-by-section and took 2 hours to cover the entire experimental area. Negative values (red) indicate time before grooves were imprinted, and positive values (green) indicate time after imprinting.

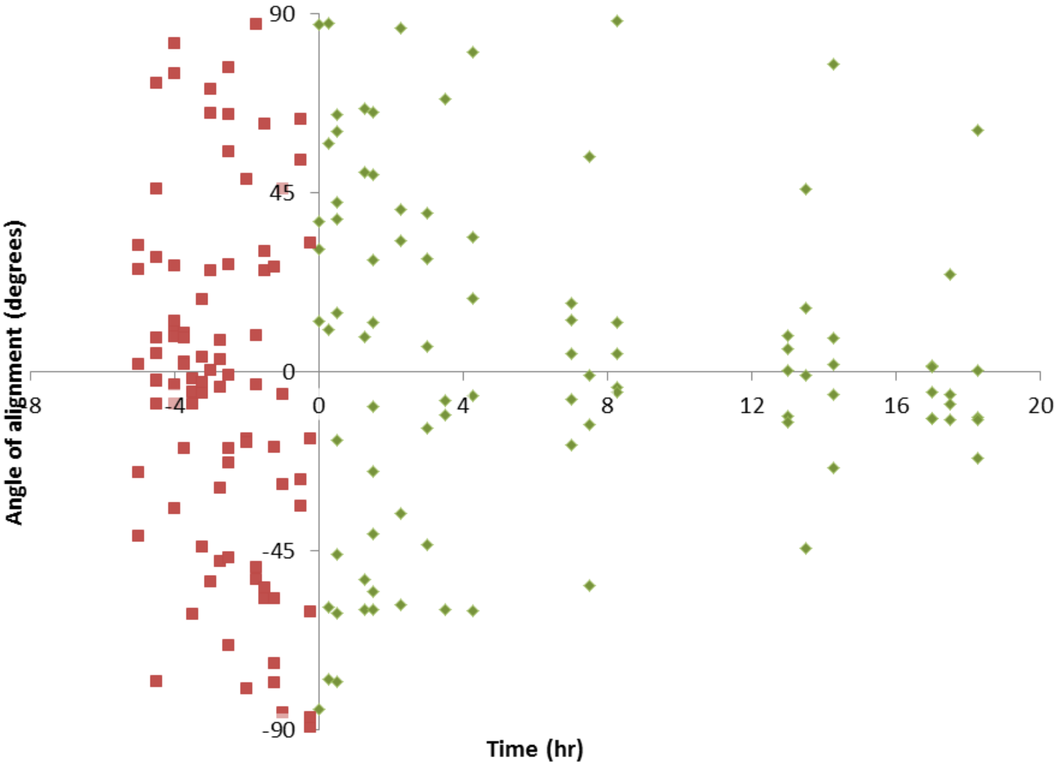

Figure 4.8: A plot of angle of alignment of cells versus time on imprinted grooves. The substrate was imprinted with [5+15] grooves 6 hours after plating. Imprinting took 2 hours with the midpoint occurring at time = 0 hr. Red points indicate measurements taken before the midpoint of imprinting, and green points indicate measurements taken after. Data is compiled from14 cells tracked over 3 experiments.

Comparing the plot with the negative and positive controls plotted in Figure 4.7 (a) and Figure 4.7 (c) respectively, it is clear that cell alignment follows a distribution similar to negative control cells before imprinting. After imprinting, the cells follow the trend demonstrated by the positive control and gradually align to the grooves. By 8 hours after imprinting, 79% of the cells are aligned within ±20° of the grooves. By comparison, on the positive control surface 87% of cells were aligned within ±20° of the grooves. In contrast, on the negative control surface, 8.3% were aligned within ±20° (and 25% were aligned within ±30°).

An F-test for equality of two variances was performed on the alignment angles of cells at the 8 hour point, between cells on the dynamic surface and the positive control surface. The null hypothesis was the alignment angles of cells on the two surfaces were equal, and assumed the angles were distributed normally around the mean, i.e. the orientation of the grooves. The F-value was found to be 0.145. At a significance level of 0.05, the one-tail critical value of the F-distribution is 0.399. As the F-value was lower than the critical value, the null hypothesis could not be rejected. The variances of the cell alignment angles on both surfaces can be considered equal.

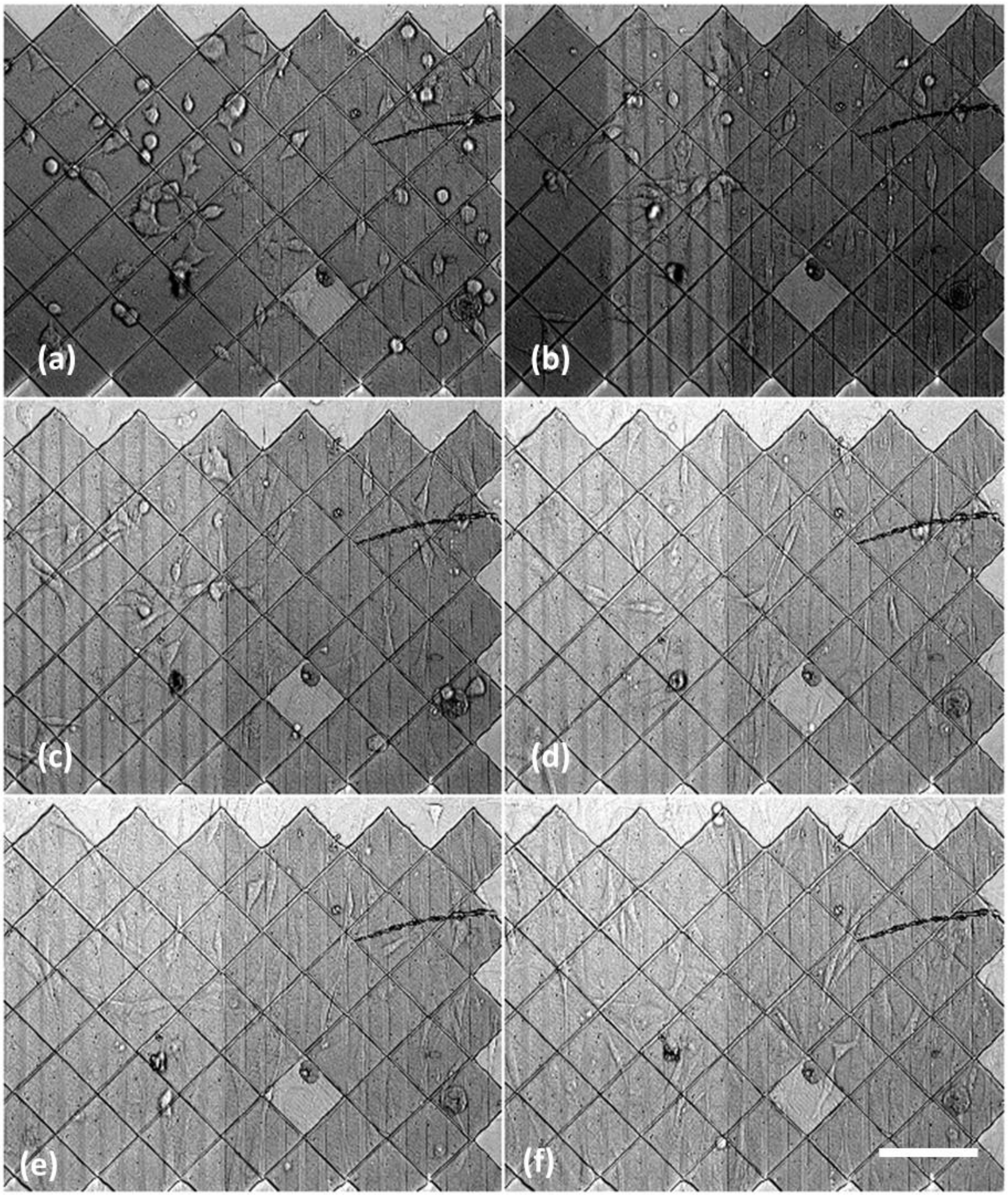

Figure 4.9: A montage showing alignment of cells to grooves. In each image dynamic grooves are to the left and control grooves are to the right. The time points (hh:mm) for the images are -2:45 (a), -0:15 (b), 1:15 (c), 4:15 (d), 8:15 (e), 14:15 (f). Scale bar is 150 µm.

In Figure 4.10, the alignment of 5 cells on both control and dynamic grooved surfaces are tracked using a line plot of alignment angle versus time.

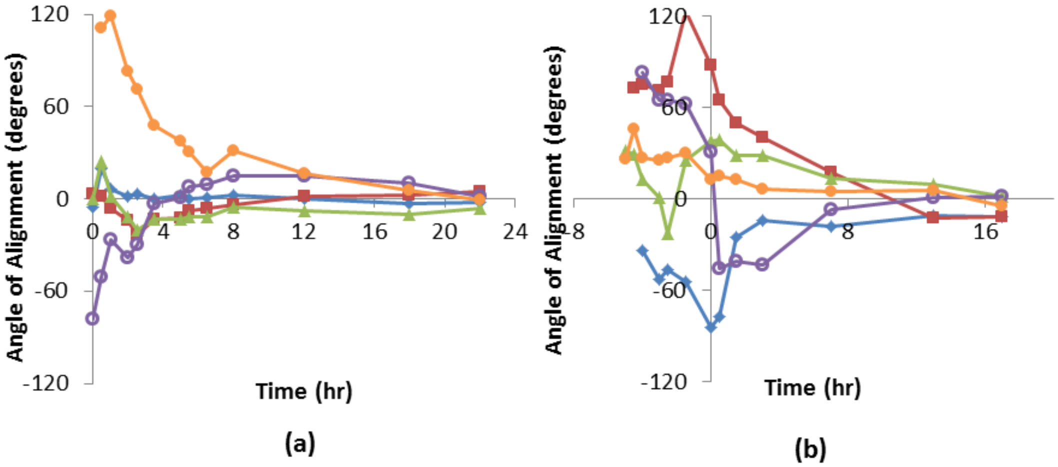

Figure 4.10: Line graphs tracking the alignment angles of individual cells. Each color represents a single cell on control grooves (a) and dynamic grooves (a).

On control grooved surfaces in Figure 4.10 (a), the cells started aligning to the grooves shortly after plating. For the first 1-2 hours, as the cells formed adhesions to the substrate and developed leading edges, their orientation was random. Shortly thereafter, one leading edge per cell started to favor extension along the grooves and pulled the cell body into alignment with the grooves. Cells with an initial polarity furthest from the groove orientation took the longest time to align. However, once cells were aligned parallel to the grooves, they kept their new orientation.

On dynamic grooved surfaces, the cells were originally oriented randomly when they were plated on a flat surface. While the substrate topography was flat, the cells displayed a stellate morphology. Each cell produced multiple leading edges that mutually competed to polarize the cell. Once the grooves were imprinted, however, cells aligned parallel to them.

Based on these results, it can be concluded that the imprinting of grooves to dynamically change the topography of a cell substrate can induce cell alignment to the grooves. The time course of cell morphology change is 8 hours compared with the 12-24 hour responses on shape-memory polymer substrates reported in the literature [6–8]. Whereas the alignment in the shape-memory studies was rate-limited by the shape recovery of the substrate, here the imprinting process took 2 minutes per tile. Consequently, the alignment rate was limited by the time-course of cell mechanisms.

Actin cytoskeleton of aligned cells

As previously discussed in Chapter 1, there is evidence in the literature that when cells align to grooved substrates, their actin cytoskeleton is also seen to align parallel to the grooves [16,17]. Figure 4.11 shows cells aligned to control and dynamic grooves.

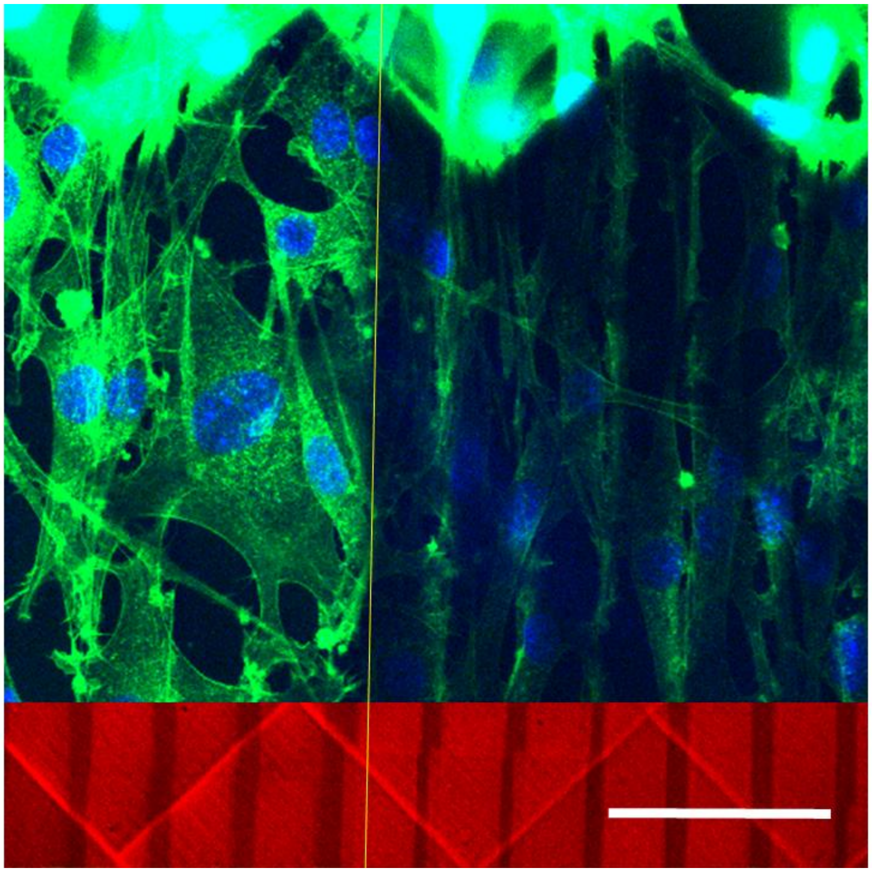

Figure 4.11: Fluorescence image of cells aligned to grooves. Dynamic grooves are to the left of yellow line, control grooves are to the right. Cells are stained to reveal the location of actin (green) and the location of cell nuclei (blue). The red portion indicates the location of the underlying grooves. Ridges (dark red) and troughs (medium red) extend underneath the entire material. The bright red lines are the seams at which printed tiles were overlapped to form a continuous cell substrate. Scale bar 70 µm.

It is worth noting that the micro-3D printed substrate attenuates the excitation laser of the confocal microscope, particularly under the trough of the control grooves, so the cells did not fluoresce uniformly. Nevertheless, the confocal image clearly shows actin-stained cells aligned closely with the ridges of the grooves. Alignment is stronger on the control grooves, which reflects the trend seen in the plots in Figures 4.7 and 4.8.

Migration of cells onto grooved substrates

While cell observations continued on the [5+15] grooves, an unexpected behavioral trend was seen shortly after imprinting. On both the dynamic and control grooves, cells migrated onto the printed substrate from the surrounding glass surface. These cells maintained alignment parallel to the grooves. The change in density of cells aligned to the grooves is plotted in Figure 4.12.

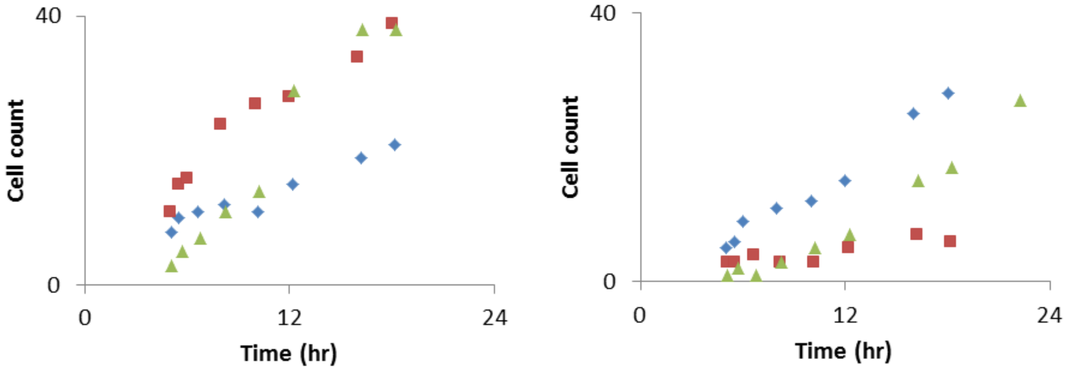

Figure 4.12: Plots showing the number of cells aligned to grooves. Control grooves are on the left and dynamic grooves are on the right. Cells were plated at t = 0. Each marker follows the cell count on one sample. The size of each sample area was ~5,000 μm^2.

This behavior is unexpected because there are no indications in the literature that aligned cells attract more cells, nor is the substrate releasing any chemoattractants that might promote cell migration. It is more likely that the rapid migration of cells onto the substrate is a consequence of the cell plating method used at the beginning of the experiment. To compensate for the large number of cells that drift off the substrate before adhering, cells were plated into the culture well at a very high density, estimated to be 20,000 cells/cm^2. Cells have a tendency to migrate, and they are equally likely to migrate off the pad as onto the pad. However, the higher cell density outside the pad results in a net average movement onto the pad.

This observation suggests ways to encourage migration of cells onto a topographically complex surface in tissue culture applications. If groove dimensions are optimized for a particular cell type, an increase in cell density in the vicinity of the substrate can encourage movement of cells onto the substrate.

4.3 CONCLUSION

This chapter demonstrates an approach for dynamically imprinting micro-3D printed cell substrates with grooves of desired dimensions. There studies confirm that cells remain viable after their substrates are scanned by a laser during imprinting *in situ*. Here, this strategy shows that dynamic grooves are capable of directing cell alignment over a time period of 8 hours.

The results presented in this chapter confirm those of previous studies that showed cells responding to dynamic topographical changes. Whereas prior studies have shown cells responding to substrates that transitioned from grooved to flat topography, this approach demonstrates that changes from flat to grooved topographies are also capable of inducing morphological changes in cells. Furthermore, this method avoids the temperature perturbations that cells on shape-memory polymer substrates were subjected to [6–8].

This approach, and its ability to induce cell behaviors that cannot be observed under other circumstances, has implications for basic research into cell topographical response studies. The results of such studies can be applied to tissue culture research to develop superior grafts and wound-healing scaffolds.

4.4 REFERENCES

1. Van Dongen SFM, Maiuri P, Marie E, Tribet C, Piel M. Triggering Cell Adhesion, Migration or Shape Change with a Dynamic Surface Coating. Adv Mater. 2013;25(12):1687–91.

2. Zhu H, Yan J, Revzin A. Catch and release cell sorting: electrochemical desorption of T-cells from antibody-modified microelectrodes. Colloids Surf B Biointerfaces. 2008 Jul 15;64(2):260–8.

3. Davila J, Chassepot A, Longo J, Boulmedais F, Reisch A, Frisch B, et al. Cyto-mechanoresponsive Polyelectrolyte Multilayer Films. J Am Chem Soc. 2012 Jan 11;134(1):83–6.

4. Shivapooja P, Wang Q, Orihuela B, Rittschof D, López GP, Zhao X. Bioinspired Surfaces with Dynamic Topography for Active Control of Biofouling. Adv Mater. 2013 Mar 13;25(10):1430–4.

5. Kiang JD, Wen JH, del Álamo JC, Engler AJ. Dynamic and reversible surface topography influences cell morphology. J Biomed Mater Res A. 2013 Aug;101(8):2313–21.

6. Ebara M, Uto K, Idota N, Hoffman JM, Aoyagi T. Shape-Memory Surface with Dynamically Tunable Nano-Geometry Activated by Body Heat. Adv Mater. 2012 Jan 10;24(2):273–8.

7. Davis KA, Burke KA, Mather PT, Henderson JH. Dynamic cell behavior on shape memory polymer substrates. Biomaterials. 2011 Mar;32(9):2285–93.

8. Le DM, Kulangara K, Adler AF, Leong KW, Ashby VS. Dynamic topographical control of mesenchymal stem cells by culture on responsive poly(ε-caprolactone) surfaces. Adv Mater. 2011 Aug 2;23(29):3278–83.

9. Gong T, Zhao K, Yang G, Li J, Chen H, Chen Y, et al. The Control of Mesenchymal Stem Cell Differentiation Using Dynamically Tunable Surface Microgrooves. Adv Healthcare Mater [Internet]. 2014 Mar 1 [cited 2014 Jul 13]; Available from: http://onlinelibrary.wiley.com.ezproxy.lib.utexas.edu/doi/10.1002/adhm.201300692/abstract

10. Tibbitt MW, Kloxin AM, Dyamenahalli KU, Anseth KS. Controlled two-photon photodegradation of PEG hydrogels to study and manipulate subcellular interactions on soft materials. Soft Matter. 2010;6(20):5100–8.

11. Reilly GC, Engler AJ. Intrinsic extracellular matrix properties regulate stem cell differentiation. J Biomech. 2010 Jan 5;43(1):55–62.

12. Schindelin J, Arganda-Carreras I, Frise E, Kaynig V, Longair M, Pietzsch T, et al. Fiji: an open-source platform for biological-image analysis. Nat Meth. 2012 Jul;9(7):676–82.

13. Cramer L, Desai A. Fixation and Immunofluorescence of the Cytoskeleton [Internet]. Mitchison Lab Protocols. 2014 [cited 2014 Jul 14]. Available from: http://mitchison.med.harvard.edu/protocols.html

14. LaMuraglia GM, Adili F, Karp SJ, Statius van Eps RG, Watkins MT. Photodynamic therapy inactivates extracellular matrix–basic fibroblast growth factor: Insights to its effect on the vascular wall. Journal of Vascular Surgery. 1997 Aug;26(2):294–301.

15. Curtis A, Wilkinson C. Topographical control of cells. Biomaterials. 1997 Dec;18(24):1573–83.

16. Dunn GA, Brown AF. Alignment of fibroblasts on grooved surfaces described by a simple geometric transformation. J Cell Sci. 1986 Jul 1;83(1):313–40.

17. Oakley C, Brunette DM. The sequence of alignment of microtubules, focal contacts and actin filaments in fibroblasts spreading on smooth and grooved titanium substrata. J Cell Sci. 1993 Sep;106 (Pt 1):343–54.

Chapter 5: Conclusion and Future Directions

5.1 CONCLUSION

This dissertation describes my efforts to introduce dynamic topographies into cell cultures for the purpose of assessing cellular responses. In Chapter 1, I provided background on cellular responses to environmental conditions. I described the historical efforts to understand the mechanisms of cell behavior pertaining to morphology and motility, followed by a summary of the present-day understanding of these mechanisms. I discussed research efforts to understand how cells interacted with various surfaces, and how surface topographies elicited interesting cellular responses. I also discussed the photochemistry involved in micro-3D printing, and how phototoxicity in cells could be minimized during the imprinting process.

In Chapter 2 I discussed my attempts to micro-3D print wall-like structures in neuronal cell cultures to guide neurite extension. I described the development of a flow chamber to enable micro-3D printing in laminar flow, such that reactive photogenerated molecular species could be convected away from proximal cells. I optimized a printing reagent for this application, ensuring that robust walls could be printed under laminar flow. However, I encountered challenges with the cell culture, and this necessitated a change in experimental direction.

In Chapter 3, I developed the technique of imprinting to elicit topographical changes in a micro-3D printed material. I explored how heights of printed tiles could be changed by imprinting, and how parameters such as scan height and number of scans influenced the ultimate height change. I also confirmed that although photosensitizer levels in the material varied over 24 hours, the imprinted height change did not vary significantly.

In the fourth chapter, I applied the imprinting technique from Chapter 3 to create cell culture substrates with dynamic topographies that transitioned from flat to grooved. After confirming that the imprinting process did not damage proximal cells, I determined the optimal dimensions for groove alignment. Next, I demonstrated that when cell substrates switch from flat to grooved, the cells growing on them switch from stellate to bipolar morphology and align parallel to the grooves.

5.2 FUTURE DIRECTIONS

There are several interesting questions raised by these results, suggesting avenues for follow-up research. Characterization of mechanical properties of printed structures would be useful in matching the material to potential applications. For instance, cell motility behavior is linked to the stiffness of their substrates. By tuning the elastic modulus of the material, one can observe how stiffness affects alignment response time and other cellular behaviors. The shear modulus of the material can impact the extent to which imprinting scans affect the surface topography. Examining the correlation between the material's shear modulus and topographical height change can help in modeling the imprinting process and in development of imprinting protocols that generate topographical patterns of desired dimensions.

While this dissertation demonstrated that cells align to grooves that appear on their culture substrate, it would be interesting to see if cells lose their alignment upon the disappearance of grooves. In other words, would cells transition from a bipolar to stellate morphology if their substrate shifts from a grooved topography to a flat topography? It would also be interesting to observe alignment to dynamic grooves after cells are first maintained on flat substrate topography for several hours or a day. It would indicate whether morphological changes are easier or more difficult to induce if intracellular machinery has more time to mature after cells are plated.

One limitation of the method developed in this dissertation was that the cell substrate was printed tile-by-tile to form a pad of dimensions 500 µm by 400 µm. A substrate of this size only had room for 10-20 cells, which limited the statistical power of each experiment. A proposed method to prepare a substrate with a larger surface area is to mold the reagent onto a glass surface and use single-photon illumination to crosslink the gel. The material could then be imprinted using the pulsed laser beam as described.

While grooved substrates are the basis of the classic assay for topographical response in cells, other substrate shapes also evoke interesting responses. It would be a simple matter to develop dynamic substrates with various topographies by creating new masks for the laser raster scan. One potentially interesting application is the fabrication of arrays of microneedles or posts for culturing cells. Such arrays have been used for a decade to study the mechanical forces that cells exert on their substrates [1]. The arrays can mimic continuous surfaces of various stiffness: taller needles, which deflect more than short needles under similar applied forces, are interpreted by cells as more compliant substrates. Imprinting could dynamically change a compliant substrate of tall needles into a stiff substrate of short needles, evoking behavioral responses in cells cultured on the surface. Substrate topographies can also induce cells to migrate slowly and persistently (a trait associated with cells in 3D cultures) rather than fast and randomly (as they do in 2D cultures) [2]. Rapid prototyping through micro-3D printing and dynamic topography changes through imprinting can create a suite of versatile topographies for modeling cellular behavior.

Recent innovations in microscopy are making it easier to track the movement of subcellular structures in real time. Many of these structures play important roles during cell migration and topographical response. Some of these structures, such as microtubules[3] and focal adhesions [4], are easy to image individually and have been modelled in some detail. Others, such as actin filaments, are much more challenging to observe and details of their mechanisms are open to debate [5]. Coupling dynamic substrate technologies, such as imprinting, to cutting-edge imaging techniques such as fluorescent speckle microscopy [6] and super-resolution microscopy [7] can provide insight into the kinetics of these subcellular structures.

While the technologies developed in this dissertation can be deployed for many applications, it is equally intriguing to consider ways in which the micro-3D printed and imprintable material can be made more tunable. At present, the micro-3D printed structures are composed of native bovine serum albumin and unmodified gelatin. While these proteins produced structures that respond to imprinting, it may be possible to develop materials with finely tuned properties such as elastic and shear moduli, density, water content, cell adhesivity, and optical transparency at various wavelengths. Such materials could be made of synthetic polymers or rationally designed proteins [8]. Photosensitizers may be incorporated into the backbone of the polymer to avoid the need to add exogenous photosensitizers [9,10]. Prepared substrates may be functionalized with biologically relevant molecules, either immobilized on the surface or loaded into the material to enable controlled release of diffusible factors [11,12].

It is hoped that research presented in this dissertation will lay the groundwork for future work in the development of dynamic cellular environments, and inspire a deeper understanding and appreciation of cell behavior.

5.3 REFERENCES

1. Tan JL, Tien J, Pirone DM, Gray DS, Bhadriraju K, Chen CS. Cells lying on a bed of microneedles: An approach to isolate mechanical force. Proc Natl Acad Sci. 2003 Feb 18;100(4):1484–9.

2. Ghibaudo M, Trichet L, Le Digabel J, Richert A, Hersen P, Ladoux B. Substrate topography induces a crossover from 2D to 3D behavior in fibroblast migration. Biophys J. 2009 Jul 8;97(1):357–68.

3. Waterman-Storer CM. Microtubules and Microscopes: How the Development of Light Microscopic Imaging Technologies Has Contributed to Discoveries about Microtubule Dynamics in Living Cells. Mol Biol Cell. 1998 Dec;9(12):3263–71.

4. Worth DC, Parsons M. Advances in imaging cell-matrix adhesions. J Cell Sci. 2010 Nov 1;123(Pt 21):3629–38.

5. Yamashiro S, Mizuno H, Smith MB, Ryan GL, Kiuchi T, Vavylonis D, et al. New single-molecule speckle microscopy reveals modification of the retrograde actin flow by focal adhesions at nanometer scales. Mol Biol Cell. 2014 Feb 5;mbc.E13–03–0162.

6. Salmon ED, M. Waterman C. How we discovered fluorescent speckle microscopy. Mol Biol Cell. 2011 Nov 1;22(21):3940–2.

7. Schwartz MA. Super-Resolution Microscopy: A New Dimension in Focal Adhesions. Curr Biol. 2011 Aug 2;21(3):R115–R116.

8. Brandl F, Sommer F, Goepferich A. Rational design of hydrogels for tissue engineering: Impact of physical factors on cell behavior. Biomaterials. 2007 Jan;28(2):134–46.

9. Wang S, Fan W, Kim G, Hah HJ, Lee Y-EK, Kopelman R, et al. Novel methods to incorporate photosensitizers into nanocarriers for cancer treatment by photodynamic therapy. Lasers Surg Med. 2011 Sep;43(7):686–95.

10. Ronzani F, Saint-Cricq P, Arzoumanian E, Pigot T, Blanc S, Oelgemöller M, et al. Immobilized Organic Photosensitizers with Versatile Reactivity for Various Visible-Light Applications. Photochem Photobiol. 2014 Mar 1;90(2):358–68.

11. Lee K, Silva EA, Mooney DJ. Growth factor delivery-based tissue engineering: general approaches and a review of recent developments. J R Soc Interface. 2010 Aug 18;rsif20100223.

12. Santo VE, Gomes ME, Mano JF, Reis RL. Controlled release strategies for bone, cartilage, and osteochondral engineering--Part I: recapitulation of native tissue healing and variables for the design of delivery systems. Tissue Eng Part B Rev. 2013 Aug;19(4):308–26.

Bibliography

Abercrombie M. The bases of the locomotory behaviour of fibroblasts. Exp Cell Res. 1961;8, Supplement:188–98.

Abercrombie M, Heaysman JE, Pegrum SM. The locomotion of fibroblasts in culture. IV. Electron microscopy of the leading lamella. Exp Cell Res. 1971 Aug;67(2):359–67.

Abercrombie M, Heaysman JEM, Pegrum SM. The locomotion of fibroblasts in culture: I. Movements of the leading edge. Exp Cell Res. 1970 a Mar;59(3):393–8.

Abercrombie M, Heaysman JEM, Pegrum SM. The locomotion of fibroblasts in culture: III. Movements of particles on the dorsal surface of the leading lamella. Exp Cell Res. 1970 b Oct;62(2–3):389–98.

Abercrombie M, Heaysman JEM, Pegrum SM. Locomotion of fibroblasts in culture: V. Surface marking with concanavalin A. Exp Cell Res. 1972 Aug;73(2):536–9.

Abuin E, Aspée A, Lissi E, León L. Binding of Rose Bengal to Bovine Serum Albumin. J Chil Chem Soc. 2007 Jun;52(2):1196–7.

Alberto M, Gabriela M. Hydrodynamic Properties of Gelatin - Studies from Intrinsic Viscosity Measurements. In: Verbeek C, editor. Prod Appl Biopolym [Internet]. InTech; 2012 [cited 2014 May 25]. Available from: http://www.intechopen.com/books/products-and-applications-of-biopolymers/hydrodynamic-properties-of-gelatin-studies-from-intrinsic-viscosity-measurements

Albrecht-Buehler G. Filopodia of spreading 3T3 cells. Do they have a substrate-exploring function? J Cell Biol. 1976 May;69(2):275–86.

Albrecht-Buehler G. The angular distribution of directional changes of guided 3T3 cells. J Cell Biol. 1979 Jan;80(1):53–60.

Allen R, Nielson R, Wise DD, Shear JB. Catalytic Three-Dimensional Protein Architectures. Anal Chem. 2005 Jul 15;77(16):5089–95.

Ambrose EJ. The movements of fibrocytes. Exp Cell Res. 1961;8, Supplement:54–73.

Basu S, Campagnola PJ. Properties of crosslinked protein matrices for tissue engineering applications synthesized by multiphoton excitation. J Biomed Mater Res A. 2004 Nov 1;71(2):359–68.

Bellairs R, Curtis A, Dunn G. Cell Behaviour: A Tribute to Michael Abercrombie. Cambridge ; New York: Cambridge University Press; 1982.

Bettinger CJ, Langer R, Borenstein JT. Engineering substrate topography at the micro- and nanoscale to control cell function. Angew Chem Int Ed Engl. 2009;48(30):5406–15.

Bettinger CJ, Orrick B, Misra A, Langer R, Borenstein JT. Microfabrication of poly (glycerol-sebacate) for contact guidance applications. Biomaterials. 2006 Apr;27(12):2558–65.

Bird RB, Stewart WE, Lightfoot EN. Transport Phenomena, 2nd Edition. 2 edition. New York: Wiley; 2001.

Birla L, Cristian A-M, Hillebrand M. Absorption and steady state fluorescence study of interaction between eosin and bovine serum albumin. Spectrochim Acta A Mol Biomol Spectrosc. 2004 Feb;60(3):551–6.

Blankenship AG, Feller MB. Mechanisms underlying spontaneous patterned activity in developing neural circuits. Nat Rev Neurosci. 2010 Jan;11(1):18–29.

Blawas AS, Reichert WM. Protein patterning. Biomaterials. 1998 May;19(7-9):595–609.

Borgens RB. Electrically mediated regeneration and guidance of adult mammalian spinal axons into polymeric channels. Neuroscience. 1999;91(1):251–64.

Brandl F, Sommer F, Goepferich A. Rational design of hydrogels for tissue engineering: Impact of physical factors on cell behavior. Biomaterials. 2007 Jan;28(2):134–46.

Brunette DM. Fibroblasts on micromachined substrata orient hierarchically to grooves of different dimensions. Exp Cell Res. 1986 a May;164(1):11–26.

Brunette DM. Spreading and orientation of epithelial cells on grooved substrata. Exp Cell Res. 1986 b Nov;167(1):203–17.

Buddy D. Ratner, Allan S. Hoffman. Synthetic Hydrogels for Biomedical Applications. Hydrogels Med Relat Appl [Internet]. American Chemical Society; 1976 [cited 2014 Jul 6]. p. 1–36. Available from: http://dx.doi.org/10.1021/bk-1976-0031.ch001

Carter SB. Principles of Cell Motility: The Direction of Cell Movement and Cancer Invasion. Nature. 1965 Dec 18;208(5016):1183–7.

Carter SB. Haptotaxis and the Mechanism of Cell Motility. Nature. 1967 Jan 21;213(5073):256–60.

Cheng C-M, Lin Y-W, Bellin RM, Steward RL Jr, Cheng Y-R, LeDuc PR, et al. Probing localized neural mechanotransduction through surface-modified elastomeric matrices and electrophysiology. Nat Protoc. 2010 Apr;5(4):714–24.

Clark P, Connolly P, Curtis AS, Dow JA, Wilkinson CD. Topographical control of cell behaviour: II. Multiple grooved substrata. Dev Camb Engl. 1990 Apr;108(4):635–44.

Cooper A, Munden HR, Brown GL. The growth of mouse neuroblastoma cells in controlled orientations on thin films of silicon monoxide. Exp Cell Res. 1976 Dec;103(2):435–9.

Craighead HG, James CD, Turner AMP. Chemical and topographical patterning for directed cell attachment. Curr Opin Solid State Mater Sci. 2001 Apr;5(2–3):177–84.

Cramer L, Desai A. Fixation and Immunofluorescence of the Cytoskeleton [Internet]. Mitchison Lab Protoc. 2014 [cited 2014 Jul 14]. Available from: http://mitchison.med.harvard.edu/protocols.html

Crank J. The Mathematics of Diffusion. Clarendon Press; 1956.

Curtis A, Wilkinson C. Topographical control of cells. Biomaterials. 1997 Dec;18(24):1573–83.

Curtis ASG, Varde M. Control of Cell Behavior: Topological Factors. J Natl Cancer Inst. 1964 Jul 1;33(1):15–26.

Danuser G, Allard J, Mogilner A. Mathematical modeling of eukaryotic cell migration: insights beyond experiments. Annu Rev Cell Dev Biol. 2013;29:501–28.

Davila J, Chassepot A, Longo J, Boulmedais F, Reisch A, Frisch B, et al. Cyto-mechanoresponsive Polyelectrolyte Multilayer Films. J Am Chem Soc. 2012 Jan 11;134(1):83–6.

Davis KA, Burke KA, Mather PT, Henderson JH. Dynamic cell behavior on shape memory polymer substrates. Biomaterials. 2011 Mar;32(9):2285–93.

Denk W, Strickler JH, Webb WW. Two-photon laser scanning fluorescence microscopy. Science. 1990 Apr 6;248(4951):73–6.

Dolmans DEJGJ, Fukumura D, Jain RK. Photodynamic therapy for cancer. Nat Rev Cancer. 2003 May;3(5):380–7.

Van Dongen SFM, Maiuri P, Marie E, Tribet C, Piel M. Triggering Cell Adhesion, Migration or Shape Change with a Dynamic Surface Coating. Adv Mater. 2013;25(12):1687–91.

Dulbecco R. Production of Plaques in Monolayer Tissue Cultures by Single Particles of an Animal Virus. Proc Natl Acad Sci U S A. 1952 Aug;38(8):747–52.

Dunn GA, Brown AF. Alignment of fibroblasts on grooved surfaces described by a simple geometric transformation. J Cell Sci. 1986 Jul 1;83(1):313–40.

Dunn GA, Heath JP. A new hypothesis of contact guidance in tissue cells. Exp Cell Res. 1976 Aug;101(1):1–14.

Eagle H. The Specific Amino Acid Requirements of a Mammalian Cell (strain L) in Tissue Culture. J Biol Chem. 1955 Jun 1;214(2):839–52.

Ebara M, Uto K, Idota N, Hoffman JM, Aoyagi T. Shape-Memory Surface with Dynamically Tunable Nano-Geometry Activated by Body Heat. Adv Mater. 2012 Jan 10;24(2):273–8.

Edahiro J-I, Sumaru K, Tada Y, Ohi K, Takagi T, Kameda M, et al. In situ control of cell adhesion using photoresponsive culture surface. Biomacromolecules. 2005 Apr;6(2):970–4.

Ehrmann RL, Gey GO. The Growth of Cells on a Transparent Gel of Reconstituted Rat-Tail Collagen. J Natl Cancer Inst. 1956 Jun 1;16(6):1375–403.

Einstein A. Investigations on the Theory of the Brownian Movement. BN Publishing; 2011.

Folch A, Toner M. Microengineering of cellular interactions. Annu Rev Biomed Eng. 2000;2:227–56.

Foley JD, Grunwald EW, Nealey PF, Murphy CJ. Cooperative modulation of neuritogenesis by PC12 cells by topography and nerve growth factor. Biomaterials. 2005 Jun;26(17):3639–44.

Fraley SI, Feng Y, Krishnamurthy R, Kim D-H, Celedon A, Longmore GD, et al. A distinctive role for focal adhesion proteins in three-dimensional cell motility. Nat Cell Biol. 2010 Jun;12(6):598–604.

Freshney RI. Culture of Animal Cells: A Manual of Basic Technique and Specialized Applications. 6th edition. Hoboken, N.J: Wiley-Blackwell; 2010.

Fritz Böhm RE. Antioxidant inhibition of porphyrin-induced cellular phototoxicity. J Photochem Photobiol B. 2002;177–83.

Furshpan EJ, MacLeish PR, O'Lague PH, Potter DD. Chemical transmission between rat sympathetic neurons and cardiac myocytes developing in microcultures: evidence for cholinergic, adrenergic, and dual-function neurons. Proc Natl Acad Sci U S A. 1976 Nov;73(11):4225–9.

Galle J, Preziosi L, Tosin A. Contact inhibition of growth described using a multiphase model and an individual cell based model. Appl Math Lett. 2009 Oct;22(10):1483–90.

Gauthier NC, Masters TA, Sheetz MP. Mechanical feedback between membrane tension and dynamics. Trends Cell Biol. 2012 Oct;22(10):527–35.

Ge S, Kojio K, Takahara A, Kajiyama T. Bovine serum albumin adsorption onto immobilized organotrichlorosilane surface: influence of the phase separation on protein adsorption patterns. J Biomater Sci Polym Ed. 1998;9(2):131–50.

Geiger B, Spatz JP, Bershadsky AD. Environmental sensing through focal adhesions. Nat Rev Mol Cell Biol. 2009 Jan;10(1):21–33.

Ghibaudo M, Trichet L, Le Digabel J, Richert A, Hersen P, Ladoux B. Substrate topography induces a crossover from 2D to 3D behavior in fibroblast migration. Biophys J. 2009 Jul 8;97(1):357–68.

Gomez N, Lu Y, Chen S, Schmidt CE. Immobilized nerve growth factor and microtopography have distinct effects on polarization versus axon elongation in hippocampal cells in culture. Biomaterials. 2007 Jan;28(2):271–84.

Gong T, Zhao K, Yang G, Li J, Chen H, Chen Y, et al. The Control of Mesenchymal Stem Cell Differentiation Using Dynamically Tunable Surface Microgrooves. Adv Healthc Mater [Internet]. 2014 Mar 1 [cited 2014 Jul 13]; Available from: http://onlinelibrary.wiley.com.ezproxy.lib.utexas.edu/doi/10.1002/adhm.201300692/abstract

Göppert-Mayer M. Über Elementarakte mit zwei Quantensprüngen. Ann Phys. 1931 Jan 1;401(3):273–94.

Greene LA, Tischler AS. Establishment of a noradrenergic clonal line of rat adrenal pheochromocytoma cells which respond to nerve growth factor. Proc Natl Acad Sci U S A. 1976 Jul;73(7):2424–8.

Guo A, Song B, Reid B, Gu Y, Forrester JV, Jahoda CAB, et al. Effects of Physiological Electric Fields on Migration of Human Dermal Fibroblasts. J Invest Dermatol. 2010 Sep;130(9):2320–7.

Gurkan UA, Tasoglu S, Akkaynak D, Avci O, Unluisler S, Canikyan S, et al. Smart Interface Materials Integrated with Microfluidics for On-Demand Local Capture and Release of Cells. Adv Healthc Mater. 2012 Sep;1(5):661–8.

Hammarback J a., Palm S l., Furcht L t., Letourneau P c. Guidance of neurite outgrowth by pathways of substratum-adsorbed laminin. J Neurosci Res. 1985;13(1-2):213–20.

Han L-H, Lai JH, Yu S, Yang F. Dynamic tissue engineering scaffolds with stimuli-responsive macroporosity formation. Biomaterials. 2013 Jun;34(17):4251–8.

Hanson JN, Motala MJ, Heien ML, Gillette M, Sweedler J, Nuzzo RG. Textural guidance cues for controlling process outgrowth of mammalian neurons. Lab Chip. 2009 Jan 7;9(1):122–31.

Harris DC. Quantitative Chemical Analysis. Eighth Edition edition. New York: W. H. Freeman; 2010.

Harrison RG, Greenman MJ, Mall FP, Jackson CM. Observations of the living developing nerve fiber. Anat Rec. 1907;1(5):116–28.

Higashida H, Furuya S. Cholinergic synapse formation between NG108-15 and muscle cells and modulation of transmission. Neurosci Res Suppl Off J Jpn Neurosci Soc. 1990;13:S75–79.

Hoch HC, Jelinski LW, Craighead HG. Nanofabrication and Biosystems: Integrating Materials Science, Engineering, and Biology. Cambridge ; New York, NY, USA: Cambridge University Press; 1996.

Hoffman RM. To do tissue culture in two or three dimensions? That is the question. Stem Cells Dayt Ohio. 1993 Mar;11(2):105–11.

Hoppe TJ. Laser-Based Techniques for Manipulating the Single-Cell Environment [Doctoral]. [Austin, TX]: The University of Texas at Austin; 2013.

Hoppe TJ, Moorjani SG, Shear JB. Generating Arbitrary Chemical Patterns for Multipoint Dosing of Single Cells. Anal Chem. 2013 Apr 2;85(7):3746–51.

Houchin-Ray T, Huang A, West ER, Zelivyanskaya M, Shea LD. Spatially patterned gene expression for guided neurite extension. J Neurosci Res. 2009 Mar;87(4):844–56.

Hynd MR, Frampton JP, Dowell-Mesfin N, Turner JN, Shain W. Directed cell growth on protein-functionalized hydrogel surfaces. J Neurosci Methods. 2007 May 15;162(1-2):255–63.

Ingram VM. A Side View of Moving Fibroblasts. Nature. 1969 May 17;222(5194):641–4.

Ivanova OY, Margolis LB. The Use of Phospholipid Film for Shaping Cell Cultures. Nature. 1973 Mar 16;242(5394):200–1.

Izmailova VN, Derkach SR, Sakvarelidze MA, Levachev SM, Voron'kov NG, Yampol'skaya GP. Gelation in gelatin and gelatin-containing multicomponent blends. Polym Sci Ser C. 2004;46(12):73–92.

Jiang FX, Yurke B, Firestein BL, Langrana NA. Neurite outgrowth on a DNA crosslinked hydrogel with tunable stiffnesses. Ann Biomed Eng. 2008 Sep;36(9):1565–79.

Jonker AM, Löwik DWPM, van Hest JCM. Peptide- and Protein-Based Hydrogels. Chem Mater. 2012 Mar 13;24(5):759–73.

Kaehr B, Allen R, Javier DJ, Currie J, Shear JB. Guiding neuronal development with in situ microfabrication. Proc Natl Acad Sci U S A. 2004 Nov 16;101(46):16104–8.

Kaehr B, Ertas N, Nielson R, Allen R, Hill RT, Plenert M, et al. Direct-write fabrication of functional protein matrixes using a low-cost Q-switched laser. Anal Chem. 2006 May 1;78(9):3198–202.

Kaehr B, Shear JB. Mask-Directed Multiphoton Lithography. J Am Chem Soc. 2007 Jan 30;129(7):1904–5.

Kaehr B, Shear JB. Multiphoton fabrication of chemically responsive protein hydrogels for microactuation. Proc Natl Acad Sci. 2008 Jul 1;105(26):8850–4.

Kaehr BJ. Defining Cellular Microenvironments Using Multiphoton Lithography [Doctoral]. [Austin, TX]: The University of Texas at Austin; 2007.

Kaiser W, Garrett C. Two-Photon Excitation in CaF_{2}: Eu^{2+}. Phys Rev Lett. 1961 Sep;7(6):229–31.

Kandel E, Schwartz J, Jessell T. Principles of Neural Science. 4 edition. New York: McGraw-Hill Medical; 2000.

Kasapis S, Norton IT, Ubbink JB. Modern Biopolymer Science: Bridging the Divide between Fundamental Treatise and Industrial Application. Academic Press; 2009.

Kiang JD, Wen JH, del Álamo JC, Engler AJ. Dynamic and reversible surface topography influences cell morphology. J Biomed Mater Res A. 2013 Aug;101(8):2313–21.

Kim B-S, Nikolovski J, Bonadio J, Mooney DJ. Cyclic mechanical strain regulates the development of engineered smooth muscle tissue. Nat Biotechnol. 1999 Oct;17(10):979–83.

Kleinfeld D, Kahler KH, Hockberger PE. Controlled outgrowth of dissociated neurons on patterned substrates. J Neurosci Off J Soc Neurosci. 1988 Nov;8(11):4098–120.

Kloxin AM, Kloxin CJ, Bowman CN, Anseth KS. Mechanical Properties of Cellularly Responsive Hydrogels and Their Experimental Determination. Adv Mater. 2010;22(31):3484–94.

Kornreich BG. The patch clamp technique: principles and technical considerations. J Vet Cardiol Off J Eur Soc Vet Cardiol. 2007 May;9(1):25–37.

Krsko P, McCann TE, Thach T-T, Laabs TL, Geller HM, Libera MR. Length-scale mediated adhesion and directed growth of neural cells by surface-patterned poly(ethylene glycol) hydrogels. Biomaterials. 2009 Feb;30(5):721–9.

Krystosek A. Neurite formation by neuroblastoma-glioma hybrid cells (NG108-15) in defined medium: stochastic initiation with persistence of differentiated functions. J Cell Physiol. 1985 Nov;125(2):319–29.

Lackie JM, Dunn GA, Jones GE. Cell Behaviour: Control and Mechanism of Motility. London: Portland Press;

LaFratta CN, Fourkas JT, Baldacchini T, Farrer RA. Multiphoton Fabrication. Angew Chem Int Ed. 2007 Aug 20;46(33):6238–58.

LaMuraglia GM, Adili F, Karp SJ, Statius van Eps RG, Watkins MT. Photodynamic therapy inactivates extracellular matrix–basic fibroblast growth factor: Insights to its effect on the vascular wall. J Vasc Surg. 1997 Aug;26(2):294–301.

Lauffenburger DA, Horwitz AF. Cell Migration: A Physically Integrated Molecular Process. Cell. 1996 Feb 9;84(3):359–69.

Lavie G, Kaplinsky C, Toren A, Aizman I, Meruelo D, Mazur Y, et al. A photodynamic pathway to apoptosis and necrosis induced by dimethyl tetrahydroxyhelianthrone and hypericin in leukaemic cells: possible relevance to photodynamic therapy. Br J Cancer. 1999 Feb;79(3-4):423–32.

Law JK-Y, Yeung C-K, Li L, Rudd JA, Ingebrandt S, Chan M. The Use of SU-8 Topographically Guided Microelectrode Array in Measuring Extracellular Field Potential Propagation. Ann Biomed Eng. 2012 Mar 1;40(3):619–27.

Lazarides E, Weber K. Actin Antibody: The Specific Visualization of Actin Filaments in Non-Muscle Cells. Proc Natl Acad Sci. 1974 Jun 1;71(6):2268–72.

Le DM, Kulangara K, Adler AF, Leong KW, Ashby VS. Dynamic topographical control of mesenchymal stem cells by culture on responsive poly(ε-caprolactone) surfaces. Adv Mater Deerfield Beach Fla. 2011 Aug 2;23(29):3278–83.

Lee K, Silva EA, Mooney DJ. Growth factor delivery-based tissue engineering: general approaches and a review of recent developments. J R Soc Interface. 2010 Aug 18;rsif20100223.

Levy JG. Photosensitizers in photodynamic therapy. Semin Oncol. 1994 Dec;21(6 Suppl 15):4–10.

Li GN, Liu J, Hoffman-Kim D. Multi-molecular gradients of permissive and inhibitory cues direct neurite outgrowth. Ann Biomed Eng. 2008 a Jun;36(6):889–904.

Li J, McNally H, Shi R. Enhanced neurite alignment on micro-patterned poly-L-lactic acid films. J Biomed Mater Res A. 2008 b Nov;87(2):392–404.

Liu J, Tu H, Zhang D, Zheng H, Li Y-L. Voltage-gated sodium channel expression and action potential generation in differentiated NG108-15 cells. BMC Neurosci. 2012 Oct 25;13(1):129.

Loeb L. Über die Entstehung von Bindegewebe, Leucocyten und roten Blutkörperchen aus Epithel; und über eine Methode, isolierte Gewebsteile zu züchten [Internet]. Chicago, Stern; 1897 [cited 2013 Dec 23]. Available from: http://archive.org/details/berdieentstehu00loeb

Lohof AM, Quillan M, Dan Y, Poo MM. Asymmetric modulation of cytosolic cAMP activity induces growth cone turning. J Neurosci Off J Soc Neurosci. 1992 Apr;12(4):1253–61.

Lu CY, Liu YY. Electron transfer oxidation of tryptophan and tyrosine by triplet states and oxidized radicals of flavin sensitizers: a laser flash photolysis study. Biochim Biophys Acta. 2002 May 10;1571(1):71–6.

Lydon MJ, Minett TW, Tighe BJ. Cellular interactions with synthetic polymer surfaces in culture. Biomaterials. 1985 Nov;6(6):396–402.

Lyon JL, Hill RT, Shear JB, Stevenson KJ. Direct Electrochemical and Spectroscopic Assessment of Heme Integrity in Multiphoton Photo-Cross-Linked Cytochrome c Structures. Anal Chem. 2007 Feb 9;79(6):2303–11.

Ma W, Fitzgerald W, Liu Q-Y, O'Shaughnessy TJ, Maric D, Lin HJ, et al. CNS stem and progenitor cell differentiation into functional neuronal circuits in three-dimensional collagen gels. Exp Neurol. 2004 Dec;190(2):276–88.

Mahoney MJ, Chen RR, Tan J, Saltzman WM. The influence of microchannels on neurite growth and architecture. Biomaterials. 2005 Mar;26(7):771–8.

Maloney MT, Bamburg JR. Mechanisms of neuronal growth cone guidance: an historical perspective. Dev Neurobiol. 2011 Sep;71(9):795–800.

Maruo S, Nakamura O, Kawata S. Three-dimensional microfabrication with two-photon-absorbed photopolymerization. Opt Lett. 1997 Jan 15;22(2):132–4.

MBInfo contributors. Types of cell-matrix adhesion complexes [Internet]. MBInfo Wiki; 2011 [cited 2014 Jun 18]. Available from: http://www.mechanobio.info/figure/1384243207520.jpg.html

MBInfo contributors. Growth cone structure [Internet]. MBInfo Wiki; 2012 [cited 2014 Jun 18]. Available from: http://www.mechanobio.info/figure/1384241700956.jpg.html

McCaig CD, Song B, Rajnicek AM. Electrical dimensions in cell science. J Cell Sci. 2009 Dec 1;122(23):4267–76.

Merz M, Fromherz P. Polyester Microstructures for Topographical Control of Outgrowth and Synapse Formation of Snail Neurons. Adv Mater. 2002 Jan 16;14(2):141–4.

Moorjani S, Nielson R, Chang XA, Shear JB. Dynamic remodeling of subcellular chemical gradients using a multi-directional flow device. Lab Chip. 2010 Aug 21;10(16):2139–46.

Mousavi SH, Tavakkol-Afshari J, Brook A, Jafari-Anarkooli I. Direct toxicity of Rose Bengal in MCF-7 cell line: Role of apoptosis. Food Chem Toxicol. 2009 Apr;47(4):855–9.

Nguyen HT, Sapp S, Wei C, Chow JK, Nguyen A, Coursen J, et al. Electric field stimulation through a biodegradable polypyrrole-co-polycaprolactone substrate enhances neural cell growth. J Biomed Mater Res A. 2014 Aug;102(8):2554–64.

Nielson R, Kaehr B, Shear JB. Microreplication and Design of Biological Architectures Using Dynamic-Mask Multiphoton Lithography. Small. 2009 Jan 1;5(1):120–5.

Nielson RY. Nonlinear laser microfabrication in biological environments [Doctoral]. [Austin, TX]: The University of Texas at Austin; 2007.

Oakley C, Brunette DM. The sequence of alignment of microtubules, focal contacts and actin filaments in fibroblasts spreading on smooth and grooved titanium substrata. J Cell Sci. 1993 Sep;106 (Pt 1):343–54.

Offenhäusser A, Böcker-Meffert S, Decker T, Helpenstein R, Gasteier P, Groll J, et al. Microcontact printing of proteins for neuronal cell guidance. Soft Matter. 2007 Feb 14;3(3):290–8.

Ohara PT, Buck RC. Contact guidance in vitro: A light, transmission, and scanning electron microscopic study. Exp Cell Res. 1979 Jul;121(2):235–49.

Okano T, Yamada N, Okuhara M, Sakai H, Sakurai Y. Mechanism of cell detachment from temperature-modulated, hydrophilic-hydrophobic polymer surfaces. Biomaterials. 1995 Mar;16(4):297–303.

Pelham RJ, Wang Y -l. Cell locomotion and focal adhesions are regulated by substrate flexibility. Proc Natl Acad Sci. 1997 Dec 9;94(25):13661–5.

Petersen OW, R?nnov-Jessen L, Howlett AR, Bissell MJ. Interaction with basement membrane serves to rapidly distinguish growth and differentiation pattern of normal and malignant human breast epithelial cells. Proc Natl Acad Sci U S A. 1992 Oct 1;89(19):9064–8.

Petrie RJ, Doyle AD, Yamada KM. Random versus directionally persistent cell migration. Nat Rev Mol Cell Biol. 2009 Aug;10(8):538–49.

Phillips GO, Williams PA. Handbook of Hydrocolloids. Taylor & Francis; 2000.

Pitts JD, Campagnola PJ, Epling GA, Goodman SL. Submicron Multiphoton Free-Form Fabrication of Proteins and Polymers: Studies of Reaction Efficiencies and Applications in Sustained Release. Macromolecules. 2000 Feb 5;33(5):1514–23.

Postnikova BJ, Currie J, Doyle T, Hanes RE, Anslyn EV, Shear JB, et al. Towards nanoscale three-dimensional fabrication using two-photon initiated polymerization and near-field excitation. Microelectron Eng. 2003 Sep;69(2–4):459–65.

Puck TT, Marcus PI. A Rapid Method for Viable Cell Titration and Clone Production with HeLa Cells in Tissue Culture: The Use of X-Radiated Cells to Supply Conditioning Factors. Proc Natl Acad Sci U S A. 1955 Jul 15;41(7):432–7.

Qiu Y, Park K. Environment-sensitive hydrogels for drug delivery. Adv Drug Deliv Rev. 2001 Dec 31;53(3):321–39.

Rajnicek A, Britland S, McCaig C. Contact guidance of CNS neurites on grooved quartz: influence of groove dimensions, neuronal age and cell type. J Cell Sci. 1997 Dec;110 (Pt 23):2905–13.

Rangarajan R, Zaman MH. Modeling cell migration in 3D. Cell Adhes Migr. 2008;2(2):106–9.

Ravve A. Light-Associated Reactions of Synthetic Polymers. Springer Science & Business Media; 2007.

Reilly GC, Engler AJ. Intrinsic extracellular matrix properties regulate stem cell differentiation. J Biomech. 2010 Jan 5;43(1):55–62.

Ridley A, Peckham M, Clark P. Cell Motility: From Molecules to Organisms. 1 edition. Wiley; 2007.

Ritger PL, Peppas NA. A simple equation for description of solute release I. Fickian and non-fickian release from non-swellable devices in the form of slabs, spheres, cylinders or discs. J Controlled Release. 1987 Jun;5(1):23–36.

Ronzani F, Saint-Cricq P, Arzoumanian E, Pigot T, Blanc S, Oelgemöller M, et al. Immobilized Organic Photosensitizers with Versatile Reactivity for Various Visible-Light Applications. Photochem Photobiol. 2014 Mar 1;90(2):358–68.

Rosenkranz AA, Jans DA, Sobolev AS. Targeted intracellular delivery of photosensitizers to enhance photodynamic efficiency. Immunol Cell Biol. 2000 Aug;78(4):452–64.

Rous P, Jones FS. A Method for Obtaining Suspensions of Living Cells from the Fixed Tissues, and for the Plating Out of Individual Cells. J Exp Med. 1916 Apr 1;23(4):549–55.

Rovensky YA, Slavnaja IL, Vasiliev JM. Behaviour of fibroblast-like cells on grooved surfaces. Exp Cell Res. 1971 Mar;65(1):193–201.

Rutten WLC, Smit JPA, Frieswijk T., Bielen J., Brouwer AH, Buitenweg JR, et al. Neuro-electronic interfacing with multielectrode arrays. IEEE Eng Med Biol Mag. 1999 May;18(3):47–55.

Salmon ED, M. Waterman C. How we discovered fluorescent speckle microscopy. Mol Biol Cell. 2011 Nov 1;22(21):3940–2.

Sanford KK, Earle WR, Likely GD. The growth in vitro of single isolated tissue cells. J Natl Cancer Inst. 1948 Dec;9(3):229–46.

Sanford KK, Westfall BB, Fioramonti MC, McQuilken WT, Bryant JC, Peppers EV, et al. The effect of serum fractions on the proliferation of strain L mouse cells in vitro. J Natl Cancer Inst. 1955 Dec;16(3):789–802.

Santo VE, Gomes ME, Mano JF, Reis RL. Controlled release strategies for bone, cartilage, and osteochondral engineering--Part I: recapitulation of native tissue healing and variables for the design of delivery systems. Tissue Eng Part B Rev. 2013 Aug;19(4):308–26.

Schindelin J, Arganda-Carreras I, Frise E, Kaynig V, Longair M, Pietzsch T, et al. Fiji: an open-source platform for biological-image analysis. Nat Methods. 2012 Jul;9(7):676–82.

Schwartz MA. Super-Resolution Microscopy: A New Dimension in Focal Adhesions. Curr Biol. 2011 Aug 2;21(3):R115–R116.

Seidlits SK, Drinnan CT, Petersen RR, Shear JB, Suggs LJ, Schmidt CE. Fibronectin-hyaluronic acid composite hydrogels for three-dimensional endothelial cell culture. Acta Biomater. 2011 Jun;7(6):2401–9.

Seidlits SK, Schmidt CE, Shear JB. High-Resolution Patterning of Hydrogels in Three Dimensions using Direct-Write Photofabrication for Cell Guidance. Adv Funct Mater. 2009 Nov 23;19(22):3543–51.

Serbin J, Egbert A, Ostendorf A, Chichkov BN, Houbertz R, Domann G, et al. Femtosecond laser-induced two-photon polymerization of inorganic organic hybrid materials for applications in photonics. Opt Lett. 2003 Mar 1;28(5):301–3.

Shen HR, Spikes JD, Kopeceková P, Kopecek J. Photodynamic crosslinking of proteins. I. Model studies using histidine- and lysine-containing N-(2-hydroxypropyl)methacrylamide copolymers. J Photochem Photobiol B. 1996 Jul;34(2-3):203–10.

Shivapooja P, Wang Q, Orihuela B, Rittschof D, López GP, Zhao X. Bioinspired Surfaces with Dynamic Topography for Active Control of Biofouling. Adv Mater. 2013 Mar 13;25(10):1430–4.

Singh AV, Gailite L, Vyas V, Lenardi C, Forti S, Matteoli M, et al. Rapid prototyping of nano- and micro-patterned substrates for the control of cell neuritogenesis by topographic and chemical cues. Mater Sci Eng C. 2011 Jul 20;31(5):892–9.

Spikes JD, Shen HR, Kopecková P, Kopecek J. Photodynamic crosslinking of proteins. III. Kinetics of the FMN- and rose bengal-sensitized photooxidation and intermolecular crosslinking of model tyrosine-containing N-(2-

hydroxypropyl)methacrylamide copolymers. Photochem Photobiol. 1999 Aug;70(2):130–7.

Stein WH, Stein WH. Amino Acif Composition of β-Lactoglobulin and Bovine Serum Albumin. J Biol Chem. 1949 Mar 1;178(1):79–91.

Stephanie Nemir HNH. PEGDA hydrogels with patterned elasticity: Novel tools for the study of cell response to substrate rigidity. Biotechnol Bioeng. 2009;105(3):636–44.

Sun H-B, Maeda M, Takada K, Chon JWM, Gu M, Kawata S. Experimental investigation of single voxels for laser nanofabrication via two-photon photopolymerization. Appl Phys Lett. 2003 Aug 4;83(5):819–21.

Szpak P. Fish bone chemistry and ultrastructure: implications for taphonomy and stable isotope analysis. J Archaeol Sci. 2011 Dec;38(12):3358–72.

Tan JL, Tien J, Pirone DM, Gray DS, Bhadriraju K, Chen CS. Cells lying on a bed of microneedles: An approach to isolate mechanical force. Proc Natl Acad Sci. 2003 Feb 18;100(4):1484–9.

Tathireddy P, Rieth L, Sharma A, Solzbacher F. Implantable microsystems and neuro electronic interfaces. 2009 IET Bionic Health Gener Implants Prosthet Devices. 2009. p. 1–22.

Testori A, Faries MB, Thompson JF, Pennacchioli E, Deroose JP, van Geel AN, et al. Local and intralesional therapy of in-transit melanoma metastases. J Surg Oncol. 2011 Sep;104(4):391–6.

Théry M. Micropatterning as a tool to decipher cell morphogenesis and functions. J Cell Sci. 2010 Dec 15;123(Pt 24):4201–13.

Tibbitt MW, Anseth KS. Dynamic Microenvironments: The Fourth Dimension. Sci Transl Med. 2012 Nov 14;4(160):160ps24–160ps24.

Tibbitt MW, Kloxin AM, Dyamenahalli KU, Anseth KS. Controlled two-photon photodegradation of PEG hydrogels to study and manipulate subcellular interactions on soft materials. Soft Matter. 2010;6(20):5100–8.

Todaro GJ, Green H. Quantitative Studies of the Growth of Mouse Embryo Cells in Culture and Their Development into Established Lines. J Cell Biol. 1963 May 1;17(2):299–313.

Tomatsu I, Peng K, Kros A. Photoresponsive hydrogels for biomedical applications. Adv Drug Deliv Rev. 2011 Nov;63(14–15):1257–66.

Truskey GA, Yuan F, Katz DF. Transport Phenomena in Biological Systems. 2 edition. Upper Saddle River, N.J: Prentice Hall; 2009.

Van der Valk J, Brunner D, De Smet K, Fex Svenningsen A, Honegger P, Knudsen LE, et al. Optimization of chemically defined cell culture media--replacing fetal bovine serum in mammalian in vitro methods. Toxicol Vitro Int J Publ Assoc BIBRA. 2010 Jun;24(4):1053–63.

Vogel V, Sheetz M. Local force and geometry sensing regulate cell functions. Nat Rev Mol Cell Biol. 2006 Apr;7(4):265–75.

Vogt AK, Brewer GJ, Decker T, Böcker-Meffert S, Jacobsen V, Kreiter M, et al. Independence of synaptic specificity from neuritic guidance. Neuroscience. 2005 a;134(3):783–90.

Vogt AK, Brewer GJ, Offenhäusser A. Connectivity patterns in neuronal networks of experimentally defined geometry. Tissue Eng. 2005 b Dec;11(11-12):1757–67.

Vogt AK, Wrobel G, Meyer W, Knoll W, Offenhäusser A. Synaptic plasticity in micropatterned neuronal networks. Biomaterials. 2005 c May;26(15):2549–57.

Wang CJ, Li X, Lin B, Shim S, Ming G, Levchenko A. A microfluidics-based turning assay reveals complex growth cone responses to integrated gradients of substrate-bound ECM molecules and diffusible guidance cues. Lab Chip. 2008 Jan 29;8(2):227–37.

Wang JH-C, Celechovsky C, Woo SL-Y. Effects of silicone microgrooves on 3T3 fibroblasts. Eng Med Biol 1999 21st Annu Conf 1999 Annu Fall Meetring Biomed Eng Soc BMESEMBS Conf 1999 Proc First Jt. 1999. p. 781 vol.2.

Wang S, Fan W, Kim G, Hah HJ, Lee Y-EK, Kopelman R, et al. Novel methods to incorporate photosensitizers into nanocarriers for cancer treatment by photodynamic therapy. Lasers Surg Med. 2011 Sep;43(7):686–95.

Waterman-Storer CM. Microtubules and Microscopes: How the Development of Light Microscopic Imaging Technologies Has Contributed to Discoveries about Microtubule Dynamics in Living Cells. Mol Biol Cell. 1998 Dec;9(12):3263–71.

Waters CM, Ridge KM, Sunio G, Venetsanou K, Sznajder JI. Mechanical stretching of alveolar epithelial cells increases Na(+)-K(+)-ATPase activity. J Appl Physiol Bethesda Md 1985. 1999 Aug;87(2):715–21.

Wedlich D. Cell Migration in Development and Disease. 1st edition. Weinheim: Wiley-Blackwell; 2005.

Weiss P. Erzwingung elementarer Strukturverschiedenheiten am in vitro wachsenden Gewebe. Wilhelm Roux Arch Für Entwicklungsmechanik Org. 1929 Jun 27;116(1):438–554.

Weiss P. Cell contact. Int Rev Cytol. 1958;(7):391–423.

Weiss P. Cellular Dynamics. Rev Mod Phys. 1959 Jan;31(1):11–20.

Weiss P. Guiding principles in cell locomotion and cell aggregation. Exp Cell Res. 1961;8:260–81.

Wheeler BC, Brewer GJ. Designing Neural Networks in Culture. Proc IEEE Inst Electr Electron Eng. 2010 Mar 1;98(3):398–406.

Wheeler BC, Corey JM, Brewer GJ, Branch DW. Microcontact printing for precise control of nerve cell growth in culture. J Biomech Eng. 1999 Feb;121(1):73–8.

Wójciak-Stothard B, Curtis A, Monaghan W, Macdonald K, Wilkinson C. Guidance and Activation of Murine Macrophages by Nanometric Scale Topography. Exp Cell Res. 1996 Mar 15;223(2):426–35.

Worth DC, Parsons M. Advances in imaging cell-matrix adhesions. J Cell Sci. 2010 Nov 1;123(Pt 21):3629–38.

Wright AK, Thompson MR. Hydrodynamic structure of bovine serum albumin determined by transient electric birefringence. Biophys J. 1975 Feb;15(2 Pt 1):137–41.

Yamashiro S, Mizuno H, Smith MB, Ryan GL, Kiuchi T, Vavylonis D, et al. New single-molecule speckle microscopy reveals modification of the retrograde actin flow by focal adhesions at nanometer scales. Mol Biol Cell. 2014 Feb 5;mbc.E13–03–0162.

Yang J, Richards J, Bowman P, Guzman R, Enami J, McCormick K, et al. Sustained growth and three-dimensional organization of primary mammary tumor epithelial cells embedded in collagen gels. Proc Natl Acad Sci U S A. 1979 Jul;76(7):3401–5.

Yeo W-S, Yousaf MN, Mrksich M. Dynamic interfaces between cells and surfaces: electroactive substrates that sequentially release and attach cells. J Am Chem Soc. 2003 Dec 10;125(49):14994–5.

Zhang J, Venkataramani S, Xu H, Song Y-K, Song H-K, Palmore GTR, et al. Combined topographical and chemical micropatterns for templating neuronal networks. Biomaterials. 2006 Nov;27(33):5734–9.

Zhu H, Yan J, Revzin A. Catch and release cell sorting: electrochemical desorption of T-cells from antibody-modified microelectrodes. Colloids Surf B Biointerfaces. 2008 Jul 15;64(2):260–8.

Milestone 2 : Nature Milestones in Cytoskeleton [Internet]. [cited 2013 Dec 28]. Available from: http://www.nature.com/milestones/milecyto/full/milecyto02.html

Vita

Maryam Ali was born in Rawalpindi, Pakistan to Muhammad and Jehanara Ali, and acquired a brother shortly thereafter. She completed her secondary schooling at The City School, Capital Campus in Islamabad, Pakistan. In 2005, she earned her Bachelor of Science in Chemical Engineering (Materials track) from the California Institute of Technology in Pasadena, California, where she conducted undergraduate research with Dr. Geoffrey A. Blake and Dr. David A. Tirrell. She went on to earn her Master of Science in Chemical Engineering from Auburn University in Auburn, Alabama in 2007. Her thesis, "Therapeutic Contact Lenses for Comfort Molecules," was based on research conducted with her advisor, Dr. Mark E. Byrne. In 2007, she entered the Biomedical Engineering graduate program at the University of Texas at Austin.

Permanent email: ali.maryam@gmail.com
This dissertation was typed by the author.